ANALYZING THE EFFECTS OF SCAFFOLD AND SYNTHESIZED MATERIAL PROPERTIES IN AN *IN VITRO* COLONIC EPITHELIAL CELL MODEL

Riley Logan Howard

A dissertation submitted to the faculty at the University of North Carolina at Chapel Hill in partial fulfillment of the requirements for the degree of Doctor of Philosophy in the Department of Applied Physical Sciences.

Chapel Hill
2020

Approved by:

Nancy L. Allbritton

David B. Hill

Richard Superfine

Daphne Klotsa

Scott Magness

ABSTRACT

Riley Logan Howard: Analyzing the effects of scaffold and synthesized material properties in an *in vitro* colonic epithelial cell model
(Under the direction of Nancy Allbritton)

The epithelial layer of the large intestine displays a unique structural biology known as intestinal crypts, invaginations within the epithelial wall which display spontaneous polarization between stem cells at the base of the crypt and differentiated cells approaching the epithelial lumen. This layer is supported by the lamina propria, a supportive and connective layer of tissue which contains a number of extracellular proteins. This layer of epithelial cells is coated by a two-tiered mucus layer, with a compacted inner layer anchored within the crypt goblet cells and a more porous gel-like outer layer which contains bacteria and other debris. This tissue architecture presents a unique opportunity for studying the effects of physical microenvironment properties on stem cell behavior *in vitro*. It also provides a useful platform for the synthesis and analysis of intestinal mucus, which in recent years has become an important focus in numerous disease models. This dissertation focuses on the analysis of the effects of altering the physical structure of a cell scaffold on *in vitro* colonic cell culture, as well as the mechanical and chemical properties of generated *in vitro* mucus.

Chapter Two of this dissertation focuses on the rheological and biochemical analysis of generated *in vitro* mucus, which was produced by a monolayer of colonic epithelial cells using an air-liquid interface and a type I collagen hydrogel scaffold. This mucus was directly compared to mucus harvested from *ex vivo* colon tissue resections, and demonstrated that this system

produces mucus with similar properties to native mucus, though *ex vivo* mucus did form larger overall mucus complexes. Chapters Three and Four demonstrate the creation of a gradient of surface properties on a single scaffold template via the use of controlled silane vapor deposition. Using this template to create *in vitro* crypts with controlled microcurvature in the stem cell niche, it was found that crypts with convex curvature displayed higher levels of proliferative activity than flat or convex crypts. It was also found that crypts with convex curvature displayed a higher level of globular, unorganized actin in their extracellular structure.

To my family and friends, thanks for sticking with me through all my years of being a student. I wouldn't have made it through this without you all.

ACKNOWLEDGMENTS

There are a number of people that deserve my acknowledgment for their role in helping me successfully complete my graduate school career. First, I have to extend my thanks to Nancy Allbritton and Chris Sims for giving me a home in their lab and always providing me with resources, advice, and mentorship throughout my graduate tenure. I want to thank the entirety of the Allbritton Lab for creating an amazing workplace for me to call home for half a decade. Within the lab, there are a few people I want to specifically acknowledge. I need to thank Yuli Wang and Angie Proctor for always being there to answer any questions I had regarding my research or general science; I wouldn't have been able to finish nearly as quickly without your help. I'm also very grateful to Nicole Smiddy, my desk neighbor for our entire tenure in the lab; I'm so incredibly happy for your graduation, and I know you're going to do great things in the next chapter of your life. I want to thank my primary undergraduate research assistant, Matt Leff; good luck as you graduate and move on into your career. I'd also like to thank (in no particular order) Johanna Dutton, Sam Hinman, Matt Disalvo, Rayna Kim, and Pete Attayek for their guidance, assistance, and friendship. Outside of the Allbritton lab, I need to give many thanks to David Hill for taking me in after the Allbritton lab left North Carolina; the mentorship and friendship he has showed me have been nothing short of awe-inspiring, and I will be forever grateful for his generosity. In the Hill lab, I need to thank Billy Kissner and Matt Markovetz for their advice and friendship. Outside of these specific labs, I want to thank Camille Ehre, Kenza Araba, Matthew Schaner, Shehzad Sheikh, Daniel Harris, Francesca Bernardi, and Scott

Magness for their assistance and advice during various projects in my graduate career. I'd also like to thank the other members of my committee, Daphne Klotsa and Richard Superfine, for always having an open door for me. Outside of my fellow scientists, there are many friends and family members who helped me survive graduate school. The friends who helped me along the way are too numerous to list here, but there are a few who I think deserve special acknowledgment for their support: Kevin Knight, Jimmy Fay, Emma Crenshaw, Tom Kolb, Zane James, Patrick Kiernan, Jackson Cox, Andrew Creech, Emi Foss, Jenna White, JP Bouquet, Kyle and Peyton Glover, Matt Begley, Jeremy Troutman, Bryan Tuck, and Lee Land. Thank you all for your friendship, support, and listening to my many rants about my work. Finally, I must thank my family for getting me to this point. To my sister Devon, thank you for always being such an amazing role model and for always having my back no matter what; you're the hardest worker and kindest person I've ever had the pleasure of knowing, and I'm lucky that I've got you in my life. To my father Doug, thank you for always pushing me and supporting me, because I wouldn't be half the man I am today without modeling myself after you. I've always worked my hardest to make you proud of me, and I'm so glad that we're both Tar Heels. And finally, to my amazing mother Pam, thank you for always being my biggest fan and always giving me the very best advice on everything. Even though I don't call nearly enough, I can't put into words just how comforting it is to know you'll always support me. I love all three of you dearly.

TABLE OF CONTENTS

LIST OF FIGURES

LIST OF TABLES

LIST OF ABBREVIATIONS AND SYMBOLS

°	Degrees
°C	Degrees Celsius
µg	Microgram
µL	Microliter
µm	Micrometer
1D	One-dimensional
2D	Two-dimensional
3D	Three-dimensional
ALI	Air-liquid interface
APTES	(3-aminopropyl)triethoxysilane
BSA	Bovine serum albumin
CAD	Computer-aided design
cm	Centimeter
DAPI	4',6-diamidino-2-phenylindole
DI	Deionized
DIC	Differential interference contrast
DM	Differentiation media
DNA	Deoxyribonucleic acid
DPG	Dipropylene glycol
DT	Diffusion coefficient
DTT	Dithiothreitol
ECM	Extracellular matrix

EDC	1-ethyl-3-(-3-dimethylaminopropyl) carbodiimide hydrochloride
EdU	5-ethyl-2'-deoxyuridine
EM	Expansion media
ESEM	Environmental scanning electron microscopy
F-actin	Filamentous actin
G'	Storage modulus
G"	Loss modulus
G-actin	Globular actin
GBL	Gamma-butyrolactone
GI	Gastrointestinal
GuHCL	Guanidinium hydrochloric acid
h	Hour
HPLC	High pressure liquid chromatography
Hz	Hertz
kb	Boltzmann's constant
kPa	KiloPascal
LVR	Linear viscoelastic region
m	Meter
MALLS	Multi-angle laser light scattering
MDa	MegaDalton
min	Minute
mL	Milliliter
mm	Millimeter

mol	Mole
MSD	Mean square displacement
η*	Complex viscosity
NBF	Neutral buffered formalin
NHS	N-Hydroxysuccinimide
nm	Nanometer
p	P-value
Pa	Pascal
PBS	Phosphate buffer solution
PDMS	Polydimethylsiloxane
PLA	Polylactic acid
PTFE	Polytetrafluoroethylene
PTS	Proline/threonine/serine
RFU	Relative fluorescence units
RPMI 1640	Roswell Park Memorial Institute 1640
s	Second
SEM	Scanning electron microscopy
SM	Stem media
TEER	Transepithelial electrical resistance
TEG	Tetraethylene glycol
TMOE	Trimethylolethane
TSH	Triarylsufonium hexafluoroantimonate
VIP	Vasointestinal peptide

WGA	Wheat germ agglutin
YAP1	Yes-associated protein 1

CHAPTER 1: INTRODUCTION AND BACKGROUND INFORMATION

1.1. Tissue engineering applications in regenerative medicine and drug screening

1.1.1. Regenerative medicine and the role of stem cells in tissue engineering

A heavy focus in biomedical research in recent years has been the improved and expanded development of tissue engineering applications, particularly in terms of physiologically-relevant tissue synthesis. This field of research is of significant importance, as the cost (both in currency and in lives lost) of organ failure and complications with organ transplants is very high. According to the Organ Procurement and Transplantation Network, the number of total organ transplants has increased each year since 2012, from 28,059 in 2012 to 39,718 in 2019 [1]. As of March 2020, there are 123,407 patients on the waiting list for organ transplants of all types [1]. Unfortunately, the number of donors available for organ donation is remarkably smaller, with 19,252 organ donors in 2019 [1]. It was estimated that approximately 6,200 patients died while awaiting organ transplant in 2019 [1]. Going beyond the actual difficulties of acquiring an organ for transplant, it is even more difficult to ensure a match between a donor and a recipient due to blood-type, tissue-type, and antibody match requirements between donor and recipient tissue [2]. Also, the material cost for the harvest, transport, transplant, and maintenance of donor tissue is staggeringly high, reaching as high as an average of ~$1.65 million per transplant for heart transplants and associated care in 2019 [3]. With these high costs, there is considerable drive to develop alternatives to donor tissue transplant.

One particular area of research in reducing the necessity and cost of tissue replacement is

regenerative medicine. This field of research combines molecular biology and tissue engineering around the idea of using stem cells and *in vitro* cell culture to repair and replace human tissue for patients who currently have untreatable or incurable illnesses or injuries. The field of regenerative medicine has grown significantly in the past two decades, spawning Food and Drug Administration (FDA) approved therapies encompassing biologic treatments, cell-based medical devices, and biopharmaceuticals [4, 5]. While these technologies are usable for *in situ* tissue repair, there is still a gap in the development of synthetic tissue replacement [5]. Ideally, regenerative medicine could use a patient's own cells to create replacement tissue for implantation, reducing transplant costs and the risk of host rejection [6]. Unfortunately, the complexity of creating an entire organ, complete with multiple layers of distinct tissue and a myriad of distinct metabolic factors, makes full tissue generation on a large scale exceedingly difficult [6]. To that end, many biomedical researchers have pursued "lab-on-a-chip" cell culture systems, designed via controlled scaffold fabrication, tissue self-assembly, and three-dimensional (3D) bioprinting of tissue [5]. Lab-on-a-chip systems are designed to mimic biological tissue (including fluid flow and cell co-culture) on a small scale, allowing for high throughput screening of the effects of drugs and other environmental stimuli [7]. While this microengineering of cell culture may seem counter-intuitive for the development of large, potentially implantable tissue, these systems allow for the complexity of each *in vivo* tissue type to be suitably replicated *in vitro*, which could then lead to larger scale tissue culture under these improved conditions [7].

A particularly important factor in successful lab-on-a-chip culture is the propagation and maintenance of stem cell lines from donor tissue [8]. It is difficult to properly mimic *in vivo* conditions for stem cell growth, as a myriad of chemical and physical factors are required to

control their viability, migration, and differentiation into various cell types within the tissue [8]. Without properly maintaining these stem cell lines, it is entirely possible that the karyotype/phenotype of any *in vitro* tissue will not match with *in vivo* tissue function [8]. While replicating the exact *in vivo* chemical microenvironment around stem cells is difficult due to the large number of chemical factors and metabolites found physiologically, the physical microenvironment of this tissue could be more easily replicable [9]. The structural microenvironment supporting stem cells can have far-reaching effects on the eventual biological structure growing from those stem cells; for example, increases in matrix stiffness have been shown to directly influence stem cell differentiation between bone cells and fat cells with human mesenchymal stem cells [10]. By placing stem cells in a physiologically mismatched environment, they can grow too quickly or too slowly, differentiate into undesirable cell types, or die [11]. In order to better characterize environment effects on stem cells, a compartmentalized, orderly cell support system is desirable. Such a structure would allow for direct observation of independent variable effects on stem cells, while minimizing interference from other types of cells. The synthetic method used to create a lab-on-a-chip system is crucial for properly developing the physical microenvironment around stem cells in culture, guiding their differentiation into biomimetic tissue [12].

1.1.2. Various synthetic methods and applications of lab-on-a-chip cell culture

One of the goals of a microengineered lab-on-a-chip platform is to recapitulate organ-level function on the microscale, and the success of this goal can be heavily affected by the synthetic method chosen. Many different synthesis methods can be found in the literature for recreating complex tissue on a lab-on-a-chip. One popular method is using decellularized native

tissue as a scaffold, reseeding it with cultured cells, and allowing the native microenvironment of the decellularized matrix to guide tissue growth [13]. This process involves the removal of cells and most chemical factors, while (theoretically) maintaining the composition, microstructure, and mechanical properties of *in vivo* tissue [5]. While promising, there are challenges for the successful implementation of decellularized tissue as an *in vitro* scaffold. Because the native extracellular matrix (ECM) operates in conjunction with a number of signaling molecules and cell-anchored proteins, the decellularization step could compromise the microstructure and mechanical properties of the tissue and lead to unsuccessful tissue recapitulation [14]. Similarly, because protein components of the native matrix are regularly replaced by host cells, the loss of live cells in the decellularization process could lead to scaffold degradation over time [5].

Another strategy for replication of *in vivo* microstructure is the use of 3D printing with cell-containing bioink on a hydrogel scaffold [5]. This technique involves using a soft hydrogel base, typically containing natural ECM polymers such as collagen, and using 3D printing techniques (such as inkjet printing, microextrusion, or laser-guided printing) to spatially organize different cell types into a native-like structure [15, 16]. With a number of significant improvements in spatial resolution on the microscale in recent years, the microstructure of complex tissues can be recapitulated *in vitro*, though whole-organ tissue printing for transplantation has still not been achieved [16]. 3D bioprinting excels in seeding cells and extracellular components layer-by-layer with compositional control, allowing for the creating of native-like 3D scaffolds for cell growth [16]. This successive layer-by-layer approach allows for increased *in vitro* tissue complexity, as *in vivo* tissues typically contain various epithelial, mesothelial, and endothelial layers [17]. A main limiting factor for this technology currently is an incomplete understanding of the multitude of metabolic and growth factors needed for exact

in vivo tissue replication [15]. Another challenge currently facing 3D bioprinting is maintaining cell viability while achieving adequate spatial resolution; because microstructures with higher resolution necessarily take more time to be printed, cell viability (and subsequent tissue viability) could be decreased compared to other synthetic methods described in this section [16].

Cellular self-assembly on natural hydrogels with near-native composition and microstructure is also a useful approach for a successful lab-on-a-chip [5]. Self-assembly relies on cellular guidance to recapitulate native tissue by providing them access to biomimetic metabolic factors and ECM components [18]. Using natural hydrogels (which will be discussed herein) as a base for cell culture, the cells have access to ECM bonds and metabolites which are used to form highly sophisticated cell-cell interactions [78]. With multiple cell types and a hydrogel structure with biomimetic composition and structure, cells have shown the ability to self-assemble into complex tissue [19, 20]. This technique offers the benefit of increased simplicity, not requiring sophisticated equipment or access to hard-to-find scaffold materials. Also, by using molding to replicate simple biological structures within a natural hydrogel scaffold, cells can be physically guided to replicate *in vivo* tissue [5, 21]. However, self-assembly does face the challenge of successfully replicating complex native microstructures, such as the alveoli in the lungs, which require very specific microcurvatures and structural composition for formation [22]. It also faces problems of scaffold composition, as exactly recreating *in vivo* ECM composition can prove challenging, especially if multiple levels of tissue are being produced in combination (such as co-culturing epithelial cells, fibroblasts, and vascular cells) [18].

Overall, many synthetic methods with distinct advantages and disadvantages are available for the replication of organ-level tissue function. One particularly important use of

these lab-on-a-chip platforms after successful synthesis is rapidly testing the effects of various drugs and metabolites on cell behavior. Drug screening on *in vitro* tissue with organ-level function is necessary for the development of new pharmaceutical approaches for disease models, as well as for assessment of comparable responses to current drug treatments for *in vivo* and *in vitro* tissue [23]. Some major roadblocks for successful drug screening are the cost and availability of metabolites and tissues of interest, as well as low-throughput models with conventional cell culture [23]. Lab-on-a-chip model systems mitigate these challenges by creating a controlled microengineered system with *in vivo*-like structure, allowing for high-throughput, rapid drug screening using fractional amounts of base tissue and metabolites [23]. For these reasons, the lab-on-a-chip model is an ideal system for advancing knowledge of both *in vitro* organ synthesis and of tissue response to drug and metabolite application.

1.2. Cell culture scaffolding and natural polymers

1.2.1. The extracellular matrix and collagen

Eukaryotic organisms contain a biological structure known as the extracellular matrix (ECM), briefly mentioned in Section 1.1.2, which is responsible for controlling cell migration and cellular mechanical support within the organism. Typically, this structure is formed by proteins and polysaccharides, and can form as a fibrillar network between cells or as a dense sheet structure on which cells can grow and survive, known as a basement membrane [24]. The ECM in humans is primarily composed of different fibrous proteins coupled with various glycosaminoglycans (GAGs), which are sugar complexes integral to the process of cell binding. The fibrous proteins in the ECM commonly include laminins, fibronectins, elastins, and most importantly, collagens [24]. These molecules are largely produced by epithelial cells known as fibroblasts, but other forms of epithelial cells also have roles in ECM molecule secretion [25].

Collagen is a family of proteins characterized by alpha triple helix morphology, forming tropocollagen fibers which can grow into larger linear fibrils or which can be networked together in thinner, non-linear structures [26]. Collagen is the most abundant protein in the body, forming up to 30% of the entire protein content found in humans [11], and plays important roles in mechanical support, wound healing, and cell mobility. While there are at least 16 distinct types of collagen, 80-90% of all collagen found in the body is in the form of type I, type II, or type III collagen, with type I collagen accounting for the bulk of these percentages [27]. The other forms of collagen typically account for specialized connective tissues, and so are not synthesized at high volumes.

Type I collagen consists of two structural units, forming a helix containing two α_1(I) chains and one α_2(I) chain within its tropocollagen structure. These fibers are approximately 300 nm in length and 1.5 nm in diameter, and pack together longitudinally to form thick collagen fibrils. The final structure of type I collagen is formed when these fibrils are networked via various cap proteins [28]. Like most other types of collagen, type I collagen can be identified by its previously-mentioned helical structure, as well the large quantity of Gly-Pro-X motifs found in its structure (with X being any other amino acid) [27].

1.2.2. Advantages, disadvantages, and properties of natural polymers

Caplan demonstrated that nearly 50 different molecules can bind to type I collagen [29], making this material particularly desirable as a substrate for adherent cell culture. It has been shown that purified type I collagen can be used effectively for both *in vivo* and *in vitro* tissue scaffolds [30]. There are noted benefits for using collagen as a scaffold substrate in tissue engineering. Due to its animal-based nature, collagen naturally has a high degree of

biocompatibility, allowing cells to adhere, migrate, differentiate on its surface, and provoke a minimal immune response when used *in vivo* [31]. Included in this advantage is the fact that collagen naturally contains cell binding ligands, which typically come as amino acid sequences with an Arg-Gly-Asp (RGD) motif. These properties have allowed the FDA to approve collagen scaffolds for clinical use in various forms [31]. Collagen is the primary component of the natural ECM. Therefore, the mechanical properties (such as elastic stiffness) of a collagen-based scaffold naturally fall close to that of the *in vivo* environment [30]. Collagen hydrogels are naturally porous, permitting easy diffusion of metabolites and hormones and allowing for cell waste to be excreted. Collagen porosity can also enable angiogenesis under the right conditions, facilitating more self-sustaining tissue constructs [32]. The materials necessary for these scaffolds are derived from animal sources making them cheap and abundant for manufacturing. Finally, for *in vivo* applications, collagen is naturally biodegradable. This biodegradability is advantageous because a main goal of therapeutic tissue engineering is to allow a host's own cells to eventually take over and replace a degrading scaffold over time [33].

Unfortunately, animal-based hydrogels such as collagen do have substantial disadvantages compared to non-animal-based hydrogels or ceramics in tissue engineering. Animal based hydrogels are derived from biological sources; thus, it can prove challenging to homogeneously extract and purify the hydrogel base material. Typically, unwanted contaminant proteins will be included in an extraction. Natural variation between sources can also cause problems in data reproducibility by affecting concentration or protein density batch to batch [30]. While the mechanical properties of collagen scaffolds are similar to *in vivo* conditions, these properties are typically extremely weak, with stiffness in the 10^1 to 10^3 Pa range [34]. This substantially decreases scalability because a collagen scaffold would have poor load-bearing

properties and would be prone to mechanical degradation with increased surface area [34]. Synthetic material properties are typically more tunable (i.e. their properties can be adjusted more easily) than those of biological materials [34]. Finally, the entire procedure of source extraction, purification, and processing requires significant time and expertise, which leads to the cost of animal-based hydrogels significantly exceeding that of common non-biological alternatives. For example, type I rat-tail collagen costs ~2 USD per mg, whereas polyethylene glycol (a common hydrogel base) costs ~.071 USD per mg (Sigma Aldrich, St. Louis, MO) [35, 36].

Ideally, a combination of the low cost, reproducibility, and property control of synthetic materials together with the biocompatibility and structure of biological materials (like collagen) would be used for tissue engineering applications. While pure collagen scaffolds do raise some issues (such as weak material properties and non-specific binding), hybridization with other biological materials or with synthetic materials has yielded promising results. For example, combination with the positively-charged biopolymer chitosan has showed biomimetic mechanical properties while maintaining biocompatibility and cell viability [30]. An example of synthetic/biological hybrid scaffolds, porcine acellular dermal matrix (an ECM extract primarily composed of collagen) has been shown to exhibit increased mechanical properties and even increased cell adhesion when combined with a synthetic polymer such as polydopamine [37].

1.2.3. Physical microenvironment effects in tissue engineering

Beyond composition, the structural microenvironment of a cell scaffold is extremely important for successful growth of biomimetic tissue *in vitro*. Human tissue structure is very complex, with organs displaying a remarkable degree of microenvironment heterogeneity between different layers (such as differences between the epithelium and endothelium) [23].

While using natural polymers as a scaffold can provide approximations of cell binding and signaling networks found in *in vivo* tissue, it can be difficult to recapitulate the physical structure necessary for guiding proper tissue growth, including microcurvature and heterogeneous material properties such as porosity and stiffness [23]. As described in Section 1.1.2, 3D bioprinting is one potential avenue for mitigating this difficulty; however, there are still concerns about resolution on the nano- and micro-scale for these techniques, as well as a high cost of equipment and materials and a high degree of necessary user experience for successful application [15, 16].

Specifically, replicating *in vivo* topography, mechanical properties, and applied tension forces of base-tissue levels is a challenge [38]. This is particularly important for guiding stem cell fate in *in vitro* culture, as it has been demonstrated that these factors can have major effects on stem cell mobility, differentiation, and viability [39, 40, 41]. Mechanical stiffness, briefly touched on in Section 1.2.1, is important for guiding tissue functions, as *in vivo* tissues display an extremely wide range of stiffnesses depending on their role within the body (i.e. bone vs smooth muscle cells) [38]. It has been demonstrated that underlying matrix stiffness has major effects on guiding cell differentiation, which would have significant downstream effects on the development of biomimetic tissue [42]. It is also important that an *in vitro* scaffold has similar response to external forces as native tissue, as mechanotransduction from fluid flow, muscle movement, and other applied forces play roles in cell differentiation and behavior [43]. Finally, the local topography (namely, the roughness and curvature of the surface) of supportive tissue has been shown to have effects on cytoskeletal assembly and stem cell behavior, as changes in nano- or micro-topography has downstream effects on protein clustering and cell signaling through the ECM [38].

1.3. The gastrointestinal tract

1.3.1. Functions and structure of the GI tract

The primary gastrointestinal (GI) tract performs as the digestive system and is responsible for nutrient/water uptake and waste removal. Primarily the GI tract encompasses the mouth, esophagus, stomach, and intestines (small and large), though other organs like the liver and pancreas also play significant accessory roles in digestion [44]. The gastrointestinal wall is formed of four distinct layers: the mucosa, the submucosa, the muscle layer, and an outer layer of connective tissue known as the serosa or adventitia, depending on the surface composition [44]. The innermost layer is the mucosa, which consists primarily of the epithelial cell layer, as well as a connective tissue layer known as the lamina propria and a smooth muscle layer known as the muscularis mucosa [44]. Overall, the mucosa performs critical roles in mucus production and nutrient absorption [44]. The submucosa is a connective tissue layer and primarily provides the GI tract with access to blood and lymphatic vessels [45], while the muscle layer is responsible for swallowing and rhythmic persistalsis along the length of the GI tract [45]. The outermost layer is the serosa or adventitia, depending on whether it is composed of connective tissue (adventitia) or mesothelial cells (serosa) [45]. The serosa typically plays roles in lubrication and protection and is usually found when the GI tract runs through body cavities, whereas an adventitia connects the GI tract to other organs and tissue and is found when the GI tract comes into contact with other organs [45]. While the upper levels of the GI tract display relatively flat epithelial layers, consisting of both squamous cells (esophagus) and columnar cells (stomach), the intestines display unique epithelial microstructures which will be described later in this chapter [44].

1.3.2. The colonic epithelium

The large intestine, commonly referred to as the colon, is the final section of the vertebrate gastrointestinal tract. The colon is largely responsible for water and salt absorption, as well as waste storage. The colon also secretes mucus, which coincides with its presence as a physical containment region for a large variety of gut microbiota [46]. As described previously, the colon displays the primary three inner layers (mucosa, submucosa, and muscle layer), as well as the serosa as an outermost layer [47]. Of primary interest in this project is the mucosa, which contains a layer of self-contained intruding cylindrical structures known as “crypts” oriented perpendicular to the surface of the intestinal lumen. These crypts (also known as the crypts of Lieberkuhn) are approximately 400 μm in depth, and perform major epithelial functions of mucus production and nutrient absorption [48]. Notably, the large intestine does not contain villi, which are finger-like protrusions found within the small intestine and provide additional surface area for nutrient absorption [48].

Crypt biology is remarkable due to its well-ordered nature and the structural segregation created between stem cells and differentiated cells [49]. The basal compartment of the crypt contains colonic stem cells, which proliferate into transient-amplifying cells as they move vertically up the crypt. As cells migrate upwards in the crypt, they begin to fully differentiate and line the intestinal lumen (Fig 1) [50]. The types of cells found in this luminal compartment of the colonic crypt are primarily divided into goblet cells for mucus production, enteroendocrine cells for hormone production, enterocytes for water and salt absorption, and tuft cells for intestinal microbe interaction [51]. Within and on top of the epithelial cells is a two-tiered mucus layer, with a tightly-packed inner layer anchored within the goblet cells and in direct contact with the epithelial lumen, and a more loosely-packed outer layer that contains bacteria and debris [49].

The root source of this structural setup is the extremely rapid level of cell renewal necessary for proper colon function. The colonic epithelium completely renews itself quickly (4-5 days in mammals) and it is key to provide the proper environment in which stem cells can divide and differentiate without mutation or failure [52]. This polarization between stem cells and differentiation cells are driven by basal-to-luminal chemical gradients (such as Wnt, Rspondin, and Noggin), as well as differences in the physical microenvironment between the stem cell niche and the rest of the crypt [21, 53].

The structure-function relationship in the colonic epithelium is extremely pronounced. Thus, proper *in vitro* mimicry of crypt biology has proved challenging. Recent breakthroughs in 2D and 3D culture of mouse-derived colonic epithelial cells enable basic drug screening and cell analysis, despite culture limitations [21, 54]. Despite the difficulty, *in vitro* formation and culture of crypt structures is necessary for properly analyzing stem cell behavior, as well as measuring the effects of cell microenvironment on cell function in bulk tissue behavior.

1.4. Lab-on-a-chip applications for colonic cells

1.4.1. Approaches, advantages, and disadvantages of a colonic lab-on-a-chip

With the unique structure and function of the large intestine, there has been a large focus in the literature on successfully recapitulating native structure in *in vitro* colon models. These models have been achieved as both epithelial-only cultures [54, 55] and more complex co-culture models with other intestinal cell types, including mesenchymal cells [56, 57]. These cultures typically follow one of two pathways: organoid formation [58] or monolayer formation [21, 59]. Organoid formation occurs under chemical conditions similar to those found *in vivo*, including access to growth factors such as R-spondin, Noggin, and epidermal growth factor [60]. When exposed to these conditions and grown on a soft hydrogel layer, intestinal epithelial cells can

self-assemble into a primary spheroid with an enclosed lumen and outward-budding structures [61]. These complexes consist mostly of stem and proliferative cells within the more isolated budding structures and differentiated cells within the interior spheroid, mimicking *in vivo* polarization within intestinal crypts [61]. It has also been demonstrated that co-culture with mesenchymal cells produces a supportive mesenchymal layer surrounding these epithelial organoids [56]. These organoids provide substantial benefits for high-throughput study of cell behavior in response to various drugs and metabolites, have very simple scaffold requirements, and can be used to successfully model diseases in a controlled setting [60]. However, there are some drawbacks towards isolated organoid formation: the lack of an exposed lumen could obscure cell behavior effects in drug screening, and it is difficult to expand these organoids into a larger, biomimetic structure once individual organoids have been formed.

A second approach which can mitigate some of these drawbacks is using a more complicated scaffold (similar to those described in Section 1.1.2) to guide epithelial cell growth in a monolayer. With physiologically-relevant scaffold structure and composition, this monolayer can successfully mimic *in vivo* levels of tissue complexity on a small scale, ideal for a lab-on-a-chip model [60]. Because cells will naturally self-assemble into sophisticated structures under the right conditions, this technique excels at recapitulating organ-level function within *in vitro* culture, as structure is tied directly into function, and a native-like structure will experience different ECM and mechanotransduction conditions than an embedded organoid will [60]. This approach allows for an accessible lumen for drug and metabolite screening, and could feasibly be scaled up with multiple layers of different types of tissue (including a mesenchymal layer) [60]. The disadvantages of this style of fabrication is a more complex scaffolding procedure, which can include the cost of the substrate materials and difficulties constructing the scaffold, as well as

the necessity for controlled chemical gradients of growth factors [60]. Overall, both culture methods have advantages and disadvantages for different biomedical applications. For this dissertation, monolayer formation was the method chosen for study, as the goal of these experiments was comparing *in vivo* and *in vitro* cell behavior and monolayers allow for a closer comparison between those two groups.

1.4.2. Scaffolding for *in vitro* colonic cell culture in the Allbritton lab

In the Allbritton lab, type I collagen derived from rat tails has been used as an effective scaffold substrate for colonic epithelial cell culture. Typically, these scaffolds can be created using one of two design mechanisms: neutral collagen or crosslinked collagen. Neutral collagen, which allows for culture of self-renewing colonic cell monolayers, is formed using two precursor solutions: lyophilized type I collagen in acetic acid and a basic neutralization buffer for pH stabilization. While useful for initial cell behavior studies, this matrix does not easily allow for long-term monolayer growth, as the collagen will contract over time once seeded with cells [62]. In order to mitigate this contraction, 1-ethyl-3-(3-dimethylaminopropyl) carbodiimide (EDC) and N-hydroxysuccinimide (NHS) are used as chemical crosslinking agents to increase matrix mechanical properties [63]. *In vivo* crosslinking is accomplished via enzymatic reactions for both covalent and non-covalent bonding; the lack of enzymatic presence during scaffold synthesis *in vitro* prevents this and is replaced with the EDC-NHS crosslinking, a common carboxyl-amine binding mechanism [64]. Homogeneous crosslinking is accomplished by adding EDC-NHS precursors in the whole gelation process, while gradient crosslinking uses a Transwell system to create a basal-sourced, EDC-NHS gradient across a type I collagen gel.

The cells used for culture in this protocol are primary murine and human colonic epithelial cells, collected directly from crypt tissue samples and seeded onto a hydrogel scaffold.

Colonic cells can be cultured with 4 distinct growth pathways depending on the scaffold composition: patchy monolayer formation, full monolayer formation, organoid formation, and 3D crypt formation. Simple neutral collagen allows for patchy monolayer formation at 1 mg/mL collagen concentration in the scaffold. However, it was found that at lower concentrations (typically starting around 0.5 mg/mL) organoid formation can occur, possibly due to decreased stiffness and/or binding site concentration [59]. Crosslinked type I collagen can be used to produce full monolayers, which grow to confluency across the culture substrate due to the substrate's resistance against contraction. This can be full crosslinking or partial crosslinking, depending on the experimental requirements [59]. Primary organoid formation can be accomplished by culturing within Matrigel © patties, which consist primarily of type IV collagen (a non-fibrillar collagen) and other ECM proteins [53]. Finally, by using a polymeric stamp to shape crosslinked collagen into cylinders roughly the size and shape of intestinal crypts, in addition to introducing chemical gradients to drive polarization (similar to *in vivo* conditions), seeded colonic cells have been successfully grown as an *in vitro* crypt model with natural polarization between stem cells at the base of the crypt and differentiated cells closer to the epithelial lumen [21]. These varied culture techniques allow for varied experimental approaches to drug screening, metabolite secretion and collection, and cell behavior analysis.

1.5. Scope of this dissertation

The primary focus of this work was two-fold: analyzing the material and chemical properties of *in vitro* colonic mucus, and analyzing the effects of scaffold microcurvature on intestinal cell behavior *in vitro*. Both aspects of this dissertation are rooted in materials science, highlighting the connection between material properties and biological function. Chapter 2 describes the rheological and biochemical properties of both *in vitro* and *ex vivo* colonic mucus,

highlighting their similarities and differences. Chapter 3 highlights the experimental and modeled diffusion of an organosilane inside of a controlled chamber for the purpose of gradient surface alteration for tissue engineering purposes. Chapter 4 uses this gradient diffusion of silane to alter the microcurvature of PDMS pillar stamps, which were then used to create collagen scaffolds for *in vitro* crypt synthesis and analyze the effects of microcurvature on epithelial cell behavior.

1.6. Figures

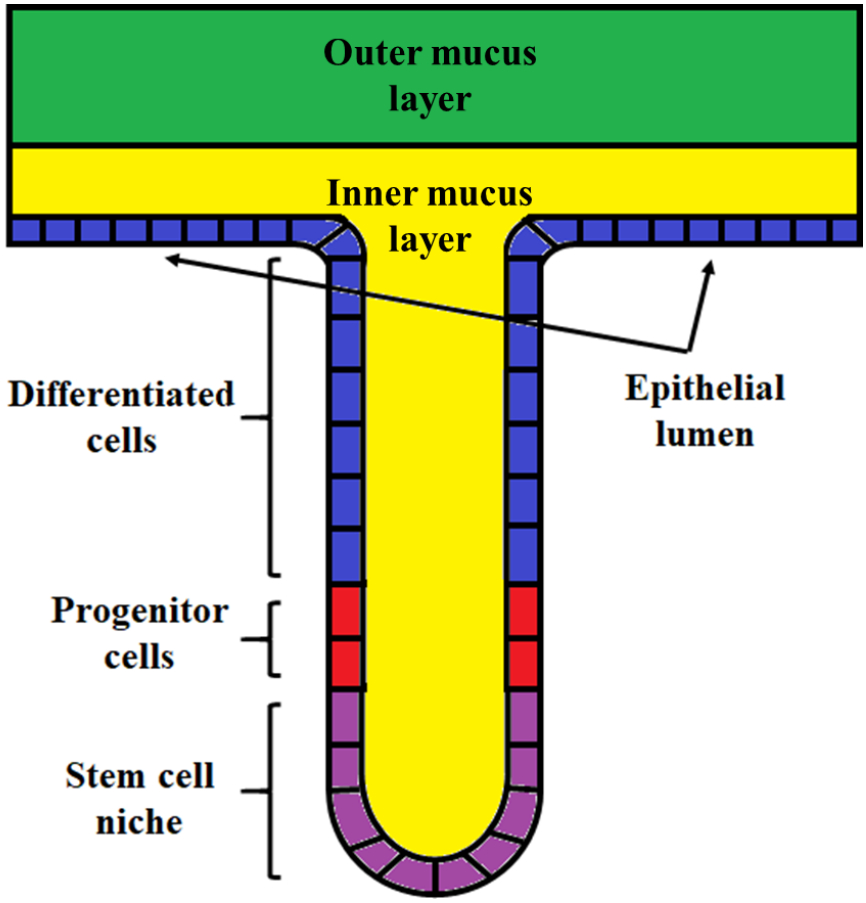

Figure 1.1. Diagram of intestinal crypt and mucus structure. The intestinal crypt, approximately 400 μm in humans, displays natural polarization between stem cells and differentiated cells moving from the base to the lumen of the epithelium. Within the crypt and against the epithelial layer is a tightly packed inner mucus layer, created by goblet cells, which transitions into a more loosely-packed outer layer of mucus containing bacteria and cell/fecal debris.

REFERENCES

1. 2019 Annual Report of the U.S. Organ Procurement and Transplantation Network and the Scientific Registry of Transplant Recipients: Transplant Data 1994-2003. Department of Health and Human Services, Health Resources and Services Administration, Healthcare Systems Bureau, Division of Transplantation, Rockville, MD; United Network for Organ Sharing, Richmond, VA; University Renal Research and Education Association, Ann Arbor, MI.

2. Snyder, T. M.; Khush, K. K.; Valantine, H. A.; Quake, S. R. Universal Noninvasive Detection of Solid Organ Transplant Rejection. *PNAS* **2011**, *108* (15), 6229–6234. https://doi.org/10.1073/pnas.1013924108.

3. Bentley, T. Scott. 2020 U.S. Organ and Tissue Transplants. **2020**, 24.

4. Falanga, V.; Sabolinski, M. A Bilayered Living Skin Construct (APLIGRAF) Accelerates Complete Closure of Hard-to-Heal Venous Ulcers. *Wound Repair Regen* **1999**, *7* (4), 201–207. https://doi.org/10.1046/j.1524-475x.1999.00201.x.

5. Mao, A. S.; Mooney, D. J. Regenerative Medicine: Current Therapies and Future Directions. *Proc Natl Acad Sci U S A* **2015**, *112* (47), 14452–14459. https://doi.org/10.1073/pnas.1508520112.

6. Jain, A.; Bansal, R. Applications of Regenerative Medicine in Organ Transplantation. *J Pharm Bioallied Sci* **2015**, *7* (3), 188–194. https://doi.org/10.4103/0975-7406.160013.

7. Dittrich, P. S.; Manz, A. Lab-on-a-Chip: Microfluidics in Drug Discovery. *Nature Reviews Drug Discovery* **2006**, *5* (3), 210–218. https://doi.org/10.1038/nrd1985.

8. Gupta, K.; Kim, D.-H.; Ellison, D.; Smith, C.; Kundu, A.; Tuan, J.; Suh, K.-Y.; Levchenko, A. Lab-on-a-Chip Devices as an Emerging Platform for Stem Cell Biology. *Lab Chip* **2010**, *10* (16), 2019–2031. https://doi.org/10.1039/C004689B.

9. Xing, F.; Li, L.; Zhou, C.; Long, C.; Wu, L.; Lei, H.; Kong, Q.; Fan, Y.; Xiang, Z.; Zhang, X. Regulation and Directing Stem Cell Fate by Tissue Engineering Functional Microenvironments: Scaffold Physical and Chemical Cues https://www.hindawi.com/journals/sci/2019/2180925/ (accessed Mar 3, 2020). https://doi.org/10.1155/2019/2180925.

10. Reilly, G. C.; Engler, A. J. Intrinsic Extracellular Matrix Properties Regulate Stem Cell Differentiation. *J Biomech* **2010**, *43* (1), 55–62. https://doi.org/10.1016/j.jbiomech.2009.09.009.

11. Gattazzo, F.; Urciuolo, A.; Bonaldo, P. Extracellular Matrix: A Dynamic Microenvironment for Stem Cell Niche. *Biochim. Biophys. Acta* **2014**, *1840* (8), 2506–2519. https://doi.org/10.1016/j.bbagen.2014.01.010.

12. Ertl, P.; Sticker, D.; Charwat, V.; Kasper, C.; Lepperdinger, G. Lab-on-a-Chip Technologies for Stem Cell Analysis. *Trends in Biotechnology* **2014**, *32* (5), 245–253. https://doi.org/10.1016/j.tibtech.2014.03.004.

13. Crapo, P. M.; Gilbert, T. W.; Badylak, S. F. An Overview of Tissue and Whole Organ Decellularization Processes. *Biomaterials* **2011**, *32* (12), 3233–3243. https://doi.org/10.1016/j.biomaterials.2011.01.057.

14. Badylak, S. F.; Taylor, D.; Uygun, K. Whole-Organ Tissue Engineering: Decellularization and Recellularization of Three-Dimensional Matrix Scaffolds. *Annu Rev Biomed Eng* **2011**, *13*, 27–53. https://doi.org/10.1146/annurev-bioeng-071910-124743.

15. Ozbolat, I. T. Bioprinting Scale-up Tissue and Organ Constructs for Transplantation. *Trends in Biotechnology* **2015**, *33* (7), 395–400. https://doi.org/10.1016/j.tibtech.2015.04.005.

16. Murphy, S. V.; Atala, A. 3D Bioprinting of Tissues and Organs. *Nat. Biotechnol.* **2014**, *32* (8), 773–785. https://doi.org/10.1038/nbt.2958.

17. Lachaud, C. C.; Rodriguez-Campins, B.; Hmadcha, A.; Soria, B. Use of Mesothelial Cells and Biological Matrices for Tissue Engineering of Simple Epithelium Surrogates. *Front Bioeng Biotechnol* **2015**, *3*. https://doi.org/10.3389/fbioe.2015.00117.

18. Thomas, D.; Gaspar, D.; Sorushanova, A.; Milcovich, G.; Spanoudes, K.; Mullen, A. M.; O'Brien, T.; Pandit, A.; Zeugolis, D. I. Scaffold and Scaffold-Free Self-Assembled Systems in Regenerative Medicine. *Biotechnology and Bioengineering* **2016**, *113* (6), 1155–1163. https://doi.org/10.1002/bit.25869.

19. Ader, M.; Tanaka, E. M. Modeling Human Development in 3D Culture. *Curr. Opin. Cell Biol.* **2014**, *31*, 23–28. https://doi.org/10.1016/j.ceb.2014.06.013.

20. Lancaster, M. A.; Knoblich, J. A. Organogenesis in a Dish: Modeling Development and Disease Using Organoid Technologies. *Science* **2014**, *345* (6194), 1247125. https://doi.org/10.1126/science.1247125.

21. Wang, Y.; Ahmad, A. A.; Sims, C. E.; Magness, S. T.; Allbritton, N. L. In Vitro Generation of Colonic Epithelium from Primary Cells Guided by Microstructures. *Lab on a chip* **2014**. https://doi.org/10.1039/c3lc51353j.

22. Knudsen, L.; Ochs, M. The Micromechanics of Lung Alveoli: Structure and Function of Surfactant and Tissue Components. *Histochem Cell Biol* **2018**, *150* (6), 661–676. https://doi.org/10.1007/s00418-018-1747-9.

23. Chi, C.-W.; Ahmed, A. R.; Dereli-Korkut, Z.; Wang, S. Microfluidic Cell Chips for High-Throughput Drug Screening. *Bioanalysis* **2016**, *8* (9), 921–937. https://doi.org/10.4155/bio-2016-0028.

24. Wiltz, D.; Arevalos, C. A.; Balaoing, L. R.; A. Blancas, A.; Sapp, M. C.; Zhang, X.; Grande-Allen, K. J. Extracellular Matrix Organization, Structure, and Function. *Calcific Aortic Valve Disease* **2013**. https://doi.org/10.5772/52842.

25. Lien, S.-M.; Ko, L.-Y.; Huang, T.-J. Effect of Pore Size on ECM Secretion and Cell Growth in Gelatin Scaffold for Articular Cartilage Tissue Engineering. *Acta Biomater* **2009**, *5* (2), 670–679. https://doi.org/10.1016/j.actbio.2008.09.020.

26. Lodish, H.; Berk, A.; Zipursky, S. L.; Matsudaira, P.; Baltimore, D.; Darnell, J. *Molecular Cell Biology*, 4th ed.; W. H. Freeman, 2000.

27. Lodish, H.; Berk, A.; Zipursky, S. L.; Matsudaira, P.; Baltimore, D.; Darnell, J. Collagen: The Fibrous Proteins of the Matrix. *Molecular Cell Biology. 4th edition* **2000**.

28. Weber, K. T.; Sun, Y.; Tyagi, S. C.; Cleutjens, J. P. Collagen Network of the Myocardium: Function, Structural Remodeling and Regulatory Mechanisms. *J. Mol. Cell. Cardiol.* **1994**, *26* (3), 279–292. https://doi.org/10.1006/jmcc.1994.1036.

29. Xu, Y.; Gurusiddappa, S.; Rich, R. L.; Owens, R. T.; Keene, D. R.; Mayne, R.; Höök, A.; Höök, M. Multiple Binding Sites in Collagen Type I for the Integrins A1β1 and A2β1. *J. Biol. Chem.* **2000**, *275* (50), 38981–38989. https://doi.org/10.1074/jbc.M007668200.

30. Dong, C.; Lv, Y. Application of Collagen Scaffold in Tissue Engineering: Recent Advances and New Perspectives. *Polymers* **2016**, *8* (2), 42. https://doi.org/10.3390/polym8020042.

31. O'Brien, F. J. Biomaterials & Scaffolds for Tissue Engineering. *Materials Today* **2011**, *14* (3), 88–95. https://doi.org/10.1016/S1369-7021(11)70058-X.

32. Chan, E. C.; Kuo, S.-M.; Kong, A. M.; Morrison, W. A.; Dusting, G. J.; Mitchell, G. M.; Lim, S. Y.; Liu, G.-S. Three Dimensional Collagen Scaffold Promotes Intrinsic Vascularisation for Tissue Engineering Applications. *PLoS ONE* **2016**, *11* (2), e0149799. https://doi.org/10.1371/journal.pone.0149799.

33. Mikos; McIntire; Anderson; Babensee. Host Response to Tissue Engineered Devices. *Adv. Drug Deliv. Rev.* **1998**, *33* (1–2), 111–139. https://doi.org/10.1016/s0169-409x(98)00023-4.

34. Meyers, M. A.; Chen, P.-Y.; Lin, A. Y.-M.; Seki, Y. Biological Materials: Structure and Mechanical Properties. *Progress in Materials Science* **2008**, *53* (1), 1–206. https://doi.org/10.1016/j.pmatsci.2007.05.002.

35. "Collagen, Type I Solution from Rat Tail C3867." *Sigma-Aldrich*. Accessed March 3, 2020. http://www.sigmaaldrich.com/catalog/product/sigma/c3867.

36. "Poly(ethylene Glycol) 81300." *Sigma-Aldrich*. Accessed March 3, 2020. http://www.sigmaaldrich.com/catalog/product/aldrich/81300.

37. Hu, Y.; Dan, W.; Xiong, S.; Kang, Y.; Dhinakar, A.; Wu, J.; Gu, Z. Development of Collagen/Polydopamine Complexed Matrix as Mechanically Enhanced and Highly Biocompatible Semi-Natural Tissue Engineering Scaffold. *Acta Biomater* **2017**, *47*, 135–148. https://doi.org/10.1016/j.actbio.2016.10.017.

38. Han, Y. L.; Wang, S.; Zhang, X.; Li, Y.; Huang, G.; Qi, H.; Pingguan-Murphy, B.; Li, Y.; Lu, T. J.; Xu, F. Engineering Physical Microenvironment for Stem Cell Based Regenerative Medicine. *Drug Discovery Today* **2014**, *19* (6), 763–773. https://doi.org/10.1016/j.drudis.2014.01.015.

39. Swift, J.; Ivanovska, I. L.; Buxboim, A.; Harada, T.; Dingal, P. C. D. P.; Pinter, J.; Pajerowski, J. D.; Spinler, K. R.; Shin, J.-W.; Tewari, M.; et al. Nuclear Lamin-A Scales with Tissue Stiffness and Enhances Matrix-Directed Differentiation. *Science* **2013**, *341* (6149). https://doi.org/10.1126/science.1240104.

40. Stevens, M. M.; George, J. H. Exploring and Engineering the Cell Surface Interface. *Science* **2005**, *310* (5751), 1135–1138. https://doi.org/10.1126/science.1106587.

41. Vincent, L. G.; Engler, A. J. Post-Degradation Forces Kick In. *Nature Materials* **2013**, *12* (5), 384–386. https://doi.org/10.1038/nmat3636.

42. Wen, J. H.; Vincent, L. G.; Fuhrmann, A.; Choi, Y. S.; Hribar, K. C.; Taylor-Weiner, H.; Chen, S.; Engler, A. J. Interplay of Matrix Stiffness and Protein Tethering in Stem Cell Differentiation. *Nature Materials* **2014**, *13* (10), 979–987. https://doi.org/10.1038/nmat4051.

43. Wozniak, M. A.; Chen, C. S. Mechanotransduction in Development: A Growing Role for Contractility. *Nature Reviews Molecular Cell Biology* **2009**, *10* (1), 34–43. https://doi.org/10.1038/nrm2592.

44. Reed, K. K.; Wickham, R. Review of the Gastrointestinal Tract: From Macro to Micro. *Seminars in Oncology Nursing* **2009**, *25* (1), 3–14. https://doi.org/10.1016/j.soncn.2008.10.002.

45. Tortora, G. J.; Derrickson, B. H. *Principles of Anatomy and Physiology*; John Wiley & Sons, 2018.

46. Large Intestine Anatomy: Gross Anatomy, Histology, Natural Variants. **2019**.

47. Michailova, K. N.; Usunoff, K. G. *Serosal Membranes (Pleura, Pericardium, Peritoneum): Normal Structure, Development and Experimental Pathology*; Springer Science & Business Media, 2006.

48. Clevers, H. The Intestinal Crypt, A Prototype Stem Cell Compartment. *Cell* **2013**, *154* (2), 274–284. https://doi.org/10.1016/j.cell.2013.07.004.

49. Baker, A.-M.; Cereser, B.; Melton, S.; Fletcher, A. G.; Rodriguez-Justo, M.; Tadrous, P. J.; Humphries, A.; Elia, G.; McDonald, S. A. C.; Wright, N. A.; et al. Quantification of Crypt and Stem Cell Evolution in the Normal and Neoplastic Human Colon. *Cell Rep* **2014**, *8* (4), 940–947. https://doi.org/10.1016/j.celrep.2014.07.019.

50. Barker, N. Adult Intestinal Stem Cells: Critical Drivers of Epithelial Homeostasis and Regeneration. *Nat. Rev. Mol. Cell Biol.* **2014**, *15* (1), 19–33. https://doi.org/10.1038/nrm3721.

51. Sarmento, B. *Concepts and Models for Drug Permeability Studies: Cell and Tissue Based In Vitro Culture Models*; 2015.

52. van der Flier, L. G.; Clevers, H. Stem Cells, Self-Renewal, and Differentiation in the Intestinal Epithelium. *Annu. Rev. Physiol.* **2009**, *71*, 241–260. https://doi.org/10.1146/annurev.physiol.010908.163145.

53. Gjorevski, N.; Sachs, N.; Manfrin, A.; Giger, S.; Bragina, M. E.; Ordóñez-Morán, P.; Clevers, H.; Lutolf, M. P. Designer Matrices for Intestinal Stem Cell and Organoid Culture. *Nature* **2016**, *539* (7630), 560–564. https://doi.org/10.1038/nature20168.

54. Sato, T.; Stange, D. E.; Ferrante, M.; Vries, R. G. J.; Van Es, J. H.; Van den Brink, S.; Van Houdt, W. J.; Pronk, A.; Van Gorp, J.; Siersema, P. D.; et al. Long-Term Expansion of Epithelial Organoids from Human Colon, Adenoma, Adenocarcinoma, and Barrett's Epithelium. *Gastroenterology* **2011**, *141* (5), 1762–1772. https://doi.org/10.1053/j.gastro.2011.07.050.

55. Jung, P.; Sato, T.; Merlos-Suárez, A.; Barriga, F. M.; Iglesias, M.; Rossell, D.; Auer, H.; Gallardo, M.; Blasco, M. A.; Sancho, E.; et al. Isolation and in Vitro Expansion of Human Colonic Stem Cells. *Nature Medicine* **2011**, *17* (10), 1225–1227. https://doi.org/10.1038/nm.2470.

56. Ootani, A.; Li, X.; Sangiorgi, E.; Ho, Q. T.; Ueno, H.; Toda, S.; Sugihara, H.; Fujimoto, K.; Weissman, I. L.; Capecchi, M. R.; et al. Sustained in Vitro Intestinal Epithelial Culture within a Wnt-Dependent Stem Cell Niche. *Nature Medicine* **2009**, *15* (6), 701–706. https://doi.org/10.1038/nm.1951.

57. Li, X.; Nadauld, L.; Ootani, A.; Corney, D. C.; Pai, R. K.; Gevaert, O.; Cantrell, M. A.; Rack, P. G.; Neal, J. T.; Chan, C. W.-M.; et al. Oncogenic Transformation of Diverse Gastrointestinal Tissues in Primary Organoid Culture. *Nature Medicine* **2014**, *20* (7), 769–777. https://doi.org/10.1038/nm.3585.

58. Mahe, M. M.; Aihara, E.; Schumacher, M. A.; Zavros, Y.; Montrose, M. H.; Helmrath, M. A.; Sato, T.; Shroyer, N. F. Establishment of Gastrointestinal Epithelial Organoids. *Current Protocols in Mouse Biology* **2013**, *3* (4), 217–240. https://doi.org/10.1002/9780470942390.mo130179.

59. Wang, Y.; DiSalvo, M.; Gunasekara, D. B.; Dutton, J.; Proctor, A.; Lebhar, M. S.; Williamson, I. A.; Speer, J.; Howard, R. L.; Smiddy, N. M.; et al. Self-Renewing Monolayer of Primary Colonic or Rectal Epithelial Cells. *Cell Mol Gastroenterol Hepatol* **2017**, *4* (1), 165-182.e7. https://doi.org/10.1016/j.jcmgh.2017.02.011.

60. Nakamura, T.; Sato, T. Advancing Intestinal Organoid Technology Toward Regenerative Medicine. *Cellular and Molecular Gastroenterology and Hepatology* **2018**, *5* (1), 51–60. https://doi.org/10.1016/j.jcmgh.2017.10.006.

61. Sato, T.; Vries, R. G.; Snippert, H. J.; van de Wetering, M.; Barker, N.; Stange, D. E.; van Es, J. H.; Abo, A.; Kujala, P.; Peters, P. J.; et al. Single Lgr5 Stem Cells Build Crypt-Villus Structures in Vitro without a Mesenchymal Niche. *Nature* **2009**, *459* (7244), 262–265. https://doi.org/10.1038/nature07935.

62. Hapach, L. A.; VanderBurgh, J. A.; Miller, J. P.; Reinhart-King, C. A. Manipulation Ofin Vitrocollagen Matrix Architecture for Scaffolds of Improved Physiological Relevance. *Phys. Biol.* **2015**, *12* (6), 061002. https://doi.org/10.1088/1478-3975/12/6/061002.

63. Shepherd, D. V.; Shepherd, J. H.; Ghose, S.; Kew, S. J.; Cameron, R. E.; Best, S. M. The Process of EDC-NHS Cross-Linking of Reconstituted Collagen Fibres Increases Collagen Fibrillar Order and Alignment. *APL Mater* **2015**, *3* (1). https://doi.org/10.1063/1.4900887.

64. Sung, H.-W.; Chang, W.-H.; Ma, C.-Y.; Lee, M.-H. Crosslinking of Biological Tissues Using Genipin and/or Carbodiimide. *Journal of Biomedical Materials Research Part A* **2003**, *64A* (3), 427–438. https://doi.org/10.1002/jbm.a.10346.

CHAPTER 2: IN VITRO GUT MUCUS COLLECTION AND ANALYSIS USING AN AIR-LIQUID INTERFACE

2.1. Introduction and background

2.1.1. The roles and structure of mucus in the GI tract

The mucosal layer of the gastrointestinal (GI) tract is the luminal facing side of the tissue, primarily composed of the epithelial layer of cells on top of a loose layer of connective tissue called the lamina propria [1]. One of the primary functions of the epithelial layer is the production of mucus, which plays a major role in protection from pathogens, cell signaling, and in lubrication for waste removal within the GI tract [1]. Mucus is structured as a large-structure natural polymer whose primary polymeric components are large glycoprotein complexes called mucins, while also containing various inorganic salts, enzymes and other glycoproteins [2]. Mucus is primarily produced by goblet cells within the digestive system, as well as in the mucosal membranes and submucosal glands in the reproductive and respiratory systems, with various types of mucus being primarily produced in different systems (e.g. MUC5B in the lungs, MUC2 in the large intestine, etc.) [3, 4, 5]. Mucins typically consist of nearly 80% carbohydrates, bonded to a protein backbone which exhibits high levels of proline, threonine, and serine organized into segments called PTS sequences [6]. The length and variation in repetition of these PTS sequences determines the structure and function of these mucus complexes, giving them either transmembrane or gel-forming properties [6]. Transmembrane mucins (such as MUC1 and MUC4) have a small C-terminus domain anchored within the cell

membrane and extending into the cytoplasm and a larger N-terminus domain bonded outside of the cell [7]. These mucins are used to connect to larger gel-forming mucins, attaching the larger mucus complexes to the epithelial cell layer and maintaining a contiguous mucus layer [7]. Individual types of mucins are determined by the number and organization of their protein domains, as well as by the number of individual mucin subdomains found within the monomeric structure [6, 8]. Mucus layers are directly exposed to large amounts of bacteria and debris; as such, they are regularly replaced by new mucus via natural microfluidic processes such as mucociliary clearance via cilia motion in the lungs, or peristaltic fluid flow within the intestine [9, 10]. Mucus clearance rates have been observed to be as rapid as 1 h in the gut, indicating the importance of maintaining a healthy, continuous layer of mucus for bacterial protection in the GI tract [10].

2.1.2. Mucins and mucus structure in the GI tract

The types of mucins and their organization varies along the length of the GI tract. Two general types of mucus organization can be observed in this system: a single layer of loose, gel-like mucus (such as in the small intestine), or a two-layer system with a loosely-packed outer layer and a much more compact inner layer up against the epithelial cell wall (such as in the stomach or large intestine) [11, 12, 13]. The mouth and esophagus do not maintain a consistent mucus layer, though salivary glands do produce mucus (notably MUC5B and MUC7) [14]. The two-tiered mucus layer in the stomach is composed primarily of MUC5AC and MUC6 [12]. The focus of this project is on the intestines, specifically the two-tiered mucus layer in the large intestine. Mucus in the large intestine is primarily based on the monomerically large MUC2, which has a weight of ~2.5 MDa in stiff rod-like backbones within covalently-bonded gel networks, though MUC5AC is present as well [15]. The inner layer of mucus, measuring

approximately 100 µm, is tightly packed in spontaneously-formed flat sheets and is usually devoid of bacteria, indicating a lack of porosity towards larger organisms and debris [16]. This

layer of mucus is attached to the goblet cells within the epithelial cell wall, and undergoes a clearance rate of approximately one hour [10]. At the luminal edge of this inner layer of mucus, the mucus complex transitions from tightly packed sheets into a looser, larger polymeric network that can be hundreds of microns thick that is held together by cysteine disulfide bonds [17]. The exact mechanisms for the transition from inner layer mucus to outer layer mucus are still poorly understood, though it is likely driven by proteolytic cleavages [17]. This outer layer is penetrable by bacteria, debris, and fecal matter, and undergoes regular clearance due to fecal pressure and fluid flow within the colon [17].

2.1.3. The human intestine and its culture in vitro

The large intestine displays a unique native physical structure, hallmarked by the presence of ~400 μm cylindrical cavities embedded in the epithelial wall known as *intestinal crypts*. These crypts display a polarization between stem cells at the basal level of the crypt and differentiated cells closer to the luminal side of the epithelium [18]. Just above the stem cell compartment of the crypt, progenitor cells lead to levels of differentiated cells such as enterocytes, enteroendocrine cells, and tuft cells, among others [18]; this natural polarization is primarily driven by chemical gradients from the base of the crypt, including Wnt, Rspondin, and Noggin, which are partially responsible for driving cell proliferation [36]. Goblet cells can be found along the inner ring of these crypts closer to the lumen, and serve as anchor points for the inner layer of intestinal mucus in addition to their primary role of mucus production [17]. In order to effectively recapitulate native intestinal behavior, it is necessary to replicate the native mucus layer in an *in vitro* tissue engineering capacity, fulfilling the roles of protection, signaling, and lubrication found *in vivo* [19]. Specifically, mucus layer thickness and other physical properties such as porosity, elasticity, and viscosity are of particular importance, as *in vivo* tissue

displays a complex balance between microbiota growth in the outer layer of mucus (and their generated compounds such as butyrate) and protection from bacterial growth in the inner layer of mucus and along the epithelial cell layer [20].

2.1.4. Current methods of in vitro mucus synthesis and analysis

There are fundamental challenges in effectively recapitulating a contiguous mucus layer in *in vitro* tissue culture. The complex chemical composition of native mucus is very difficult to replicate, as the entire mucus layer is composed of a complex combination of mucins, lipids, and other proteins [19]. Also, the entire group of metabolic factors responsible for instigating mucus secretion is not fully understood, which limits researchers' ability to replicate with *in vitro* media conditions. For example, vasointestinal peptide (VIP) has been demonstrated to stimulate goblet cell growth and mucus production in the gut, but is not commonly included in cell culture media [21]. It has also been demonstrated that exposure of the mucus layer to various bacteria and pathogens *in vivo* can cause significant alterations in the observed mucus layer, which is difficult to replicate in more sterile *in vitro* tissue culture conditions without significant loss in cell viability [19]. Finally, with typical cell culture techniques, the epithelial cell layer is submerged and regularly washed with fresh media, making it difficult for a continuous mucus layer to be developed and maintained across the surface of the cells due to regular convective mixing [22, 23]. In order to combat these shortcomings, inspiration was drawn from mucus production in respiratory cell culture on an air-liquid interface (ALI) with basal media access by the epithelial layer [24]. By growing cells on a microporous membrane with media in a basal reservoir beneath the cells and an exposed lumen, it was hypothesized that mucus secretion could be stimulated with the addition of VIP and media containing differentiation factors. Using this system, it was thought that the lack of convective mixing on the lumen would allow this mucus layer to grow

and be maintained for multiple days of culture [23, 24]. While this method does have some shortcomings, namely the lack of biomimetic microstructure (monolayer vs. crypts) and the lack of regular peristaltic fluid flow, it has been demonstrated previously that this ALI culture method allows for the creation of a measurable mucus layer after 2-3 days of culture [24]. While this mucus layer is useful for conducting assays, it is first necessary to understand whether the mucus produced by the ALI gut culture is biochemically and rheologically similar to that of native gut mucus. Significant differences in porosity, viscosity, composition, and structure could all cause major downstream effects on cell behavior, specifically in response to pathogen exposure [24]. This project was aimed to validate this ALI model system, analyzing the rheological and biochemical differences between ALI *in vitro* mucus and harvested native gut mucus.

2.2. Materials and methods

2.2.1. Air-liquid interface culture of intestinal epithelial cells

Cells derived from human transverse colon samples were cultured and expanded as described in previous publications [20, 25]. Cells were acquired from colonoscopies at the University of North Carolina's Hospital Meadowmont Endoscopy Center with informed consent of the patient (under the approved University of North Carolina Institutional Review Board #14-2013), and were collected from 3 separate donors (2 male, 1 female). All experiments in this study were conducted using cells between passage 5 and 10 (P5 and P10). Cells demonstrated a normal karyotype through P11 [25]. A solution of 1% Matrigel in cold 1X phosphate-buffered saline (PBS) was prepared. 1 mL each of this solution was placed in the top compartment of 12-well polyurethane Transwell inserts with 0.4 μm pores (#3460; Corning, Corning, NY). After insertion, these Transwells were incubated for 24 h at 37°C, then rinsed twice with sterile 1X PBS. Transverse cells were then plated in these Transwell inserts in Sato’s expansion media,

described in previous publications [20, 25, 26]. 1 mL of Sato's media containing cells was placed in the top compartment of each Transwell, and 2 mL of Sato's media with no cells was placed in the bottom compartment underneath each Transwell. Media was changed at 3 days. At 5 days, a solution of differentiation media (DM, described previously [20, 25]) with 330 ng/mL vasointestinal peptide (VIP; #AS-22872; AnaSpec, Fremont, CA) was prepared. 0.5 mL of this media was added to the basal compartment beneath each Transwell every 24 h. This left the apical surface of the cells exposed as an air-liquid interface. Cells were cultured for 2-7 days in these conditions, with samples collected from each day and stored separately. For mucus collection, a positive pressure pipette was used to collect and store the viscous mucus samples.

2.2.2. Mucus harvest from ex vivo surgical resections of intestinal tissue

Ex vivo surgical resections from human GI tract biopsies were received in Roswell Park Memorial Institute (RPMI) 1640 growth medium from the Shehzad Sheikh lab. These samples were acquired from colonoscopies at the University of North Carolina's Hospital with informed consent of the patient (under the approved University of North Carolina Institutional Review Board #10-0355). These samples were transported and harvested for mucus within 2 hours of reception. All samples were initially massed and their patient code recorded, and placed within a p100 petri dish. Initially, a spatula was used to scrape off the visible mucosa layer from the epithelial side of the samples, and this scraping was collected in a 15 mL tube. The samples were then incubated for 10 min in the petri dish on a rotary platform at 37°C with 1 mL of 1X PBS per g of sample. This wash was collected and stored in a separate 15 mL tube. The tissue was then incubated in the same conditions (10 min at 37°C with rotation) with 1 mL/g of sample of 1X PBS with 10 mM DTT, and the wash was collected. Finally, 1 mL/g of sample of 6 M guanidinium hydrochloric acid (GuHCL) was incubated with the sample under the same

conditions, and the wash was collected. These samples were then frozen at -20°C until needed for analysis.

2.2.3. Macrorheology for mucus analysis

Bulk rheological properties of the mucus samples were measured using cone-and-plate oscillational rheometry (20 mm cone, 1° deflection). 40 µL of each sample were loaded onto the bottom Peltier plate of a DHR-3 rheometer (TA Instruments, New Castle, DE). Next, two separate steps of oscillatory shear testing were conducted. First, the linear viscoelastic region (LVR) for the storage modulus (G') and the loss modulus (G") was determined by applying a range of small strains to each sample (0.01-10%) at two frequencies (1 Hz and 5 Hz). Next, a frequency sweep of a constant strain magnitude (1%) were applied to the same sample from 0.1 Hz to 100 Hz, generating a frequency vs. modulus plot for G', G", and the complex viscosity (η*). Mechanical sweeps were conducted with three separate loads from each sample to account for variance.

2.2.4. Microrheology for mucus analysis via microparticle tracking

For rheological properties on the microscale, 30 µL of each mucus sample was aliquoted into a separate conical tube. After this, each sample was loaded with 0.5 µL of 1-µm diameter fluorescent carboxylated beads (F8823; Thermo Fisher, Fremont, CA) and left for 24 h at 4°C on a rotating platform to allow beads to mix into the samples. After this, 5 µL of each sample was placed on a glass slide underneath a glass cover slip. Using a Nikon Eclipse TE2000U microscope with a 40x air objective, the motion of the beads was recorded at 60 FPS for 30 s. The movement of each bead was automatically tracked using a custom Python program, TrackPy (https://doi-org.libproxy.lib.unc.edu/10.5281/zenodo.34028). The mean squared displacement

(MSD) and complex viscosity (η*) values were calculated for each bead in accordance with mathematics described previously, primarily based on the Stokes-Einstein equation [27, 28].

2.2.5. Biochemical mucus analysis

10 µL of the mucus samples were mixed as a 20% solution in 6M GuHCL at 25°C for 20 min, in order to break down non-covalent bonds and leave behind large mucin protein complexes. These samples were then diluted further at a ratio of 1:10 or 1:40 in light scattering buffer (pH = 7.0). This solution was then run through a high pressure liquid chromatography (HPLC) CL2B column, allowing for weight-based separation of mucins from smaller proteins. HPLC and light scattering were performed using the Optilab t-REX refractometer (Wyatt Technology, Santa Barbara, CA) and Dawn Heleos II multi-angle laser photometer (Wyatt Technology, Santa Barbara, CA).

2.2.6. Immunohistochemical staining and imaging

Mucus samples (both scrapings and apical washings) were pipetted onto positively charged microscope slides and allowed to dry at 25°C for 1 h. The samples were then fixed with 10% neutral buffered formalin (NBF) for 5 min. They were washed with 1X PBS 3 times for 5 min each in a stationary phase and then blocked with 3% bovine serum albumin (BSA) in 1X PBS for 1 h at 25°C. After blocking, the 3% BSA solution was replaced with a primary antibody/lectin solution of either MUC2 BD (Mouse Anti-Human MUC2) and biotinylated jacalin, or 45M1 (MUC5AC monoclonal antibody) and biotinylated wheat germ agglutin (WGA). All primary antibodies and lectins were diluted 1:1000 in 3% BSA solution. After incubating 16 h at 4°C, protected from light and kept moist using wet paper towels in a slide box, the samples were washed 3 times with 1X PBS for 5 min each and incubated in secondary antibody solution at 25°C for 1 h. The secondary antibody solution was composed of Alexa

Fluor 594 donkey anti-mouse IgG (mouse red) and streptavidin Alexa Fluor 488 conjugate (streptavidin green), diluted 1:1000 in 3% BSA solution and used as secondary antibodies. After 1 hour, the secondary antibody solution was replaced with 4′,6-diamidino-2-phenylindole (DAPI) diluted 1:1000 in 1X PBS for 5 min at 25°C. The samples were then washed with 1X PBS 3 times for 5 min each, aspirated, and the slides were mounted using FluorSave mounting oil and 24X50-1.5 coverslips and sealed with clear nail polish. The samples were imaged using the Olympus VS120 virtual microscope (slide scanner) and the Olympus FluoView FV1000 (confocal) microscope. For quantification, MATLAB R2019b (Mathworks, Natick, MA) was used to outline individual mucus complexes using pixel thresholding and calculate their size.

2.2.7. Weight percent solids measurements

50-100 µL of mucus was aliquoted on a pre-weighted foil square and the combined mass of the mucus sample and foil square was measured. The sample and foil were incubated for 16 h at 80°C. The final mass of the sample and foil were measured, allowing for calculation of the percent solids remaining after liquid evaporation.

2.2.8. Transepithelial electrical resistance measurements

Using the cell culture technique described in Section 2.2.1, 3 Transwell inserts were cultured to confluence and then cultured under the ALI for 5 days of mucus accumulation. The apical and basal reservoirs of these inserts were washed 2 times with 1X PBS. Additionally, a Transwell insert without any cells was washed 2 times with 1X PBS. Following this, the transepithelial electrical resistance (TEER) of each insert was measured using a Millicell ERS-2 Voltohmmeter (Millipore, Burlington, MA). This measurement was conducted 3 times per well, with the probe placed at different locations within each well for each measurement.

2.2.9. pH measurement of apical and basal reservoirs of Transwell inserts

Using the cell culture technique described in Section 2.2.1, 9 Transwell inserts were cultured to confluence and then cultured under the ALI for 5 days of mucus accumulation. Following this, a Mettler Toledo S220 SevenCompact Benchtop pH/ISE Meter (Mettler-Toledo, LLC; Columbus, OH) was calibrated between pH 7 and pH 10. These Transwells were then tested for pH at 25°C in the basal reservoir, then in the apical reservoir, within a period of 3 min. To control for temperature-dependent changes in pH, the pH of the basal reservoir was tested again directly after testing of the apical reservoir.

2.2.10. Statistics

In order to determine statistical significance, two-tailed, two-mean t tests were conducted using the mean and standard deviation of each variable of interest and comparing between *in vitro* and *ex vivo* sample data. Statistical significance was defined using 95% confidence intervals, with p-values < 0.05. For power law analysis, power law equations were fit to gathered data using OriginPro 2020 (OriginLab, Northampton, MA).

2.3. Results and discussion

2.3.1. Overview of mucus generation and collection

The goal of this project was to establish the effectiveness of ALI culture in generating *in vitro* colonic mucus, and comparing the properties (rheological and biochemical) of that mucus to native colonic mucus. Using the techniques described in Section 2.2.1, a mucus layer was created and collected using an *in vitro* colonic epithelial monolayer (Fig 1). Cells were initially seeded and grown to confluence on a 12-well Transwell insert coated with a thin layer of Matrigel, using Sato's expansion media. After reaching confluence, basal media was replaced with differentiation media containing VIP and apical media was removed entirely, creating an

air-liquid interface (ALI) for the cell monolayer. During the 2-7 days of culture, mucus was secreted and accumulated on the apical surface of the monolayer where it could be collected and analyzed.

2.3.2. Establishing the effectiveness of an ALI interface for culture confluence and metabolite secretion

The initial steps of this project were to establish that a continuous monolayer of colonic cells could be formed, and that this monolayer could create a measurable level of mucus over time. It was hypothesized that a continuous monolayer would have a notably higher transepithelial electrical resistance (TEER) than a normal Transwell insert would. For example, in the CaCo-2 human colon cell line, TEER values between 150-400 $\Omega.cm^2$ have been reported [30]. For this *in vitro* system, 3 wells cultured for 10 total days (5 days of expansion, 5 days of mucus secretion) were prepared for TEER measurements as described in Section 2.2.8. A blank Transwell, containing no cells, was also prepared as a control. After this, the TEER of each of these wells was measured and compared to establish if the ALI system generated a contiguous monolayer (Fig 2a). It was found that each of the cell-containing wells offered a statistically significantly higher resistance than the blank well, as the blank well had a TEER of 144 $\Omega.cm^2$ and the cell-containing wells showed resistances of 364-422 $\Omega.cm^2$. This provided evidence that this *in vitro* system was capable of generating a contiguous monolayer of colonic epithelial cells.

The second hypothesis for the proof-of-concept experiments in this project was that, if a monolayer were given more days of culture in the ALI, then it would accumulate a measurably higher amount of mucus (and likely other metabolites and proteins). This would translate to a higher percentage of solids in the fluid collected from the apical reservoir of the Transwell in these cultures, as measured in Section 2.2.7. Cells were grown to confluence on Transwell

inserts, and then allowed to accumulate mucus under the ALI-VIP culture for a period of 2-7 days. On each of these days, mucus from wells were harvested, and the % solids in the apical collection was measured (Fig 2b). Donors of both genders and ranging from age 12 to 65 were used. When harvested, as much mucus as possible was collected from the well and then the culture was discarded; no well was harvested on multiple days. It was found that the weight percent of solids increased directly as the number of days of accumulation was increased, demonstrating higher % solids at 7 days of accumulation (2.4±0.3%) than at 2 days of collection (1.3±0.5%). This increased % solids in the collection was statistically significant with 95% confidence ($p = 0.029$). This gives evidence to confirm the initial hypothesis, and suggests that more time in the ALI allows the epithelial monolayer to secrete more mucus without previously-secreted mucus being washed away or destroyed.

One interesting (and unexpected) phenomenon was first noticed due to pH-based color differences in the apical and basal reservoir media, observed after 4-5 days in the ALI. It was expected that media would either leak or be pumped through the cell monolayer into the apical reservoir in addition to mucus (and other) secretions, but a significant pH difference was unexpected. After 5 days of mucus accumulation in the ALI, the pH of the apical and basal reservoirs was measured in 9 Transwells (Fig 2c). The apical reservoir was found to have a statistically significantly higher pH compared to the basal reservoir, indicating that the cell monolayer was releasing basic compounds. One potential explanation of this phenomenon could be for an initial layer of protection for the mucosal layer against gastric acid, as has been observed in the literature [30]. This would give further evidence that the cells formed a contiguous monolayer, as well as evidence for the secretion of a coherent mucus layer above the

cell monolayer. Future studies could be conducted to determine the nature of which ion channels were being activated by exposure to the ALI.

2.3.3. Using oscillational rheometry to measure rheological properties of intestinal mucus on the macroscale

Using the methods described in Section 2.2.3, bulk rheometry was performed on stored mucus from both *in vitro* and *ex vivo* samples. It was hypothesized that higher weight percent of solids would positively correlate with viscoelastic properties in the mucus samples, as more solid material in the sample would likely lead to stronger gelation. It was also hypothesized that *ex vivo* samples would display stronger viscoelastic properties than *in vitro* samples, due to a larger amount of cell debris within the *ex vivo* samples as well as a stronger mucus response in those samples after their exposure to intestinal bacteria. First, an amplitude sweep of increasing strain rates was conducted at a constant frequency of 1 Hz, as 1 Hz is representative of native *in vivo* intestinal contraction rates [20]. To determine the storage modulus (G') and the loss modulus (G"), the linear viscoelastic region (LVR) was found for each sample. This region represents the range of applied stress where a viscoelastic material (like a hydrogel) displays rheological properties that are independent of the applied stress, allowing for comparison between samples [31]. For this set of experiments, G' and G" measurements were made at 1% stress were chosen for each sample, as this stress value fell within the LVR for both *in vitro* and *ex vivo* samples. These values were then compared based on the weight percent of solids previously found for each mucus sample (Fig 3a,b).

The first observation made about the LVR modulus data was that, for all samples, G' was greater than G". This is important to note, as G' > G" is an indicator that the material being analyzed has undergone gelation, since G' represents the elastic properties of the material while

G” represents the fluid-like properties of the material [20]. To show this relationship, the ratio of G’/G” for each data point was also plotted, indicating gelation within the samples (Fig 3c). One interesting observation is the independent relationship between weight percent of solids and the G’/G” for the *in vitro* samples. This indicates that gelation of these samples is relatively homogenous regardless of mucin concentration in the sample. Another important observation was that *ex vivo* mucus displayed larger G’ and smaller G” values than *in vitro* samples at similar weight percentage of solids. This data is evidence that there is a stronger gel matrix in the *ex vivo* samples, though it could also be explained by the presence of cells and other debris trapped in those samples compared to the apical washings from the *in vitro* mucus samples. Finally, it was observed that the *in vitro* mucus samples displayed a concentration-dependent power law, scaling upwards as the weight percent of solids in the sample was increased, with R^2 values of 0.90 and 0.87 for the *in vitro* G’ and G” trends, respectively. This was expected based on examples in the literature of power law scaling below a threshold concentration of mucins/solids [28, 32, 33]. The *ex vivo* samples also displayed a concentration-dependent increase in both G’ and G”, but did not display as strong of a power-law correlation, with R^2 values of 0.46 and 0.60, respectively. This could have a few explanations, potentially including the smaller number of samples compared to the *in vitro* samples, more heterogeneity in the structure of the *ex vivo* samples, and a smaller range of weight-percent solids in these samples (1.4-2% for *ex vivo*; 0.8-3.3% for *in vitro*).

The viscoelastic moduli of a hydrogel can be expressed as one frequency-dependent variable, the complex viscosity η*, via the equation [34]

$$\eta^*(\omega) = \frac{(G'^2 + G''^2)^{1/2}}{\omega}$$

Typically, a frequency sweep is used to find η* at a representative frequency for comparison between samples. For this set of experiments, 1 Hz was again chosen for its physiological relevance to intestinal contraction [20], and the complex viscosities of both *in vitro* and *ex vivo* samples were plotted against their weight percentage of solids (Fig 3d). Very similar trends were found when using η* as were found by comparing G' and G" for both types of samples. The *in vitro* samples displayed a very strong concentration-dependent power-law correlation ($R^2 = 0.94$) while the *ex vivo* samples displayed a much more modest correlation ($R^2 = 0.53$), and the *ex vivo* samples displayed stronger mechanical properties than *in vitro* samples of comparative weight percentage of solids.

2.3.4. Microbead tracking to measure rheological properties of intestinal mucus on the microscale

While macrorheology provides measurements on the bulk mechanical properties of a hydrogel, it is ill-suited to provide accurate information on the heterogeneity of a sample. Mucus, as a natural polymeric network filled with and cellular and fecal debris, will inherently exhibit irregular structure. It is important to identify the levels of heterogeneity in both *in vitro* and native mucus, as a loosely-packed, mostly homogeneous mucus layer will behave differently in epithelial protection and bacterial diffusion than a heterogeneous, clumpy mucus layer will. Additionally, analyzing rheological properties on the microscale can minimize the effects of cells and other large debris on the resulting measurements. Microrheology can be accomplished by measuring the movement of small objects through a hydrogel or fluid. In this project, 1-μm diameter carboxylated beads (as described in Section 2.2.4) were used. Specifically, thermal motion of small objects can be converted into rheological measurements by means of the Stokes-Einstein law of diffusion [38]. Briefly, by assuming that small particles behave similarly to

gaseous molecules in solution, the mean square displacement (MSD) of a particle in solution can be converted into the diffusion coefficient (D_T) of the particle in that solution via the equation [36]

$$MSD(t) = 4D_T t$$

This follows that, if a particle's MSD is tracked and measured over a known period of time (in this set of experiments, 30 s), the D_T of the sample can then be calculated from that bead. Moving further, the Stokes-Einstein law allows that the viscosity η* of a sample can be calculated from D_T based on the equation [36]

$$D_T = \frac{k_b T}{3\pi\eta^* d}$$

Where k_b is the Boltzmann constant, T is temperature, and d is the diameter of the particle being used. It should be noted that η* in this equation is frequency dependent when measured in viscoelastic fluids, and can derived by applying a Fourier transform to the measured shear modulus [37]. By tracking the MSD of many particles in the same sample, an average η* can be found for that sample; additionally, by comparing the MSD of each individual particle within a sample, the range of values can be expressed and the heterogeneity of the sample can be assessed.

For these experiments, fluorescent beads were mixed and tracked for MSD in both *in vitro* and *ex vivo* mucus samples as described in Section 2.2.4 (Fig 4). First, it was expected that beads would move more freely within samples that had lower weight percentage of solids, as there would be less protein matrixes to block random motion of the particles. To demonstrate this, beads were placed in *in vitro* mucus samples of ~1% solids and ~3% solids and representative maps of the particle motion were generated (Fig 4a). It can be observed that the representative bead in the 1% solid sample had more random Brownian motion than the bead

from the 3% sample, giving evidence in support of the initial hypothesis as a proof of concept. Moving from this into comparison between *in vitro* and *ex vivo* samples, multiple samples for each type within the 1.4-2.0% solids range were loaded with beads and tracked for MSD (Fig 4b-d). Firstly, the average viscosity for each sample indicated that the *ex vivo* samples had a higher microviscosity than the *in vitro* samples, and that both examples were significantly more viscous than water (which displays a complex viscosity of ~10^{-3}). Narrowing down the range to physiological relevance it was found that, at 1 Hz (or 2π rad/s), the complex viscosity of the *ex vivo* samples was .42±.59 Pa*s and the viscosity of the *in vitro* samples at that frequency was .02±.20 Pa*s. While not statistically significant ($p = 0.169$), this trend would indicate that the *ex vivo* samples have a stiffer underlying matrix than their *in vitro* counterpoints, which would give evidence that the mucus being synthesized with the ALI culture is not entirely reflective of native mucus. It should also be noted that the high variance in MSD in the *ex vivo* samples hold with the hypothesis that these native mucus samples form more heterogeneous complexes.

By looking at the distribution of the measured MSDs within each type of sample, an explanation for these rheological trends can be found. Both samples exhibited two distinct MSD peaks when looking at a histogram distribution of the MSD of individual tracked beads (Fig 4c). The first peak occurs at approximately 10^{-3} Pa*s, indicating the presence of water or mucus networkss with large pore size within the sample. The high amplitude and narrowness of these peaks is in keeping with the low percentage of solids within the samples, with the *in vitro* samples displaying a higher overall percentage of beads in water (even with a smaller number of total beads) of 55% compared to 29% of beads in water in the *ex vivo* samples. The second peaks, found in the 10^{-1}-10^{-2} Pa*s range, are likely indicative of beads within mucus in the sample. Looking at just these peaks, the *ex vivo* samples displayed an average viscosity of

.28±.61 Pa*s, while the *in vitro* samples had an average viscosity of .34±.16 at 1 Hz. These values, which are not statistically significantly different in either direction ($p = 0.85$), indicate that the mucus components of the samples likely display similar microrheological properties. Delving further into this, the complex viscosity of the beads within these mucus peaks was tracked over a range of angular frequencies (Fig 4d). These observed trends indicate much more similar microrheology between the sample types, giving evidence that the *ex vivo* samples display more heterogeneous mucus complexes, whereas the *in vivo* samples indicate a more diffuse mucus layer with a lower degree of heterogeneity. These observations show that, while the mucus may form different types of complexes between *ex vivo* and *in vitro* samples, they display similar rheological properties on the microscale and that the *in vitro* mucus does have some physiological relevance.

2.3.5. Measuring biochemical properties of gut mucus via light scattering

One important aspect of this study was determining whether or not the ALI-generated *in vitro* mucus formed complexes with similar mucin concentrations and structure to *ex vivo* samples, as different mucus complexes and mucin types would lead to different sample responses downstream during biotechnology applications (such as drug screening). These properties could be found by using multi-angle laser light scattering (MALLS), as described in Section 2.2.5, with the mucus samples forced into solution using GuHCL. GuHCL was used to break all non-covalent bonds in the sample, allowing for analysis of primarily proteins and excluding other non-covalent debris. By detecting the scattering angle and intensity of a laser-illuminated mucus sample, biochemical properties such as molecular weight, total sample mass, and radius of gyration can be determined [38]. In order to allow for comparison, both *ex vivo* and

in vitro samples within the 1.4-2.0% range of weight percentage of solids were analyzed, and their average molar mass, total mass of mucins, and radius of gyration was found (Fig 5).

The largest difference between the *ex vivo* and *in vitro* samples was found with the average molar mass of the analyzed mucus complexes. *Ex vivo* samples exhibited a statistically significantly higher ($p <<< 0.001$) molar mass of 2.6e3±8.1e2 MDa compared to the *in vitro* molar mass of 6.9e2±4.6e2 MDa. This ~4-fold increase in molar mass would indicate much larger mucin complexes from native tissue, while the smaller molar mass for *in vitro* samples indicates a much looser, more diffuse layer of mucus. This result is supported by the average radii of gyration found for the two samples, as the *ex vivo* samples displayed a statistically larger radius of gyration compared to the *in vitro* samples ($p = 0.018$). This result could potentially be caused by the presence of additional debris in the *ex vivo* samples (like cells), allowing for mucus nucleation rather than primarily mucus complex bonding. This theory would be supported by the statistically larger final mass of covalently-bonded complexes in the *ex vivo* samples compared to *in vivo* ($p = 0.013$), though that could also indicate an overall larger production level of mucus with native tissue compared to the *in vitro* monolayer. It could also be explained as the synthesis of the two distinctly different mucus layers, inner and outer, described in Section 2.1.3, with *ex vivo* samples containing primarily the more compact inner layer, and the *in vitro* samples creating the more diffuse outer layer [18]. This result could also be explained by the presence of covalent bonds; while 8 M GuHCL should theoretically break any non-covalent bonds and drive those components into solution, it is possible that some additional bonds were not broken within the *ex vivo* complexes. This theory could be tested in the future using a stronger dilution liquid, or by running a molecular weight SDS gel electrophoresis gradient to give a clearer look at the heterogeneity of molar mass within the samples.

2.3.6. Staining and imaging in vitro and ex vivo samples for proteins of interest

After rheological and biochemical properties were tested in both samples, it was necessary to stain, image, and quantify the differences in mucus complexes via confocal microscopy. This step allowed for comparisons between experimental data and the mucus phenotype for each sample. Using DAPI as a DNA stain (blue) and anti-MUC2 human antibody (red), confocal images of both *in vitro* and *ex vivo* mucus were generated (Fig 6). A few initial observations can be made on these images. First, there is a smaller presence of DNA in the *in vitro* samples compared to the *ex vivo* samples, indicating that there are less cells (and thus, less nuclear DNA) being collected from the *in vitro* apical washings. The larger presence of DNA in the *ex vivo* scrapings occurs in larger groupings that are co-localized with mucus, indicating that cells are clumping together and that mucus complexes are being formed around these cells. This was expected, as the mucus collection method for the *ex vivo* samples is more likely to disturb the epithelial cell layer than the gentler collection method for *in vitro* mucus. The mucus staining provides evidence in support of the biochemical results found in Section 2.3.5, showing that *ex vivo* mucus tends to form larger complexes compared to the looser *in vitro* mucus structure. In combination with DNA staining, these larger complexes could be caused directly by the higher presence of cells in the *ex vivo* samples.

Once stained, it was necessary to quantify the differences in mucus complex size and coverage between the two sample types. Using MATLAB, the outline of each individual mucus complex (regardless of size) in each image was found (Fig 7a-b). These images were then used to calculate the average size of a mucus complex (Fig 7c) and the overall surface coverage of mucus (Fig 7d) for each sample type. While neither measurement yielded statistically significant results (likely due to sample size concerns), the overall trends measured were consistent with

other data found in this study. *Ex vivo* samples displayed a higher average complex size and higher overall surface coverage that *in vitro* samples. This indicates that the *ex vivo* samples form larger gel matrixes and that more mucus is present in the *ex vivo* samples. Also, the high variability in average complex size in the *ex vivo* samples is consistent with the hypothesis that mucus in those samples is more heterogeneous than the diffuse mucus layer in *in vitro* samples. Overall, these results provide evidence that the mucus formed from ALI *in vitro* culture is of similar composition but different structure than harvested native mucus.

2.4. Conclusions and acknowledgments

In summary, data reported in this study demonstrated that an air-liquid interface culture of colonic epithelial cells is capable of generating a continuous mucus layer that coats the epithelial layer. These conditions provided a contiguous monolayer of cells, measurable based on the transepithelial electrical resistance across the cell layer. Reasonable evidence was also found that these monolayers experienced some form of ion pumping based on pH differences between the apical and basal reservoirs of the porous insert used to culture the monolayers. After exposure to the ALI, the mucus layer was collected and measured for the weight percentage of solids within the sample; a positive correlation between days of mucus accumulation and % solids within the sample was found. This correlation indicates that additional mucus was generated with extra days of culture under the ALI.

The mucus from these *in vitro* tissue cultures was collected at 24 hour intervals for 2-7 days of exposure to the ALI. In addition, *ex vivo* mucus was directly collected from the mucosa of native transverse colon tissue. These samples were tested via oscillational rheometry and bead-tracking microrheology to determine their biomechanical properties on both the macro- and microscale. On the macroscale, *ex vivo* mucus displayed slightly stronger mechanical properties

than *in vitro* mucus, with trends of larger storage moduli and complex viscosity to go with a trend of lower loss moduli. Additionally, *in vitro* mucus displayed a measurable power law correlation between the percentage of solids in the sample and their measured rheological properties. On the microscale, however, there was not a significant difference in rheological properties between the *ex vivo* and *in vitro* samples when measurements were isolated to beads embedded within the mucus complexes of the sample. It was noted that the *ex vivo* samples displayed a larger amount of heterogeneity in rheological properties, indicating that there was more mucus clumping in these samples compared to the looser mucus network found in *in vitro* samples. When the biochemical properties of these samples were measured and compared, this hypothesis was supported as *ex vivo* samples displayed a higher overall molar mass and radius of gyration in their mucus complexes. Staining results provided more evidence in support of this hypothesis, showing larger overall mucus concentration and complex size in *ex vivo* samples compared to *in vitro* samples.

The author would like to thank Yuli Wang for assistance and training in ALI culture and mucus collection, and thank Scott Magness for providing human colonic epithelial tissue. The author would also thank Matthew Schaner for assistance in native tissue collection. The author also thanks Matthew Markovetz, Lawrence Bacudio, and William Kissner for assistance in rheological measurements. Finally, the author thanks NSF GRFP Grant # 2016212411 and NIH DK109559 for funding.

2.5. Figures

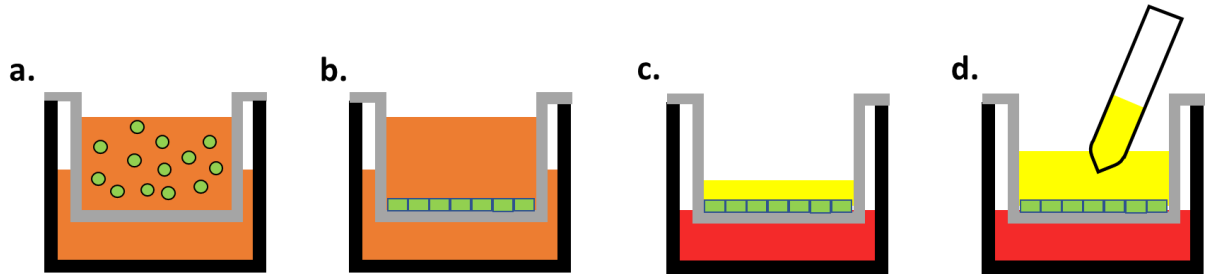

Figure 2.1. Schematic of ALI culture of colonic cells and mucus collection. A schematic of the air-liquid interface culture of colonic cells (green) for mucus formation. a) Cells are seeded on a microporous insert, with expansion media (orange) in both the apical and basal reservoirs. b) Cells are grown into a confluent monolayer over the course of 3-5 days. Expansion media is aspirated and replaced in both reservoirs every 2-3 days until confluence is reached. c) After confluence is achieved, both the apical and basal media are aspirated. Differentiation media (red) containing vasointestinal peptide (VIP) is placed in the basal reservoir underneath the microporous insert. No media is added to the apical reservoir (ALI culture). This allows for the formation of a hydrated continuous mucus layer (yellow) on the surface of the epithelial cell layer. Differentiation media is replaced daily. d) After 2-7 days of culture under ALI conditions, the mucus layer can be collected via a positive displacement pipette.

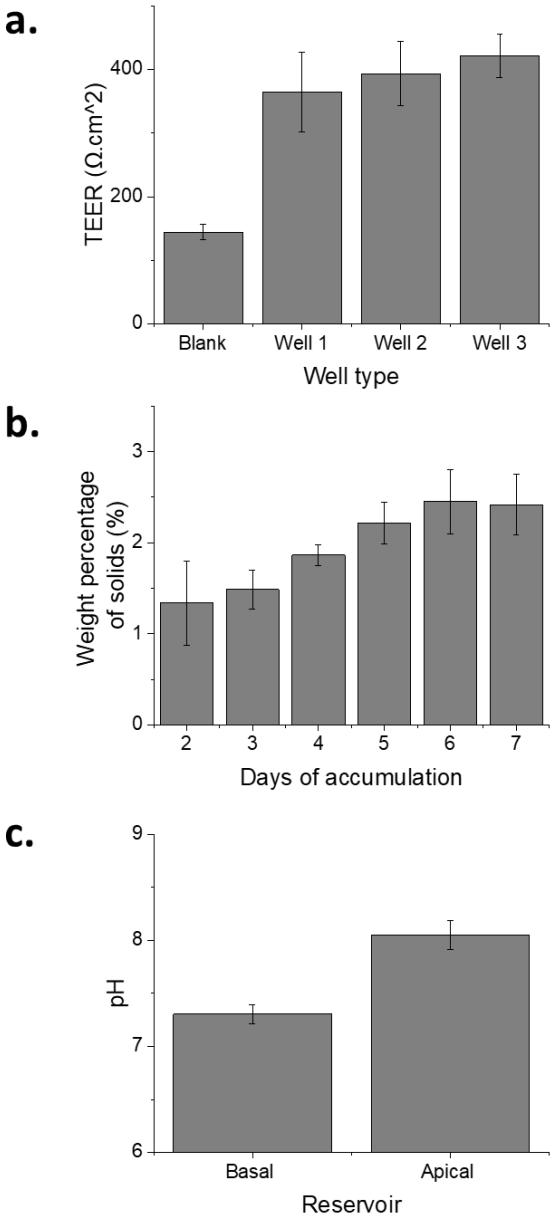

Figure 2.2. Establishing the effectiveness of ALI colonic culture and mucus accumulation over time. a) Transepithelial electrical resistance (TEER) was measured across 3 confluent layers of colonic epithelial cells, cultured on microporous inserts. Additionally, a microporous insert with no cells (submerged in PBS) was measured as a control. b) Confluent colonic epithelial cell layers were cultured under ALI-VIP conditions on microporous inserts for 2-7 days, allowing for the accumulation of a connected mucus layer. The mucus was collected from

3 inserts for each day between 2-7 days, and the harvested inserts were discarded after mucus collection. After this, 50 µL of each sample was measured for weight percentage of solids as described in Section 2.2.7. c) The pH of the apical and basal reservoirs of 9 wells were measured for monolayers that had been grown to confluence and then cultured under ALI-VIP conditions for 5 days, allowing for the formation of a mucus layer and for the pumping of media/ions across the cell monolayer.

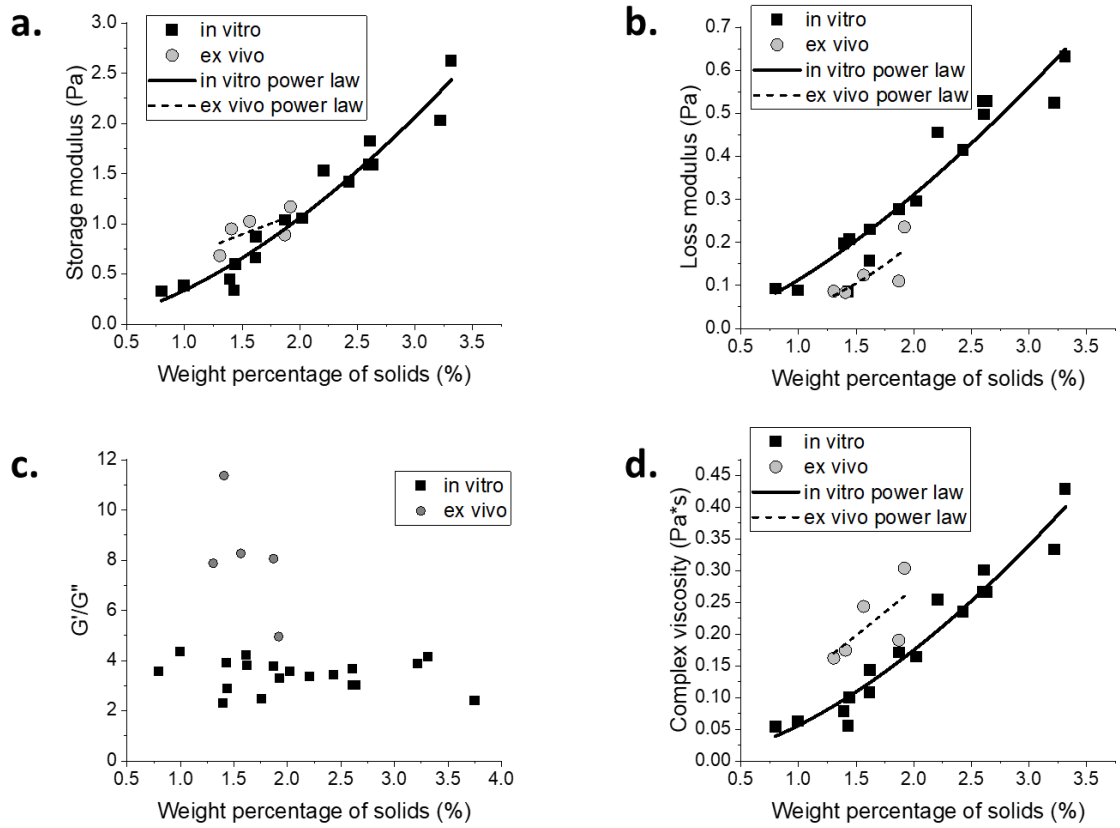

Figure 2.3. Measuring bulk rheology of mucus samples via oscillational rheometry. *In vitro* mucus samples grown from 3 separate transverse colon donors were collected from 2-7 days for each sample. Similarly, *ex vivo* mucus samples were collected from 5 separate samples of surgical resection tissue from non-inflamed transverse colons. These samples were measured in 40 µL aliquots using oscillational rheometry, generating scatter plots with the connection between weight percentage of solids and storage modulus (a) and loss modulus (b). To show gelation, which is indicated when G' > G", G'/G" was also plotted for each sample (c). Then the complex viscosity at 1 Hz was calculated and plotted for each sample vs. their weight percentage of solids (d). Power laws are plotted for both *in vitro* and *ex vivo* data for (a), (b), and (d).

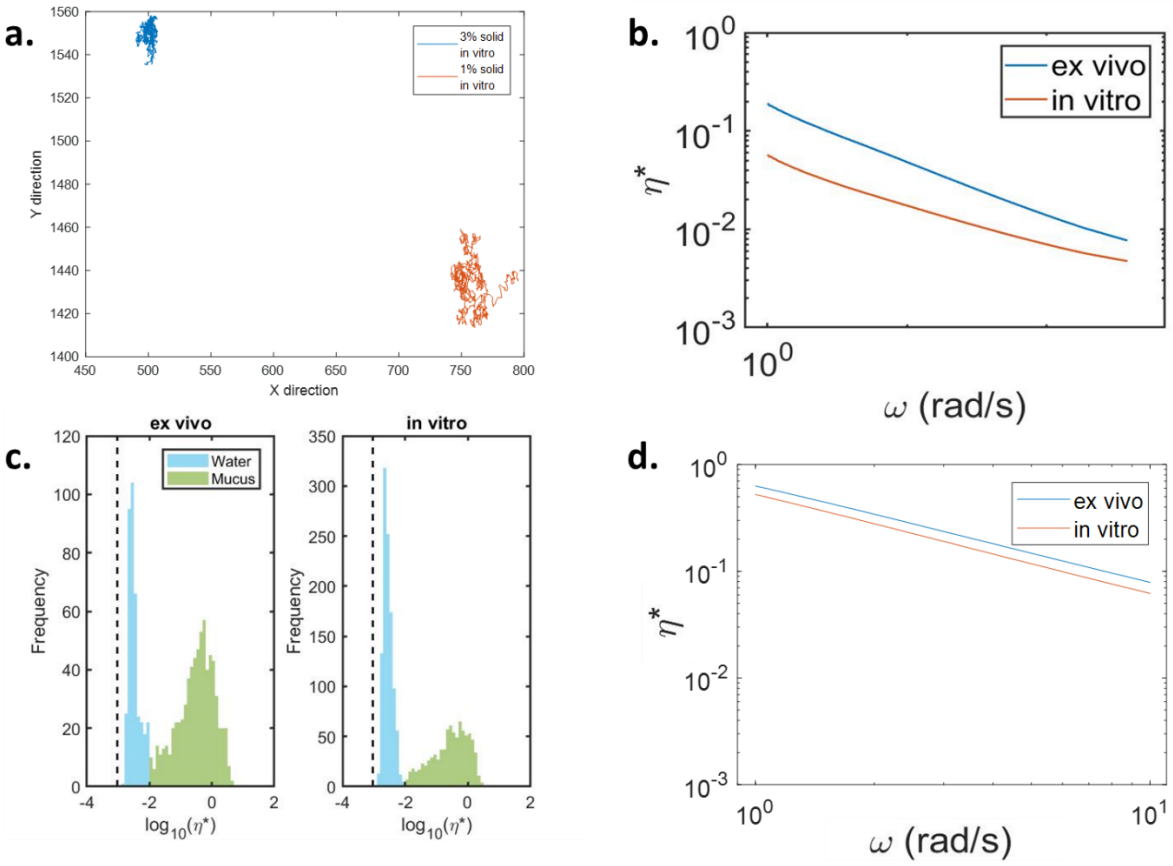

Figure 2.4. Measuring microrheology of mucus samples via microbead tracking. Collected mucus samples from both *in vitro* and *ex vivo* donors were tested for weight percentage of solids, and samples within the range of 1.4-2.0% solids were separated into 40 µL aliquots. These aliquots were loaded with fluorescent beads, and the movement of these beads was tracked for 30 s, with 30 iterations per sample. a) Representative trajectories of individual beads from *in vitro* samples of 1% solids and 3% solids were tracked and plotted in the xy-plane. b) The average MSD of all beads in the *in vitro* and *ex vivo* samples was calculated and converted into a frequency-dependent range of complex viscosities. c) The log of the complex viscosity at 1 Hz of each individual bead in each set of samples was calculated, and these values were plotted based on their frequency of occurrence. These histograms displayed two distinct peaks, one close to the viscosity of water, and the other presumably representing beads stuck in mucus complexes.

d) The frequency-dependent range of complex viscosities was calculated and plotted only for beads embedded in a mucus complex.

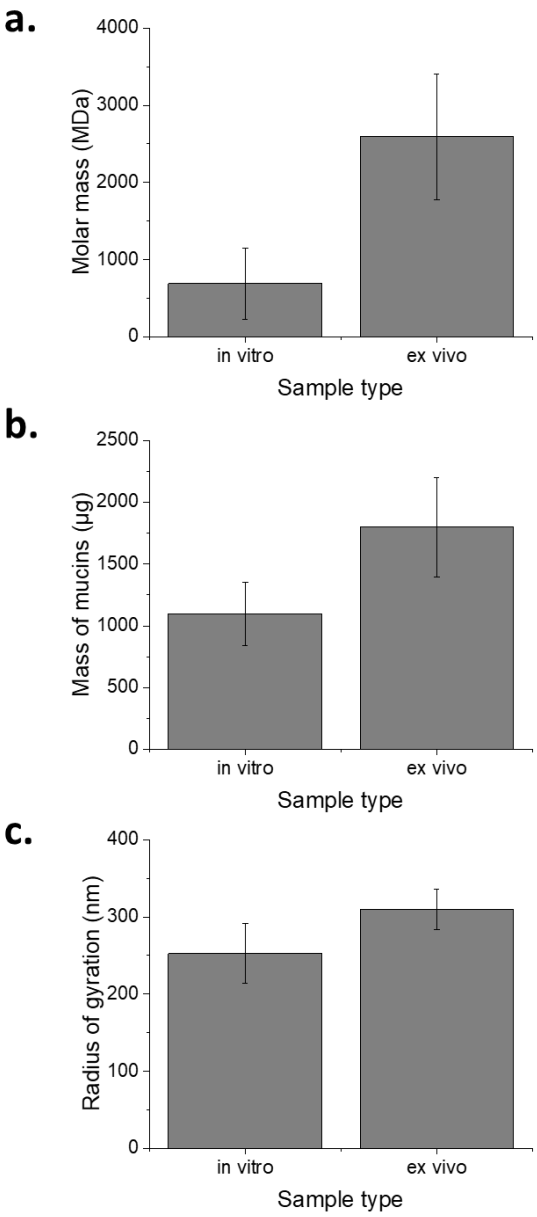

Figure 2.5. Measuring biochemical properties of mucus samples via HPLC and light scattering. Samples of *ex vivo* and *in vitro* mucus with 1.4-2.0% solids were diluted in guanidinium hydrochloric acid and light scattering buffer. These samples were then separated by high-pressure liquid chromatography and proteins were detected by multi-angle light scattering, generating average values of molar mass (a), total mass of mucins in the sample (b), and radius of gyration (c).

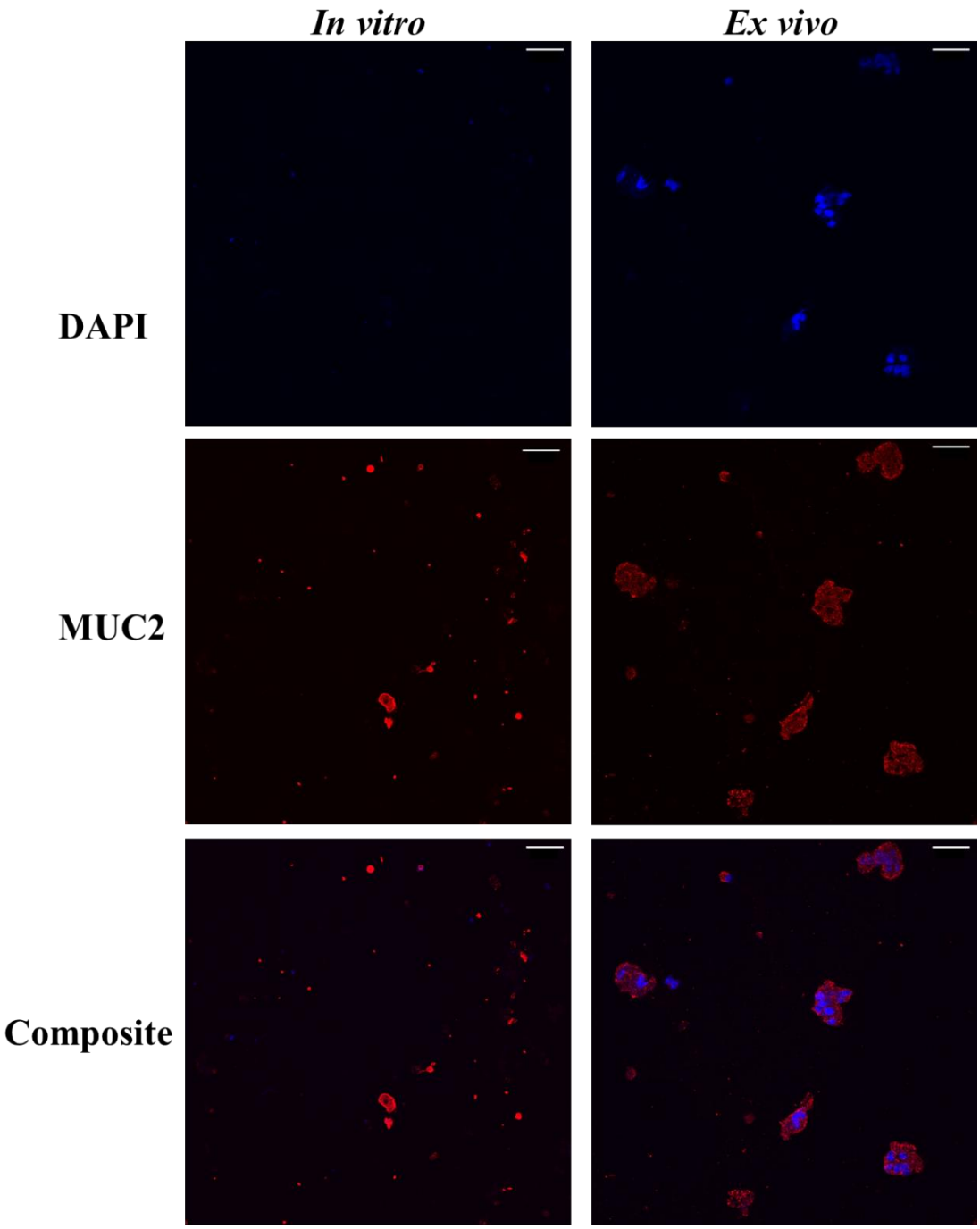

Figure 2.6. Staining for DNA and MUC2 in *in vitro* and *ex vivo* samples. Confocal microscopy images were taken of *in vitro* apical washings and *ex vivo* mucosal scrapings after staining with DAPI for DNA (blue) and MUC2 antibody for the MUC2 mucin (red). Scale bar in all images is 50 μm.

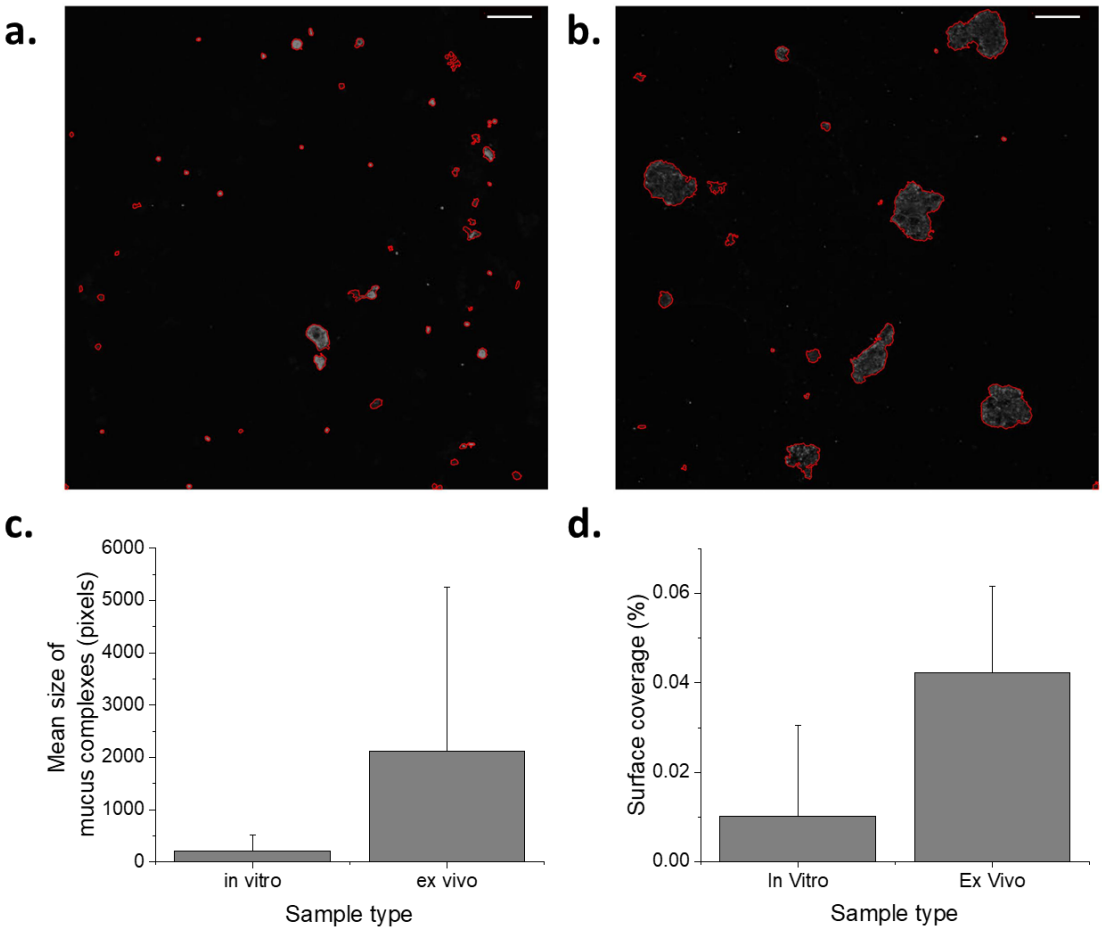

Figure 2.7. Quantifying the complex size and surface coverage of mucus samples based on source. Using stained images of mucus complexes from both *in vitro* and *ex vivo* samples, the outlines of individual mucus complexes were found and isolated from the image background. Representative images of this result are shown for both *in vitro* (a) and *ex vivo* (b) examples. The mean size of these complexes in pixels were calculated (c), and the average surface coverage of mucus over the entire image relative to the background size was also calculated (d). Scale bar for all images is 50 µm.

REFERENCES

1. Allison, P. R.; Johnstone, A. S. The Oesophagus Lined with Gastric Mucous Membrane. *Thorax* **1953**, *8* (2), 87–101.

2. Singh, P. K.; Parsek, M. R.; Greenberg, E. P.; Welsh, M. J. A Component of Innate Immunity Prevents Bacterial Biofilm Development. *Nature* **2002**, *417* (6888), 552–555. https://doi.org/10.1038/417552a.

3. Hodges, R. R.; Dartt, D. A. Conjunctival Goblet Cells. In *Encyclopedia of the Eye*; Dartt, D. A., Ed.; Academic Press: Oxford, 2010; pp 369–376. https://doi.org/10.1016/B978-0-12-374203-2.00053-1.

4. Meezaman, D.; Charles, P.; Daskal, E.; Polymeropoulos, M. H.; Martin, B. M.; Rose, M. C. Cloning and Analysis of CDNA Encoding a Major Airway Glycoprotein, Human Tracheobronchial Mucin (MUC5). *J. Biol. Chem.* **1994**, *269* (17), 12932–12939.

5. Johansson, M. E. V.; Phillipson, M.; Petersson, J.; Velcich, A.; Holm, L.; Hansson, G. C. The Inner of the Two Muc2 Mucin-Dependent Mucus Layers in Colon Is Devoid of Bacteria. *Proc Natl Acad Sci U S A* **2008**, *105* (39), 15064–15069. https://doi.org/10.1073/pnas.0803124105.

6. Johansson, M. E. V.; Sjövall, H.; Hansson, G. C. The Gastrointestinal Mucus System in Health and Disease. *Nat Rev Gastroenterol Hepatol* **2013**, *10* (6), 352–361. https://doi.org/10.1038/nrgastro.2013.35.

7. Hattrup, C. L.; Gendler, S. J. Structure and Function of the Cell Surface (Tethered) Mucins. *Annu. Rev. Physiol.* **2008**, *70*, 431–457. https://doi.org/10.1146/annurev.physiol.70.113006.100659.

8. Macao, B.; Johansson, D. G. A.; Hansson, G. C.; Härd, T. Autoproteolysis Coupled to Protein Folding in the SEA Domain of the Membrane-Bound MUC1 Mucin. *Nat. Struct. Mol. Biol.* **2006**, *13* (1), 71–76. https://doi.org/10.1038/nsmb1035.

9. Bustamante-Marin, X. M.; Ostrowski, L. E. Cilia and Mucociliary Clearance. *Cold Spring Harb Perspect Biol* **2017**, *9* (4). https://doi.org/10.1101/cshperspect.a028241.

10. Johansson, M. E. V. Fast Renewal of the Distal Colonic Mucus Layers by the Surface Goblet Cells as Measured by In Vivo Labeling of Mucin Glycoproteins. *PLoS One* **2012**, *7* (7). https://doi.org/10.1371/journal.pone.0041009.

11. Audie, J. P.; Janin, A.; Porchet, N.; Copin, M. C.; Gosselin, B.; Aubert, J. P. Expression of Human Mucin Genes in Respiratory, Digestive, and Reproductive Tracts Ascertained by in Situ Hybridization. *J. Histochem. Cytochem.* **1993**, *41* (10), 1479–1485. https://doi.org/10.1177/41.10.8245407.

12. Atuma, C.; Strugala, V.; Allen, A.; Holm, L. The Adherent Gastrointestinal Mucus Gel Layer: Thickness and Physical State in Vivo. *Am. J. Physiol. Gastrointest. Liver Physiol.* **2001**, *280* (5), G922-929. https://doi.org/10.1152/ajpgi.2001.280.5.G922.

13. Gum, J. R.; Hicks, J. W.; Toribara, N. W.; Siddiki, B.; Kim, Y. S. Molecular Cloning of Human Intestinal Mucin (MUC2) CDNA. Identification of the Amino Terminus and Overall Sequence Similarity to Prepro-von Willebrand Factor. *J. Biol. Chem.* **1994**, *269* (4), 2440–2446.

14. Thornton, D. J.; Khan, N.; Mehrotra, R.; Howard, M.; Veerman, E.; Packer, N. H.; Sheehan, J. K. Salivary Mucin MG1 Is Comprised Almost Entirely of Different Glycosylated Forms of the MUC5B Gene Product. *Glycobiology* **1999**, *9* (3), 293–302. https://doi.org/10.1093/glycob/9.3.293.

15. Ambort, D.; Johansson, M. E. V.; Gustafsson, J. K.; Nilsson, H. E.; Ermund, A.; Johansson, B. R.; Koeck, P. J. B.; Hebert, H.; Hansson, G. C. Calcium and PH-Dependent Packing and Release of the Gel-Forming MUC2 Mucin. *Proc Natl Acad Sci U S A* **2012**, *109* (15), 5645–5650. https://doi.org/10.1073/pnas.1120269109.

16. Schroeder, B. O. Fight Them or Feed Them: How the Intestinal Mucus Layer Manages the Gut Microbiota. *Gastroenterol Rep (Oxf)* **2019**, *7* (1), 3–12. https://doi.org/10.1093/gastro/goy052.

17. Johansson, M. E. V.; Larsson, J. M. H.; Hansson, G. C. The Two Mucus Layers of Colon Are Organized by the MUC2 Mucin, Whereas the Outer Layer Is a Legislator of Host–Microbial Interactions. *PNAS* **2011**, *108* (Supplement 1), 4659–4665. https://doi.org/10.1073/pnas.1006451107.

18. Clevers, H. The Intestinal Crypt, A Prototype Stem Cell Compartment. *Cell* **2013**, *154* (2), 274–284. https://doi.org/10.1016/j.cell.2013.07.004.

19. Sardelli, L.; Pacheco, D. P.; Ziccarelli, A.; Tunesi, M.; Caspani, O.; Fusari, A.; Vangosa, F. B.; Giordano, C.; Petrini, P. Towards Bioinspired in Vitro Models of Intestinal Mucus. *RSC Adv.* **2019**, *9* (28), 15887–15899. https://doi.org/10.1039/C9RA02368B.

20. Wang, Y.; Kim, R.; Gunasekara, D. B.; Reed, M. I.; DiSalvo, M.; Nguyen, D. L.; Bultman, S. J.; Sims, C. E.; Magness, S. T.; Allbritton, N. L. Formation of Human Colonic Crypt Array by Application of Chemical Gradients Across a Shaped Epithelial Monolayer. *Cellular and Molecular Gastroenterology and Hepatology* **2018**, *5* (2), 113–130. https://doi.org/10.1016/j.jcmgh.2017.10.007.

21. Webber, S. E.; Widdicombe, J. G. The Effect of Vasoactive Intestinal Peptide on Smooth Muscle Tone and Mucus Secretion from the Ferret Trachea. *Br J Pharmacol* **1987**, *91* (1), 139–148.

22. Kesimer, M.; Kirkham, S.; Pickles, R. J.; Henderson, A. G.; Alexis, N. E.; DeMaria, G.; Knight, D.; Thornton, D. J.; Sheehan, J. K. Tracheobronchial Air-Liquid Interface Cell Culture: A Model for Innate Mucosal Defense of the Upper Airways? *Am J Physiol Lung Cell Mol Physiol* **2009**, *296* (1), L92–L100. https://doi.org/10.1152/ajplung.90388.2008.

23. Wang, Y.; Kim, R.; Sims, C. E.; Allbritton, N. L. Building a Thick Mucus Hydrogel Layer to Improve the Physiological Relevance of In Vitro Primary Colonic Epithelial Models. *Cellular and Molecular Gastroenterology and Hepatology* **2019**, *8* (4), 653-655.e5. https://doi.org/10.1016/j.jcmgh.2019.07.009.

24. Hill, D. B.; Button, B. Establishment of Respiratory Air–Liquid Interface Cultures and Their Use in Studying Mucin Production, Secretion, and Function. In *Mucins: Methods and Protocols*; McGuckin, M. A., Thornton, D. J., Eds.; Methods in Molecular Biology; Humana Press: Totowa, NJ, 2012; pp 245–258. https://doi.org/10.1007/978-1-61779-513-8_15.

25. Wang, Y.; DiSalvo, M.; Gunasekara, D. B.; Dutton, J.; Proctor, A.; Lebhar, M. S.; Williamson, I. A.; Speer, J.; Howard, R. L.; Smiddy, N. M.; et al. Self-Renewing Monolayer of Primary Colonic or Rectal Epithelial Cells. *Cellular and Molecular Gastroenterology and Hepatology* **2017**, *4* (1), 165-182.e7. https://doi.org/10.1016/j.jcmgh.2017.02.011.

26. Wang, Y.; Kim, R.; Hwang, S.-H. J.; Dutton, J.; Sims, C. E.; Allbritton, N. L. Analysis of Interleukin 8 Secretion by a Stem-Cell-Derived Human-Intestinal-Epithelial-Monolayer Platform. *Anal. Chem.* **2018**, *90* (19), 11523–11530. https://doi.org/10.1021/acs.analchem.8b02835.

27. Hill, D. B.; Vasquez, P. A.; Mellnik, J.; McKinley, S. A.; Vose, A.; Mu, F.; Henderson, A. G.; Donaldson, S. H.; Alexis, N. E.; Boucher, R. C.; et al. A Biophysical Basis for Mucus Solids Concentration as a Candidate Biomarker for Airways Disease. *PLoS ONE* **2014**, *9* (2), e87681. https://doi.org/10.1371/journal.pone.0087681.

28. Mason, T. G. Estimating the Viscoelastic Moduli of Complex Fluids Using the Generalized Stokes–Einstein Equation. *Rheol. Acta* **2000**, *39* (4), 371–378. https://doi.org/10.1007/s003970000094.

29. Srinivasan, B.; Kolli, A. R.; Esch, M. B.; Abaci, H. E.; Shuler, M. L.; Hickman, J. J. TEER Measurement Techniques for in Vitro Barrier Model Systems. *J Lab Autom* **2015**, *20* (2), 107–126. https://doi.org/10.1177/2211068214561025.

30. Allen, A.; Flemström, G. Gastroduodenal Mucus Bicarbonate Barrier: Protection against Acid and Pepsin. *American Journal of Physiology-Cell Physiology* **2005**, *288* (1), C1–C19. https://doi.org/10.1152/ajpcell.00102.2004.

31. Thim, L.; Madsen, F.; Poulsen, S. S. Effect of Trefoil Factors on the Viscoelastic Properties of Mucus Gels. *European Journal of Clinical Investigation* **2002**, *32* (7), 519–527. https://doi.org/10.1046/j.1365-2362.2002.01014.x.

32. Button, B.; Cai, L.-H.; Ehre, C.; Kesimer, M.; Hill, D. B.; Sheehan, J. K.; Boucher, R. C.; Rubinstein, M. A Periciliary Brush Promotes the Lung Health by Separating the Mucus Layer from Airway Epithelia. *Science* **2012**, *337* (6097), 937–941. https://doi.org/10.1126/science.1223012.

33. Yakubov, G. E.; Papagiannopoulos, A.; Rat, E.; Easton, R. L.; Waigh, T. A. Molecular Structure and Rheological Properties of Short-Side-Chain Heavily Glycosylated Porcine Stomach Mucin. *Biomacromolecules* **2007**, *8* (11), 3467–3477. https://doi.org/10.1021/bm700607w.

34. Shchipunov, Y.; Sarin, S.; Kim, I.; Ha, C.-S. Hydrogels Formed through Regulated Self-Organization of Gradually Charging Chitosan in Solution of Xanthan. *Green Chem.* **2010**, *12* (7), 1187–1195. https://doi.org/10.1039/B925138C.

35. Miller, C. C.; Walker, J. The Stokes-Einstein Law for Diffusion in Solution. *Proceedings of the Royal Society of London. Series A, Containing Papers of a Mathematical and Physical Character* **1924**, *106* (740), 724–749. https://doi.org/10.1098/rspa.1924.0100.

36. Coglitore, D.; Edwardson, S. P.; Macko, P.; Patterson, E. A.; Whelan, M. Transition from Fractional to Classical Stokes–Einstein Behaviour in Simple Fluids. *R Soc Open Sci* **2017**, *4* (12). https://doi.org/10.1098/rsos.170507.

37. Gardel, M. L.; Valentine, M. T.; Weitz, D. A. Microrheology. In *Microscale Diagnostic Techniques*; Breuer, K. S., Ed.; Springer: Berlin, Heidelberg, 2005; pp 1–49. https://doi.org/10.1007/3-540-26449-3_1.

38. Jumel, K.; Fiebrig, I.; Harding, S. E. Rapid Size Distribution and Purity Analysis of Gastric Mucus Glycoproteins by Size Exclusion Chromatography/Multi Angle Laser Light Scattering. *International Journal of Biological Macromolecules* **1996**, *18* (1), 133–139. https://doi.org/10.1016/0141-8130(95)01071-8.

CHAPTER 3: CONTROLLING SILANE DIFFUSION FOR GRADIENT APPLICATION OF SURFACE PROPERTIES IN BIOTECHNOLOGY

3.1. Introduction and background

3.1.1. Rationale for using surface property gradients in biotechnology

In order to properly mimic *in vivo* biological applications in *in vitro* cell culture, one major roadblock is recapitulating the wide range of physical microstructures that occur in native tissue [1]. Biological tissue growth is partially guided by localized mechanotransduction, which is fundamentally tied to localized microcurvature in the cell microenvironment [1]. Because tissues display variations in microcurvature and topology even within a tissue type, it is therefore necessary to be able to also replicate those variations with *in vitro* culture [2, 3]. One particular method of accomplishing microcurvature variation is by creating a gradient of a material structure/property on a cell scaffold and measuring cell behavior to compare with native tissue [1]. This allows for proper microstructures to be reconstructed in tissue engineering. In this project, the overall goal is measuring the effects of microcurvature in the intestinal crypt stem cell niche on *in vitro* tissue behavior. In order to accomplish this, it is necessary to generate a gradient of crypt microcurvatures and correlate stem cell behavior with the microengineered physical environment.

3.1.2. Current technologies for generating gradients of surface properties

Primarily, there are two general strategies used to apply gradients of properties on (or in) a material: passive and active. Passive strategies tend to refer to diffusion-based gradients, where molecules diffuse based on thermal motion to expand into areas of low concentration [4]. These types of gradients have been accomplished in a number of ways. For example, gradients of chemical crosslinking within a hydrogel have been accomplished via passive fluid diffusion, creating networks with heterogeneous biophysical properties (such as stiffness, porosity, or degradation rates) at different locations along the applied gradient [5, 6]. It has also been demonstrated that using ECM scaffolds of differing stiffnesses, created via passive diffusion of a crosslinker, can have an effect on cell cultures growing into organoids or contiguous monolayers in colonic epithelial cells [7]. Generally, passive diffusion is a simple protocol and involves little-to-no outside equipment, but it is difficult to control diffusion rates and they can be affected by environmental factors (such as porosity and temperature) [8]. In contrast, active creation of gradient material properties can be achieved via controlled fluid flow (such as in microfluidics), light patterning, compositional control, and other methods [9]. These methods are designed to allow tunable changes on (or in) a material rather than relying on thermal motion and entropy to drive these changes [9]. As an example, creating gradients of mechanical stiffness via microfluidic addition of a crosslinker to a hydrogel has demonstrated that cell growth and propagation (specifically for neurites) can be altered and guided by growing them on collagen surfaces of progressively higher stiffnesses within the same culture [10]. It has also been demonstrated that using ECM scaffolds of differing stiffnesses can have an effect on cell cultures growing into organoids or contiguous monolayers in colonic epithelial cells [7]. Outside factors can also be applied to create gradients, such as using ultraviolet light sources to crosslink photoreactive hydrogels in a gradient along a surface [11]. While active methods can offer a

higher degree of control of a specific gradient of properties, they can also require specific, costly materials and equipment in order to accomplish, and can take more time than passive methods to be accomplished [8].

Because *in vivo* tissue displays heterogenous gradients of physical properties [12, 13], it is important to be able to replicate those conditions in *in vitro* tissue-engineered systems. These applications of passively-generated physical gradients show that being able to alter the surface properties of a scaffold prior to cell culture can have major downstream effects on the behavior of *in vitro* tissue. For a range of surface properties specifically, gradients of application could be used to alter the properties of a microfluidic system to make it more suitable for fluid flow and cell growth [14, 15]. They could also be used within lithographic synthesis of bioscaffold master templates to create gradients of mechanical properties along the surface of a bioscaffold stamp [16]. In this project, the focus was placed on passive diffusion for the creation of surface property gradients.

3.1.3. Diffusion mechanics

Fluid diffusion is a well-studied phenomenon of molecular movement of compounds from areas of high concentration to low concentration. In a fluid, particles move randomly due to thermal or Brownian motion, causing them to collide with each other and with the confines of their container [4]. These collisions naturally drive a particle from an area of high concentration (with many collisions) to an area of low concentration (with less collisions) [4]. This is a passive process without any additional energy input, allowing for concentrations of particles to spread themselves out evenly over time [4]. Diffusion is a naturally occurring phenomenon in biology, with passive diffusion driving metabolites both into and out of cells regularly [17]. Diffusion

occurs in liquid or gas form, though it tends to occur more quickly in gases due to higher kinetic energy expressed by gaseous particles [17]. Pure solids do not experience noticeable diffusion due to the low kinetic energy and rigid structure, but porous solids (such as hydrogels) can experience diffusion at slower rates than fluids [17]. Because gaseous diffusion is the most rapid form, it can be useful to transition a compound of interest from the liquid phase to the gas phase before diffusion. By briefly exposing a small amount of liquid to vacuum, the liquid phase can be transitioned into gas phase by decreasing the pressure within the chamber that holds the liquid molecules together. Once this occurs, entropy drives the gaseous molecules of the vaporized liquid to spread out within the chamber, equilibrating concentration of the compound evenly throughout the space [4].

A number of factors contribute to the rate at which a liquid vaporizes and diffuses within a vacuum: molecular weight of the compound, size of the diffusion area, the strength and duration of the vacuum applied, temperature, and the concentration of the compound within the chamber [18]. In addition to these factors, the diffusivity of a material, also described as it's diffusion coefficient (D), is an inherent material property which describes how quickly a fluid will diffuse. The interaction of these variables together was described by Adolf Fick in the 19th century, collated into Fick's first and second laws of diffusion [19]:

$$J = -D\frac{\partial \varphi}{\partial x}$$

and

$$\frac{\partial \varphi}{\partial t} = D\frac{\partial^2 \varphi}{\partial x^2}$$

In these equations, J is the diffusion flux (or concentration of diffused material per unit area per unit time), D is the diffusion coefficient, φ is the concentration of the material, and x and t are

the position and time, respectively. These formulas can be used to describe diffusion in fluid environments (both liquid and gaseous) under ideal conditions [19]. Assuming a source-sink model with an "infinite" (or sufficiently high concentration) source of a compound, and a sink area with zero or very little concentration of the same compound, diffusion can create a gradient of compound concentration that measurably decreases as it moves from the source into the sink. This gradient can have useful biotechnology applications for its downstream surface or material property gradient effects.

3.1.4. Silanes and their uses for biotechnology

For this project, a gradient of surface tension was desirable in order to set up the development of biomedical lithographic techniques (described in Chapter 4). Silicon-hydrocarbon compounds known as *organosilanes* play a number of roles, notably as a surface treatment for microfluidic devices in a process known as silanization [20]. Silanization typically involves the liquid or vaporous deposition of an organosilane onto a microfluidic surface, changing the surface's properties in a number of potential ways [21]. Organosilanes are particularly useful in surface modification of solids because hydroxyl groups (and other hydrocarbon groups) can bind strongly and steadily with the silicon atoms within the silane, allowing solid monolayers of silane deposition across an appropriate surface [22]. Monolayers coated along microsurfaces are desirable for multiple applications in biotechnology for their ability to act as attachment sites for ligands of interest, functionalizing a surface for stronger ligand specificity [23]. As an example, this is usable for binding nucleotides and DNA to a surface coated with an amine-bonded organosilane layer [24]. As another example, silanization has been used to mitigate the extreme hydrophobicity of native polydimethysiloxane (PDMS), allowing for surface functionalization of the PDMS to increase cell adhesion/viability [25].

Silanization is also usable with natural polymer hydrogels; for example, it has been used to treat a hydroxypropyl methylcellulose hydrogel scaffold for chondrocyte differentiation, as well as porous chitosan scaffolds for improved degradation rates [26, 27]. In general, silanization has value in bioengineering because the increased binding affinities of many organosilane monolayers allows for increased cell and protein adhesion [27].

Silane deposition can be accomplished in either liquid-phase or vapor-phase. For this study, vapor-phase deposition was chosen as the silanization method, as it allowed for a more controllable diffusion profile on surfaces of interest [28]. By using multiple chambers under vacuum, a source-and-sink model could be constructed to allow for diffusion of an organosilane in a measurable, repeatable pattern. This is a desirable outcome, as controlling the concentration of organosilane deposition could allow to downstream control of surface modification effects.

3.2. Materials and methods

3.2.1. Silane vaporization and diffusion

Prior to use, standard glass slides were cleaned with 70% ethanol, deionized water, and dried with compressed nitrogen. The slides were then treated with oxygen plasma for 5 min. Inside a polycarbonate desiccator (08-642-7; Thermo Fisher, Fremont, CA), a glass side was placed with the plasma-treated side facing upwards. Then a secondary, 3D-printed rectangular chamber with one side open was taped on top of the glass slide (1mm, 2mm, or 4mm in height; 30 mm × 30 mm in length/width). The synthesis method for these secondary chambers is described in Section 3.2.2. In a petri dish in the center of the desiccator, a volume of (3-aminopropyl)triethoxysilane (APTES) was deposited (either 100 µL or 500 µL; 0.06 mol/m^3 and 0.3 mol/m^3). The chamber was placed under a 95 kPa vacuum for 5 min to vaporize the silane, then left vacuum sealed for a period of time between 2-24 h to allow for diffusion of the silane

into the secondary chamber and across the surface of the glass slide. After diffusion, the slides were removed, separated from their secondary chamber, and placed in a foil-covered container to await staining.

3.2.2. 3D printing of secondary diffusion chambers to create gradient silane deposition

All secondary diffusion chambers were initially rendered on Solidworks CAD software (version 2016). Each chamber was designed to have a rectangular prismatic cavity in its center, 30 mm × 30 mm in length/width, with variable heights of 1 mm, 2 mm, or 4 mm. The 3D printing filament used was polylactic acid (PLA), and the 3D printer used was the Prusa i3 MK3 (Prusalab; Czechia).

3.2.3. Staining of silane deposition

Solutions of 5 µg/mL of Alexa Fluor 594 NHS Ester in 1X PBS were prepared in foil-covered tubes (A37572; Thermo Fisher, Fremont, CA). Underneath the foil, each tube was covered with polyimide tape (8997; 3M, St Paul, MN) to prevent additional light from interacting with the fluorescent solution. Once prepared, 200 µL of this solution was applied to the region of the silanized glass slides. These were incubated at 25°C for 45 min, covered from light. After staining, excess solution was removed, and the slide was gently washed with 70% ethanol to remove any remaining unbonded fluorescent dye.

3.2.4. Confocal microscopy imaging

After staining, the amine-conjugated slides were imaged within 24 h before significant hydrolysis of the silane or photobleaching of the fluorophore could occur. The slides were then placed on the stage of an Olympus IX83 Research Inverted Microscope and imaged with a 4X air objective at constant laser power and voltage. The slides were imaged at 0.5 cm increments, from the slice that had been at the opening of the secondary chamber (x=0 cm) to the slice that had

been at the back of the chamber (x=3 cm). To control for variability, 5 images were collected at each x-region, and 5 randomly selected points within each of these images was measured for average fluorescence intensity via ImageJ software. Each of these experimental trials was conducted at least 3 times to account for sample-to-sample variability.

3.2.5. Computational modeling of a silane gradient diffusion profile

When analytical solutions were not available, numerical solutions were computed using Mathematica (Wolfram, Champaign, IL).

3.2.6. Statistics

To determine statistical significance, groups were compared via two-mean, two-tailed t tests with 99% confidence intervals ($p < .01$). With large sample sizes, groups were assumed to be approximately normal distributions.

3.3. Results and discussion

3.3.1. Overview of silane vaporization, deposition, and staining

Using an oxygen plasma-treated glass slide, a diffusion system for vaporized silane was developed in order to create a gradient of silane in a controlled manner, and thus to create a gradient of potential surface modification (Fig 1). The glass slide was attached to a secondary diffusion chamber within the overall larger chamber, and then an aminosilane was vaporized via vacuum exposure within the overall system. This created a gradient of aminosilane across the treated glass slide which could be imaged and quantified by incubating the slide with an amine-binding fluorophore.

The addition of a secondary, smaller chamber with only one opening into a vacuum space where diffusion is occurring can allow for more controlled diffusion of the vaporized silane. Once vaporized and spread within the larger chamber, the concentration of the silane can be

considered as a source, and the interior of the secondary chamber can be considered as a sink [29]. The silane will start at the opening of the secondary chamber and flow inside the chamber, depositing along the surface attached to the bottom of that chamber. Along the chamber length, it becomes harder for the silane molecules to diffuse further into the chamber, as the mean free path of each silane molecule is small enough that it is probabilistically more difficult for silane to reach the back of the chamber [30]. As the time scale is allowed to increase, eventually the surface area inside the secondary chamber will reach saturation levels of silane deposition. Before this occurs, however, a gradient of silane can be observed along the surface inside the secondary chamber, moving from high concentrations of silane near the entrance to lower concentrations of silane near the back of the chamber [30]. As discussed, using a silane coating can alter the material properties of a surface, and thus having a gradient of this surface coating could lead to a gradient in surface properties and the surface's subsequent applications, especially for use in biotechnology [31, 32, 33].

3.3.2. Confirming silane deposition *in vacuo* and silane staining without a gradient

In order to stain, image, and quantify a gradient of silane deposition, the necessary first step was confirming that silane could be coated on a surface and then bound to a fluorescent ligand. For this study, APTES was chosen due to an exposed amine group, allowing for an amine-specific fluorescent dye to be used to conjugate the silane and provide a quantifiable fluorescence signal. Further, other research groups have already shown that surfaces functionalized with APTES deposition have been successfully used in cell culture, playing roles in modifying cell viability and scaffold mechanical properties [34, 35]. N-hydroxysuccinimidyl ester (also known as NHS ester) conjugated with Alexa Fluor 594 was chosen as a fluorescent

label for the aminosilane due to its high amine reactivity and specificity [36]. Once the silane and fluorophore were chosen, plasma-treated glass slides were silanized and stained at 2 h intervals from 2-24 h, as described in Sections 3.2.1 and 3.2.3, without the addition of a secondary diffusion chamber attached to the surface of each slide. These slides were then imaged and their relative fluorescence measured as described in Section 3.2.4.

Once measured, it was observed that the fluorescence of each slide had a direct relationship with the amount of time the slide was silanized, displaying higher average fluorescent intensities with longer silanization times (Fig 2). At each 2 h interval between 8-20 h, there was a statistically significant increase in average fluorescence intensity (and thus silane deposition), increasing steadily from 126±10 RFU to 235±5 RFU (Fig 2d). The lack of a significant difference between 20-22 h, and then between 22-24 h, could indicate that silane deposition was beginning to reach saturation at those times. There were also differences in fluorescence standard deviation at increasing silanization times. At short silanization times (2-8 h), there was a high degree of heterogeneity in the average fluorescence intensity, with standard deviations between 10-15 RFU. As silanization time was increased, it was noted that heterogeneity of fluorescence generally decreased, measured as low as 4 RFU at 24 h of silanization time. In physical terms, this could indicate that longer silanization times allow for a more homogeneous coating of silane along the entirety of the treated surface, which follows the observed properties of diffusion as time scales increase. Overall, this section of experiments demonstrated that the underlying principle of silane deposition and subsequent staining was possible on separate glass slides. The next step, based on the need in tissue engineering for high throughput screening, was determined to be the formation of a gradient in silane deposition, allowing for multiple surface conditions to be tested on one device.

3.3.3. Creating a quantifiable gradient of silane diffusion via a secondary chamber

To create the desired gradient of aminosilane deposition on a single surface, secondary diffusion chambers were constructed (Figure 1) and attached to the treated glass slides as described in Sections 3.2.1 and 3.2.2 (width of 30 mm; heights of 1 mm, 2 mm, 4 mm; lengths of 20 mm, 30 mm, 50 mm). With the secondary chamber attached to the glass slide, the plasma-treated side of the surface was accessable by the vapor-phase silane through the single opening on the side of the chamber. This was hypothesized to create a gradient of silane deposition with a greater amount of silane deposited at the opening on the secondary chamber relative to that deposited deeper into the chamber. On the non-silanized side of each slide, markings were made every 0.5 cm from the opening of the chamber to the back of the chamber, denoting locations for images (x=0 to x=3.0). For this section of experiments, 100 µL of silane was vaporized within the primary diffusion chamber. At 2 h intervals between 2 and 24 h, silane was deposited, reacted with the NHS ester fluorophore, and then imaged. The average fluorescence intensity was then quantified along the surface of the slide (Fig 3). It was observed that fluorescence generally showed a decrease in intensity as x increased from 0 to 3.0 cm, providing evidence for the hypothesis that the secondary supported the deposition of a gradient of silane. For all of the secondary chamber heights, there was a statistically significant difference in fluorescence between the area at x = 0 cm and the area at x = 3.0 cm for every diffusion time. This indicates that the amount of silane deposited had not saturated the available binding sites on the slide during much of this time span. There was also a general trend of an increase in average fluorescence intensity with increasing diffusion time at most time points for each chamber,

providing supporting evidence to the findings in Section 3.3.2. It should be noted that there were a few instances where this did not hold true, but these instances can likely be explained by sample-to-sample variance, as they were not consistently statistically significant.

One important and unexpected phenomenon was observed regarding differences in gradient formation based on the height of the chamber. It was initially hypothesized that all of the chamber heights would display a similar gradient for all time points, as the height of the chamber (1 mm – 4 mm) is significantly shorter than the length of the chamber (30 mm), meaning that any height-related changes in diffusion along the chamber would be minimal [37]. Experimentally, this was not shown to be the case, as fluorescence values at x = 0 cm were independent of secondary chamber height, but fluorescence values at x = 3.0 cm were not. Fluorescence at x = 3.0 cm was statistically significantly higher with 4 mm chamber height instead of both 1 mm and 2 mm chamber heights starting at 6 h of diffusion, and they were statistically significantly higher with 2 mm chamber height instead of 1 mm chamber height starting at 18 h of diffusion. Potential explanations for this include convection effects occurring during the initial vacuum vaporization of the silane driving silane more forcefully through the larger openings, though this was thought to be unlikely as the vacuum vaporization step was a much shorter time scale (5 min) compared to even the smallest diffusion time scale (2 h) [38]. The more likely potential explanation would be depletion of the local concentration of vaporous silane in the primary diffusion chamber as silane is deposited in both chambers. The secondary chamber height was not expected to affect the gradient of silane deposition assuming an infinite yet constant concentration of silane. However, it is possible that vaporized silane was consumed over time leading to a decreasing concentration of silane in the chamber itself over time. This would then decrease the amount of silane available to diffuse and deposit onto the surface within

the secondary diffusion chamber. This theory will be tested and discussed in Section 3.3.5 by using a higher source concentration of vapor-phase aminosilane.

A few observations were also made about trends in variance for these fluorescence measurements. First, it was noted that variance at x = 0 cm was usually smaller than at other points along the surface, even at short time scales. This suggests that the opening of the chamber had access to the most homogenous concentration of silane compared to the rest of the surface inside the secondary chamber. Secondly, it was noted that short time scales tended to display less variance in fluorescence at points where x approached 3.0 cm compared to longer time scales. Physically, this could likely be explained by the silane not having sufficient time to adequately diffuse that far into the secondary chamber, and because the fluorescence was much closer to 0, had less opportunity for intensity variance. Overall, this section of experiments displayed that a gradient deposition of vapor-phase silane was possible and controllable via diffusion time and (unexpectedly) secondary chamber height. The next step was determining the effects of secondary chamber length on the deposition, as biotechnology applications would inherently require surfaces of different lengths for different purposes.

3.3.4. Testing the effects of secondary chamber length on silane diffusion gradient

Using the same protocols from Sections 3.2.1-3.2.3, secondary diffusion chambers of constant width (30 mm) but varying lengths (20 mm, 30 mm, 50 mm) and heights (1 mm, 2 mm, 4 mm) were synthesized and used for aminosilane gradient deposition with 100 µL of vaporous silane for 16 h. After staining, the surfaces were imaged every 0.5 cm along slide within the secondary chamber. The fluorescence was then quantified along the length of the slide (Fig 4). It was observed that the different chamber heights displayed a height-based discrepancy in silane deposition as x increased as was found in Section 3.3.3. It was also observed that, at the same

distance from the opening (up to x = 2.0 cm), similar gradient profiles were observed independent of chamber length. For each chamber height and length, a statistically significant decrease in fluorescence intensity was measured. Beyond those points (as x approached 5.0 cm for the longest chamber), a steady decrease in fluorescence intensity was observed, going as low as 6 RFU for the 50 mm length chamber and 26 RFU for the 30 mm length chamber. For the shortest chamber (20 mm), this fluorescence decreased was not observed as x approached 2.0 cm. Physically, this indicates that silane had more difficulty penetrating into the longer chambers, likely due to insufficient diffusion time to travel deeply into the chamber. Experimentally, increasing vapor-phase silane concentration or diffusion time (as was done in Section 3.3.3) could potentially be used to control gradients at differing length scales.

3.3.5. Testing the effects of higher vaporous silane volumes on silane gradient profile

The findings in Section 3.3.3 suggested the hypothesis that depletion of silane was having effects on the silane gradient formation. For this reason, higher concentrations of vapor-phase silane (i.e. a larger volume of liquid silane) were loaded into the primary chamber. In this section, 500 µL of silane (instead of the previously used 100 µL) was placed into the primary chamber and permitted to diffuse into the secondary diffusion chamber, with constant chamber length (30 mm) and varied chamber heights (1 mm, 2 mm, 4 mm) and diffusion times (8, 12, 16 h). It was hypothesized that using this higher concentration of silane would lead to a gradient of silane independent of chamber height by mimicking more closely an infinite source of constant concentration of vapor-phase silane. After the surfaces were silanized, labeled with a fluorophore, and imaged, evidence was found that supported this hypothesis (Fig 5). Whereas in previous sections, a clear difference in diffusion gradient was found based on variable chamber height, a similar difference was not observed at this higher concentration of vaporous silane.

Statistically significant gradients were observed for all times and all chamber heights in this set of experiments. It was observed that overall, 500 µL of vaporous silane generated significantly higher intensity values than 100 µL did at x = 0 cm. For 1 mm, 2 mm, and 4 mm chamber heights respectively, 500 µL of silane generated base fluorescences at x = 0 cm of 228±16 RFU, 338±17 RFU, and 405±15 RFU. These values were much higher than the values produced by 100 µL of silane at 127±10 RFU, 192±6 RFU, and 208±6 RFU for 1 mm, 2 mm, and 4 mm chamber heights, respectively. Physically, this indicates that a higher amount of silane was available for deposition, and thus more amine groups were available for binding to the amine-specific fluorophore. Finally, it was observed that variance in fluorescence intensities was typically lower at 500 µL compared to 100 µL; this likely indicates a more homogenous deposition of silane, stemming from the larger source of available silane for deposition in the case of 500 µL.

3.3.6. Modeling silane diffusion data

Using the experimental data collected in Sections 3.3.1-3.3.5, it was possible to generate computational models for explaining the method of silane vapor deposition, as well as predicting silane deposition for other conditions not tested experimentally. The first step in accurately modeling silane diffusion in this situation was solving the one-dimensional diffusion equation,

$$\frac{\partial c}{\partial t} = \kappa \frac{\partial^2 c}{\partial x^2}$$

where c(x,t) is the silane concentration at time t and at some distance within the chamber x, and κ is the silane diffusion constant. In a simple 1D diffusion problem, the silane concentration at the inlet of the secondary chamber would be assumed to be a constant c_0, and the silane concentration at the back of the chamber would be assumed to be 0 at t = 0. However, during the initial silane vaporization, rapid evacuation of the primary diffusion chamber generates

convective effects that drive the silane into the secondary chamber by some distance, a (Fig 6a). This sets up the initial conditions of

$$c(x,0) = \begin{cases} c_a\,, x < a \\ 0\,, x > a \end{cases}$$

where c_a is the silane concentration for $0 < x < a$. When compared to experimental results, the theoretical predictions generated under these conditions did not appropriately model the experimental data. One theory for this discrepancy was a non-instantaneous deposition of silane after vaporization, indicating the need for a diffusion-deposition model. For this experimental setup, the diffusion-deposition model is governed by

$$\frac{\partial I}{\partial t} = k\,(\frac{c(x,t)}{c_a})(I_0 - I)$$

where I(x,t) is the measured fluorescence intensity (assumed to be proportional to silane deposition) at some distance x and time t, and $\frac{c(x,t)}{c_a}$ is the previously determined amount of silane diffused into the chamber. In this case, k and I_o are unknown constants which must be determined experimentally.

The first step to fully solving this equation was finding k and I_0, which was done using fluorescence intensity from slides without a secondary diffusion chamber. In this case, $c(x,t) = c_a$ and the solution to the above equation is

$$I(x,t) = I_0(1 - e^{-kt})$$

By applying a best fit curve to the experimental data of intensity with 500 µL of vaporous silane and no gradient, values of $k = 0.093\ hr^{-1}$ and $I_0 = 503.8$ were found (Fig 6b). Because the constant k is the inverse of the time scale of diffusion, the time scale of diffusion was found to be 10.75 h. Additionally, by using the experimental gradient data at 500 µL for chambers with 1

mm height, a value of a was approximated by finding a theoretical value with the smallest root mean squared error compared to experimental results. This value was found to be a = 1.4 cm.

After finding values of all necessary constants, the diffusion-deposition theoretical model could be compared to the gathered experimental data. By assuming a = 1.4 cm and solving for the gradient profile in a 1 mm height secondary chamber, the theoretical diffusion model was plotted against the experimental data at 8, 12, and 16 h (Fig 6c). While still imperfect, this model provides a relatively close model of the physically observed aminosilane diffusion. The fluorescence intensity values at x = 0 cm and at x = 3.0 cm were comparable between the model and the experimental data. One discrepancy between the model and the experimental data was an observed plateau layer of fluorescence near the opening of the chamber that was not predicted using the model. This discrepancy increased as diffusion time was increased and is most noticeable at 16 h of diffusion. It is possible that this was due to the initial convective effects during vaporization, or could potentially be explained by vaporous silane bonding more readily to silane that has already been deposited on the surface of the glass substrate than to the glass substrate itself.

3.4. Conclusions and acknowledgements

In summary, this set of experiments gave strong evidence that vapor-phase silane deposition can be guided via experimental controls, allowing for gradient deposition of the silane across a single surface. Using a secondary diffusion chamber, significant gradients of silane deposition were observed, directly related with vapor-phase silane concentration and diffusion time. Unexpectedly, the height of the secondary diffusion chamber also displayed an effect on the diffusion gradient at lower silane concentrations, with taller openings of the chamber allowing more silane in relative to the shorter openings. Because this effect was not observed at

higher silane concentrations inside the primary diffusion chamber, it is hypothesized that below a benchmark silane concentration, depletion effects will occur and prevent the silane within the primary chamber from acting as a constant concentration source for vapor-phase diffusion. For future work, different volumes of silane could be tested incrementally to find what this benchmark silane concentration is, as well as a wider range of lengths of the secondary diffusion chamber. Finally, different shapes of the secondary diffusion chamber could be tested in the future (radial, trapezoidal, triangular, chambers with increasing or decreasing height, etc). This would potentially allow for gradients other than purely linear ones to be observed and applied in biotechnology.

The author would like to thank Raehyun Kim and Yuli Wang for experimental advice and training on confocal microscopy. The author would also like to thank NSF GRFP Grant # 2016212411 and NIH # DK109559 for funding.

3.5. Figures

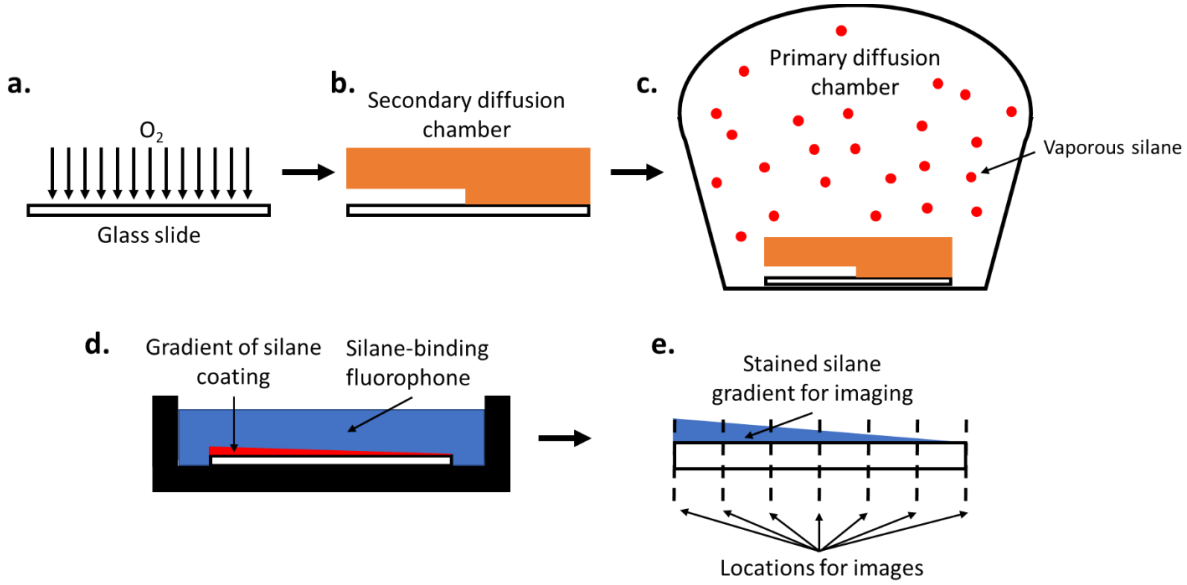

Figure 3.1. Schematic of aminosilane diffusion and staining. Schematic of gradient aminosilane diffusion and subsequent staining/imaging. a) A clean glass slide is treated with oxygen plasma for 5 min. b) A secondary diffusion chamber, 3D-printed, is attached to the plasma-treated side of the surface. This allows one opening for the entrance of silane from the larger primary diffusion chamber into the diffusion chamber. c) The glass slide with an attached secondary diffusion chamber is placed within the primary diffusion chamber. A petri dish containing liquid-phase aminosilane is also placed in the primary diffusion chamber. The primary diffusion chamber is then placed under vacuum, driving the aminosilane into vapor-phase. The chambers are incubated for a time that is insufficient for the silane to equilibrate and reach a uniform concentration within the secondary diffusion chamber. d) After a gradient is formed, the glass slide is removed from the primary diffusion chamber, decoupled from the secondary chamber, and incubated with an amine-specific fluorophore. e) Linear scans along the slide perpendicular to the axis of the surface modification gradient are then conducted. The line

scans are performed every 0.5 cm along the region that was contained within the secondary diffusion chamber.

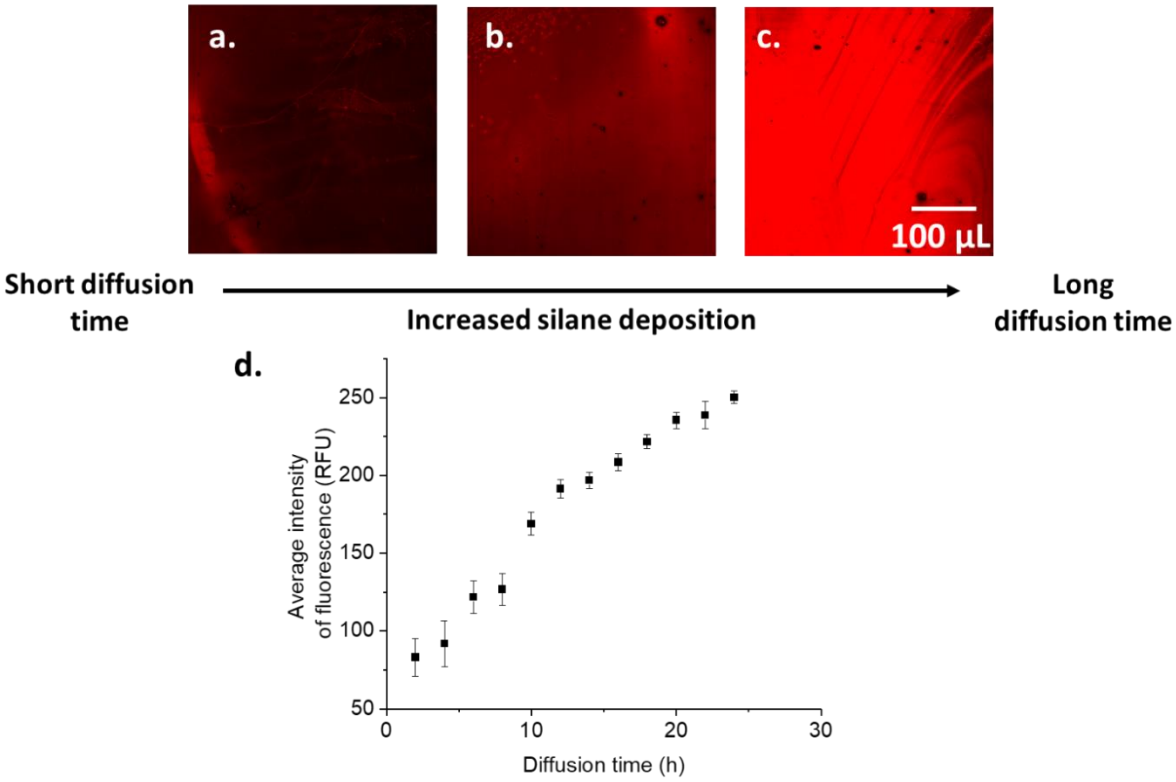

Figure 3.2. Establishing the effectiveness of aminosilane deposition and staining a-c) Images collected of silanized and fluorescently-stained glass slides at increasing diffusion times (2, 8, 16 h) without a secondary diffusion chamber. These images display a clear increase in silane deposition and fluorescence at longer time points and provide a base level of fluorescence before a gradient was formed using a secondary diffusion chamber. d) Quantified average intensity of fluorescence at 2 h intervals of silanization. These values were collected from 25 images per slide, randomly chosen. All trials were conducted 3 times to control for variability.

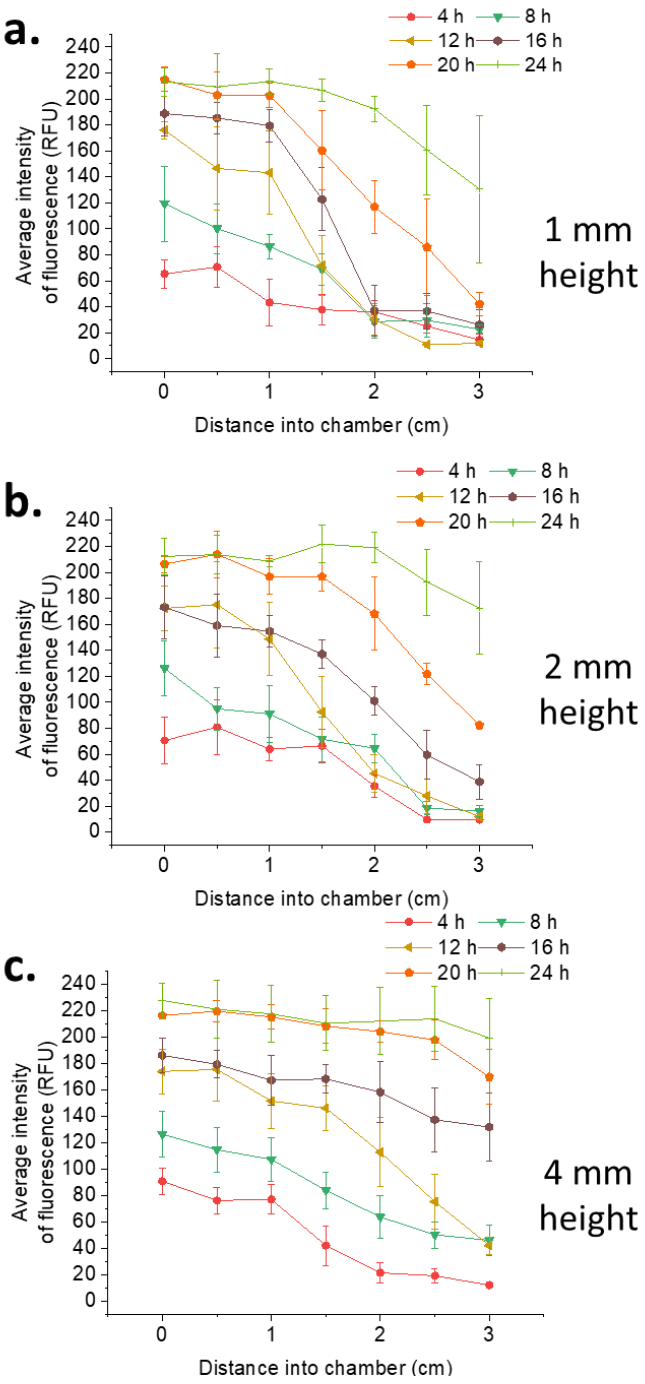

Figure 3.3. Measuring the effect of diffusion time on silane penetration into secondary diffusion chambers of differing heights and constant length. Average fluorescence intensity was measured at 0.5 cm increments along surfaces that were coupled with 30 mm long secondary

diffusion chambers, using varying diffusion times (2 h increments between 2 and 24 h). Three different chamber heights were tested, at 1 mm (a), 2 mm (b), and 4 mm (c). Each of these systems displayed statistically significant gradients of silane deposition along the length of each chamber from the opening of the chamber to the back of the chamber. All measurements in this set of experiments were done with 100 µL of vapor-phase aminosilane.

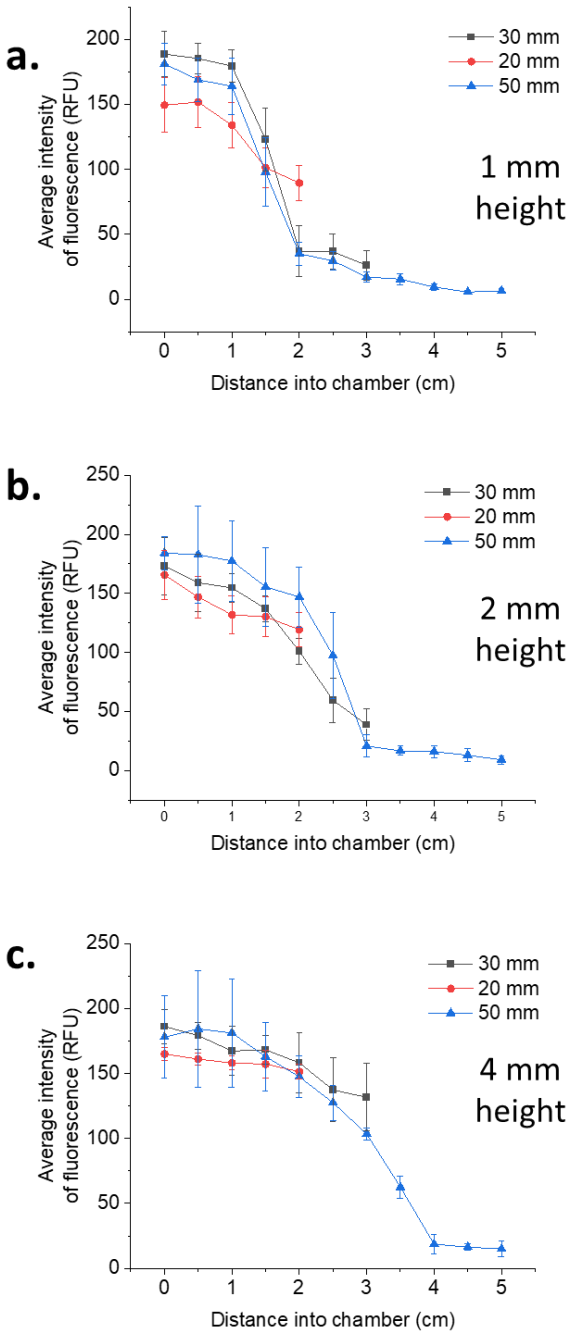

Figure 3.4. Measuring the effect of chamber length on silane penetration into secondary diffusion chambers of differing heights at constant diffusion time. Average fluorescence intensity was measured at 0.5 cm increments along slide surfaces for secondary diffusion chambers of varying length (20 mm, 30 mm, and 50 mm). 16 h of silane diffusion was allowed

in each case, as this time-frame had displayed gradient deposition in earlier experiments. Three different chamber heights were tested, at 1 mm (a), 2 mm (b), and 4 mm (c). It was seen that, at locations approaching x = 0 cm for each chamber length, similar gradients were observed. It was also observed the fluorescence (and therefore silane deposition) was limited as x increased in the longer chambers. All measurements in this set of experiments were done with 100 µL of vapor-phase aminosilane.

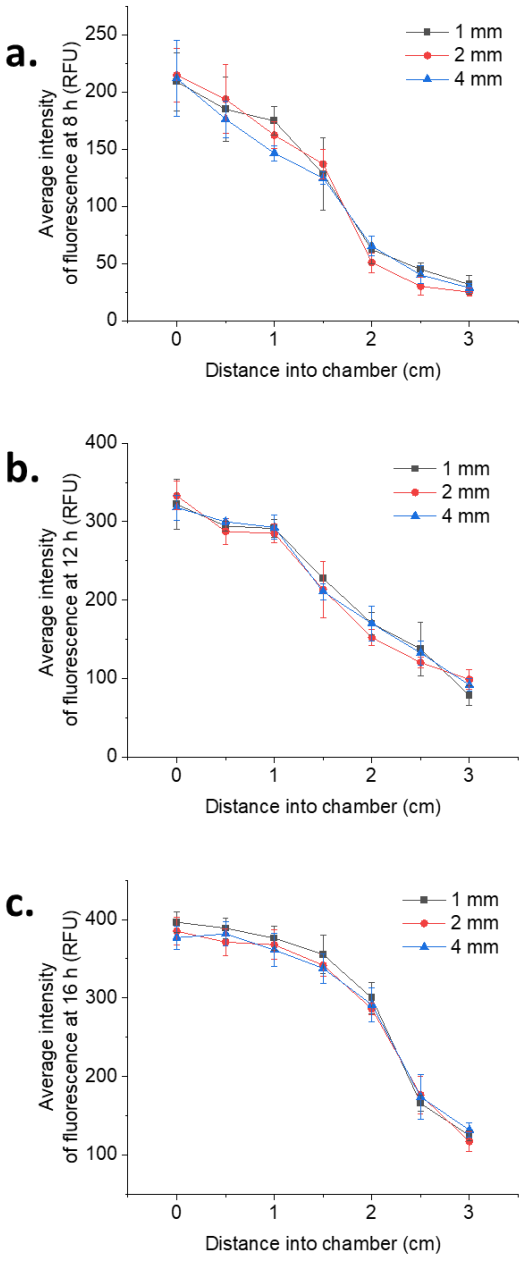

Figure 3.5. Measuring the effect of increased vaporous silane concentration on height-based differences in diffusion in secondary diffusion chambers. Average fluorescence intensity was measured at 0.5 cm increments along surfaces that were placed within 30 mm long secondary diffusion chambers, using varying diffusion times (8 h, 12 h, 16 h). 500 µL of vapor-phase silane was used to create silane deposition gradients. Three different chamber heights were

tested, at 1 mm (a), 2 mm (b), and 4 mm (c). Each of these systems displayed statistically significant gradients of silane deposition along the length of each chamber, comparing the opening of the chamber to the back of the chamber. Also, there was no significant difference observed relative to the secondary chamber height at any point, giving evidence that depletion effects were in play at lower silane concentrations.

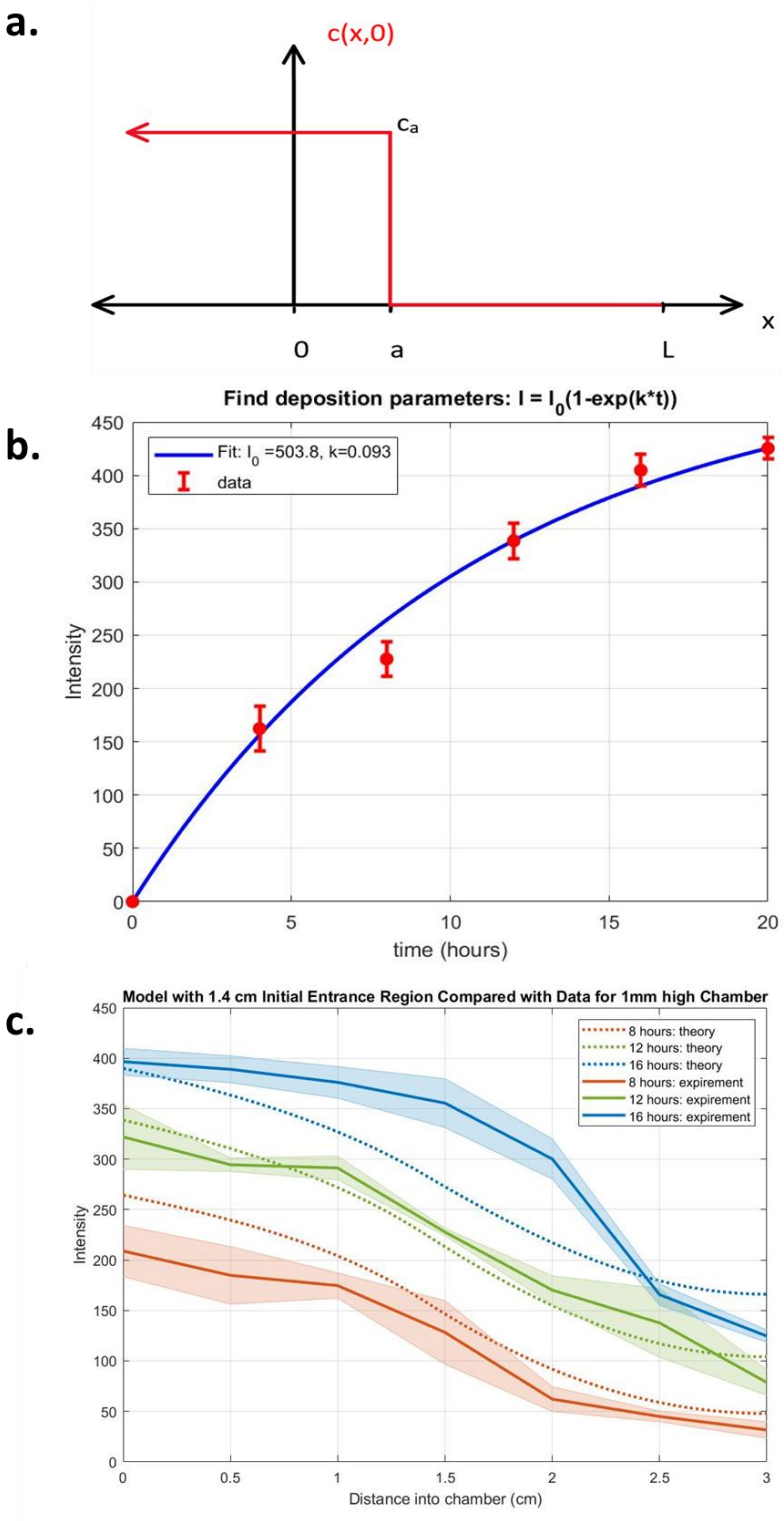

Figure 3.6. Computationally modeling aminosilane gradient diffusion. (a) The diffusion-deposition model assumed that initial vaporization of the liquid silane drove molecules some

distance a into the secondary diffusion chamber via convection. This generated a boundary condition of concentration c_a when $0 < x < a$. (b) By comparing the solution of the diffusion-deposition model to fluorescence measurements without using a secondary chamber (where $c(x,t) \sim c_a$, assumed to be constant), values of the constants I_0 and k were found. (c) After finding both I_0 and k, a solution for the total diffusion-deposition model was plotted against experimental data at 8, 12, and 16 h from 1 mm chamber height trials.

REFERENCES

1. Egan, P. F.; Shea, K. A.; Ferguson, S. J. Simulated Tissue Growth for 3D Printed Scaffolds. *Biomech Model Mechanobiol* **2018**, *17* (5), 1481–1495. https://doi.org/10.1007/s10237-018-1040-9.

2. Deng, L.; Jin, Y.; Luo, M. Micro-Curvature Environment Is a Determinant of Airway Smooth Muscle Cell Orientation and Stiffness During Early Pattern Formation in Culture. In *B30. MECHANISMS OF AIRWAY SMOOTH MUSCLE CONTRACTILITY AND RELAXATION: POTENTIAL THERAPEUTIC TARGETS*; American Thoracic Society International Conference Abstracts; American Thoracic Society, 2017; pp A3154–A3154. https://doi.org/10.1164/ajrccm-conference.2017.195.1_MeetingAbstracts.A3154.

3. Sun, B.; Lam, R. H. W. Influence of Micro-Scale Substrate Curvature on Subcellular Behaviors of Vascular Cells. In *2016 IEEE 16th International Conference on Nanotechnology (IEEE-NANO)*; 2016; pp 339–342. https://doi.org/10.1109/NANO.2016.7751337.

4. Marquardt, N. *Introduction to the Principles of Vacuum Physics*; CERN, 1999.

5. Burdick, J. A.; Khademhosseini, A.; Langer, R. Fabrication of Gradient Hydrogels Using a Microfluidics/Photopolymerization Process. *Langmuir* **2004**, *20* (13), 5153–5156. https://doi.org/10.1021/la049298n.

6. Wong, J. Y.; Velasco, A.; Rajagopalan, P.; Pham, Q. Directed Movement of Vascular Smooth Muscle Cells on Gradient-Compliant Hydrogels. *Langmuir* **2003**, *19* (5), 1908–1913. https://doi.org/10.1021/la026403p.

7. Wang, Y.; DiSalvo, M.; Gunasekara, D. B.; Dutton, J.; Proctor, A.; Lebhar, M. S.; Williamson, I. A.; Speer, J.; Howard, R. L.; Smiddy, N. M.; et al. Self-Renewing Monolayer of Primary Colonic or Rectal Epithelial Cells. *Cellular and Molecular Gastroenterology and Hepatology* **2017**, *4* (1), 165-182.e7. https://doi.org/10.1016/j.jcmgh.2017.02.011.

8. Hennink, W. E.; van Nostrum, C. F. Novel Crosslinking Methods to Design Hydrogels. *Advanced Drug Delivery Reviews* **2012**, *64*, 223–236. https://doi.org/10.1016/j.addr.2012.09.009.

9. Wang, P.-Y.; Tsai, W.-B.; Voelcker, N. H. Screening of Rat Mesenchymal Stem Cell Behaviour on Polydimethylsiloxane Stiffness Gradients. *Acta Biomaterialia* **2012**, *8* (2), 519–530. https://doi.org/10.1016/j.actbio.2011.09.030.

10. Sundararaghavan, H. G.; Monteiro, G. A.; Firestein, B. L.; Shreiber, D. I. Neurite Growth in 3D Collagen Gels with Gradients of Mechanical Properties. *Biotechnol. Bioeng.* **2009**, *102* (2), 632–643. https://doi.org/10.1002/bit.22074.

11. Seppälä, J.; Korhonen, H.; Hakala, R.; Malin, M. Photocrosslinkable Polyesters and Poly(Ester Anhydride)s for Biomedical Applications. *Macromolecular Bioscience* **2011**, *11* (12), 1647–1652. https://doi.org/10.1002/mabi.201100198.

12. Chrastina, A.; Massey, K. A.; Schnitzer, J. E. Overcoming in Vivo Barriers to Targeted Nanodelivery. *WIREs Nanomedicine and Nanobiotechnology* **2011**, *3* (4), 421–437. https://doi.org/10.1002/wnan.143.

13. Seidi, A.; Ramalingam, M.; Elloumi-Hannachi, I.; Ostrovidov, S.; Khademhosseini, A. Gradient Biomaterials for Soft-to-Hard Interface Tissue Engineering. *Acta Biomaterialia* **2011**, *7* (4), 1441–1451. https://doi.org/10.1016/j.actbio.2011.01.011.

14. S. Lee, K.; J. Ram, R. Plastic–PDMS Bonding for High Pressure Hydrolytically Stable Active Microfluidics. *Lab on a Chip* **2009**, *9* (11), 1618–1624. https://doi.org/10.1039/B820924C.

15. R. Abate, A.; T. Krummel, A.; Lee, D.; Marquez, M.; Holtze, C.; A. Weitz, D. Photoreactive Coating for High-Contrast Spatial Patterning of Microfluidic Device Wettability. *Lab on a Chip* **2008**, *8* (12), 2157–2160. https://doi.org/10.1039/B813405G.

16. Balowski, J. J.; Wang, Y.; Allbritton, N. L. Fabrication of 3D Microstructures from Interactions of Immiscible Liquids with a Structured Surface. *Adv. Mater. Weinheim* **2013**, *25* (30), 4107–4112. https://doi.org/10.1002/adma.201301658.

17. Cussler, E. L. *Diffusion: Mass Transfer in Fluid Systems*, 3 edition.; Cambridge University Press: Cambridge ; New York, 2009.

18. Poirier, D. R.; Geiger, G. H. Fick's Law and Diffusivity of Materials. In *Transport Phenomena in Materials Processing*; Poirier, D. R., Geiger, G. H., Eds.; Springer International Publishing: Cham, 2016; pp 419–461. https://doi.org/10.1007/978-3-319-48090-9_12.

19. Fick, D. A. V. On Liquid Diffusion. *The London, Edinburgh, and Dublin Philosophical Magazine and Journal of Science* **1855**, *10* (63), 30–39. https://doi.org/10.1080/14786445508641925.

20. Glass, N. R.; Tjeung, R.; Chan, P.; Yeo, L. Y.; Friend, J. R. Organosilane Deposition for Microfluidic Applications. *Biomicrofluidics* **2011**, *5* (3), 036501. https://doi.org/10.1063/1.3625605.

21. Brzoska, J. B.; Azouz, I. B.; Rondelez, F. Silanization of Solid Substrates: A Step Toward Reproducibility. *Langmuir* **1994**, *10* (11), 4367–4373. https://doi.org/10.1021/la00023a072.

22. Boccafoschi, F.; Fusaro, L.; Cannas, M. 15 - Immobilization of Peptides on Cardiovascular Stent. In *Functionalised Cardiovascular Stents*; Wall, J. G., Podbielska,

H., Wawrzyńska, M., Eds.; Woodhead Publishing, 2018; pp 305–318. https://doi.org/10.1016/B978-0-08-100496-8.00016-0.

23. Williams, R. A.; Blanch, H. W. Covalent Immobilization of Protein Monolayers for Biosensor Applications. *Biosensors and Bioelectronics* **1994**, *9* (2), 159–167. https://doi.org/10.1016/0956-5663(94)80108-8.

24. Möller, R.; Csáki, A.; Köhler, J. M.; Fritzsche, W. DNA Probes on Chip Surfaces Studied by Scanning Force Microscopy Using Specific Binding of Colloidal Gold. *Nucleic Acids Res* **2000**, *28* (20), e91–e91. https://doi.org/10.1093/nar/28.20.e91.

25. Chuah, Y. J.; Kuddannaya, S.; Lee, M. H. A.; Zhang, Y.; Kang, Y. The Effects of Poly(Dimethylsiloxane) Surface Silanization on the Mesenchymal Stem Cell Fate. *Biomater Sci* **2015**, *3* (2), 383–390. https://doi.org/10.1039/c4bm00268g.

26. Vinatier, C.; Magne, D.; Weiss, P.; Trojani, C.; Rochet, N.; Carle, G. F.; Vignes-Colombeix, C.; Chadjichristos, C.; Galera, P.; Daculsi, G.; et al. A Silanized Hydroxypropyl Methylcellulose Hydrogel for the Three-Dimensional Culture of Chondrocytes. *Biomaterials* **2005**, *26* (33), 6643–6651. https://doi.org/10.1016/j.biomaterials.2005.04.057.

27. Li, G.; Zhang, L.; Wang, C.; Zhao, X.; Zhu, C.; Zheng, Y.; Wang, Y.; Zhao, Y.; Yang, Y. Effect of Silanization on Chitosan Porous Scaffolds for Peripheral Nerve Regeneration. *Carbohydrate Polymers* **2014**, *101*, 718–726. https://doi.org/10.1016/j.carbpol.2013.09.064.

28. Ruckenstein, E.; Liu, H. Self-Diffusion in Gases and Liquids. *Ind. Eng. Chem. Res.* **1997**, *36* (9), 3927–3936. https://doi.org/10.1021/ie9701332.

29. Chen, Zhangxin.; Huan, Guanren.; Ma, Yuanle. *Computational Methods for Multiphase Flows in Porous Media*; Computational Science & Engineering; Society for Industrial and Applied Mathematics, 2006. https://doi.org/10.1137/1.9780898718942.

30. Bird, R. B.; Stewart, W. E.; Lightfoot, E. N. *Transport Phenomena, Revised 2nd Edition*, 2nd edition.; John Wiley & Sons, Inc.: New York, 2006.

31. Wu, J.; Mao, Z.; Tan, H.; Han, L.; Ren, T.; Gao, C. Gradient Biomaterials and Their Influences on Cell Migration. *Interface Focus* **2012**, *2* (3), 337–355. https://doi.org/10.1098/rsfs.2011.0124.

32. Keenan, T. M.; Folch, A. Biomolecular Gradients in Cell Culture Systems. *Lab Chip* **2008**, *8* (1). https://doi.org/10.1039/b711887b.

33. Sant, S.; Hancock, M. J.; Donnelly, J. P.; Iyer, D.; Khademhosseini, A. Biomimetic Gradient Hydrogels for Tissue Engineering. *The Canadian Journal of Chemical Engineering* **2010**, *88* (6), 899–911. https://doi.org/10.1002/cjce.20411.

34. Natarajan, A.; Chun, C.; Hickman, J. J.; Molnar, P. Growth and Electrophysiological Properties of Rat Embryonic Cardiomyocytes on Hydroxyl- and Carboxyl-Modified

Surfaces. *J Biomater Sci Polym Ed* **2008**, *19* (10), 1319–1331. https://doi.org/10.1163/156856208786052399.

35. Zargar, R.; Nourmohammadi, J.; Amoabediny, G. Preparation, Characterization, and Silanization of 3D Microporous PDMS Structure with Properly Sized Pores for Endothelial Cell Culture. *Biotechnology and Applied Biochemistry* **2016**, *63* (2), 190–199. https://doi.org/10.1002/bab.1371.

36. Alexa Fluor™ 594 NHS Ester (Succinimidyl Ester) http://www.thermofisher.com/order/catalog/product/A20004 (accessed Feb 2, 2020).

37. Lund, L. M.; Berman, A. S. Flow and Self-Diffusion of Gases in Capillaries. Part II. *Journal of Applied Physics* **1966**, *37* (6), 2496–2508. https://doi.org/10.1063/1.1708842.

38. Kruczek, B. Convective Transport. In *Encyclopedia of Membranes*; Drioli, E., Giorno, L., Eds.; Springer: Berlin, Heidelberg, 2015; pp 1–3. https://doi.org/10.1007/978-3-642-40872-4_1994-1.

CHAPTER 4: USING LIQUID LITHOGRAPHY TO CONTROL BIOMEDICAL STAMP MICROCURVATURE FOR IN VITRO CRYPT FORMATION

4.1. Introduction and background

4.1.1. Synthesis techniques for cell culture scaffolds in tissue engineering

Using current lithography techniques, micropatterns with well-controlled features can be created in both two and three dimensions. Photolithography is a microfabrication process with uses light to create precise structures in photo-reactive materials [1]. The method provides high resolution vertical features, such as microwells or fluid channels, but is limited in scope by the light pathways that can be used to pattern a template particularly for complex 3-dimensional features. Structures with a curvature in the Z dimension, occurring parallel to the light path, are generally difficult to construct without highly specialized equipment, expensive reagents, or extensive user experience, despite their potential in the re-creation of intricate features such as that to mimic tissue architecture [2]. Two-photon lithography [3], interference lithography [4], and grayscale lithography [5] are photolithography techniques used to shape 3D structures; however, these techniques often require sophisticated infrastructure. These and other challenges limit adoption and ultimately the breadth of microscale devices that can be fabricated using conventional lithographic workflows [6].

Other pattern strategies create curved features along a Z axis on the microscale. 3D printing is one such method, which involves using additive processing of materials to create three-dimensional objects from digital renderings. Today, 3D printers are cheaper and more readily available than ever before, and allow rapid prototyping (sometimes as quickly as same day). However, the more specialized materials needed for biological applications still have

challenges to overcome (namely structural integrity and limits in sample thickness) for widespread use, and available bio-inks are not suitable for all tissue systems [7]. Laser ablation is another potential method of creating features with curvature, but it can be difficult to create delicate features on soft biomaterials (as their structures may not remain intact when exposed to high energy densities), and curvature can only be made in one direction (away from the laser, convex curvature) [8]. Precise mechanical force can be used to remove exact amounts of polymeric material to create microfeatures, but this method is limited in its resolution. Additionally, the method can only create convex curvatures, as removing increasing amounts of material to create concave curvature in the other direction is not feasible, [9].

This study will explore an alternate synthetic method to create curved, 3-dimensional microfeatures by combining high-resolution (but simple) photolithographic templates with an additional lithographic technique, such as soft lithography. Soft lithography is a set of fabrication techniques which utilize a master template in combination with an elastomeric polymer such as polydimethylsiloxane (PDMS) to form a patterned mold or stamp to generate 3D structures. Methods such as capillary force lithography employ this strategy, though there can be difficulty in ensuring pattern uniformity, and the generated curvature can be difficult to control [10]. 3D structures can also be created directly in an elastic polymer via replica molding, involving liquid interfaces [11], air interfaces [12], or self-assembling objects like beads [13].

4.1.2. Liquid lithography

The technique of interest in this paper is termed “liquid lithography”, which combines elements of photolithography, surface tension interactions, and soft lithography, and is particularly adept at creating curved microsurfaces. Liquid lithography forces two immiscible liquids to interact within a base photolithography mold, forming a surface of controlled curvature

using the two liquid's interfacial tension [14]. Liquids with different relative surface tensions create predictable feature patterns when placed within a photolithographic template. The curved surfaces formed can range from relatively flat interfaces when liquids of similar surface energy are employed to extreme curvatures when liquids with very different surface energy are utilized. Liquid lithography has been explored in-depth, providing increasingly elaborate patterns from otherwise simple templates [15]. Using a template with relatively simple features, such as microwells (roughly 100-400 μm), the surface of a molding liquid (typically a polyol) introduced into the template forms a curved meniscus. A second immiscible or overlaying liquid such as PDMS is then added to the template and solidified to establish a curvature complimentary to the first or molding liquid. In this study, the goal was to extend the range of liquids utilized to support liquid lithography as well as to develop a strategy to form a gradient in the curvature of formed structures. Such a method would have wide-spread application for understanding cellular physiology wherein physical structure plays a critical role in tissue function. Examples of curved features thought to have important physiologic roles include colonic crypts with stem cells located at a region of high curvature [16] and the highly curved lung alveoli responsible for oxygen exchange [17]. To properly model the architectural microenvironment on these cells, the ability to replicate their curved supporting surfaces or features is of critical importance.

4.1.3. Establishing a link between microcurvature of a scaffold and colonic cell culture

Prior investigators have demonstrated that substrate microcurvature can modulate mechanotransduction between the ECM and cells [18]. The geometry of the cell culture surface has also been linked to the expression of various cytoskeletal proteins (such as YAP1 and F-actin) [19,20]. Colonic cell culture is of particularly interest in this study, as the colonic crypt base is comprised of a highly curved surface which supports stem cells. These crypts are

embedded in the epithelial wall of the intestinal tract, and are responsible for nutrient uptake, host defense, and hormonal signaling. Significantly, these crypts demonstrate cell compartmentalization with stem cells in the basal compartment and differentiated cells closer to the luminal side of the crypt [21]. Chemically, a number of factors influence this natural polarization, including gradients of compounds like Wnt, Rspondin, and Noggin from the base of the crypt to the lumen [23]. At this point, however, detailed studies have not yet been conducted on the link between any physical/structural gradients within the crypt and their resulting effects on colon cell behavior.

In this work, the ability to control curvature using a range of different polyols combined with chemical surface modification was assessed. The ability of gradients in surface chemical properties to form microfeatures with gradients in their surface curvature across a device was evaluated and optimized. These gradients in chemical surface properties were demonstrated following optimization of a vapor diffusion process within a constricted microchannel. To demonstrate the utility of the method, human primary colonic stem cells were cultured within microwells with varying curvature at the microwell base. The impact of the concave to convex curvatures on cell proliferation and cytoskeletal behaviors was assessed.

4.2. Materials and methods

4.2.1. Photolithographic microwell template creation

Photolithographic materials were prepared in-house. SU-8 100 photoresist was developed by mixing 73% by weight SU-8 resin with 22% by weight gamma-butyrolactone (GBL) and 5% by weight triarylsufonium hexafluoroantimonate (TSH). The adhesive base layer photoresist for templates was 1002F-10; 49% by weight 1002F resin, 46.1% GBL, and 4.9% TSH [24]. A clean glass slide was initially treated with oxygen plasma for 5 min. After this, an adhesive layer of

1002F-10, 5-10 µm thick, was applied to the slide, which was then exposed to 1 J of UV light (350 nm wavelength) and then baked for 20 h at 120°C. The slides were then spincoated with SU-8 100 to desired thicknesses (100 to 350 µm), baked (95°C) for 2 h, and exposed to 0.4 J of UV light while covered with a photomask. Two photomasks (Front Range Photomask, Lake Havasu City, AZ) were used in this study, each fabricated using low reflective chrome on a glass base. These masks were created with 5 µm of resolution, with the first mask containing arrays of 70 µm-diameter circles, and the second mask containing arrays of 120 µm-diameter circles. These circles were separated center-to-center by 100 µm and 150 µm, respectively. The array of circles was 30 × 30 mm in both cases. After exposure and a 2 h post-exposure bake at 95°C, these slides were developed in 1-methoxy 2-propyl acetate at 25°C for 10 min, and then left for 16 h at 120°C in order to fully cure.

4.2.2. Silanization of photolithographic microwell templates

Using a polycarbonate desiccator (Fisher Scientific, 08-642-7), the photoresist templates were placed with microfeatures facing up on a level surface within the desiccator. Varying volumes of trichloro(octyl)silane, 50 µL-250 µL in 50 µL increments, were added in liquid form to a small petri dish within the chamber and the liquid was left uncovered. The chamber was placed under a 95 kPa vacuum for 5 min to vaporize the silane and incubated for 16 h. When gradients of silane were formed across the surface of the microwell template, the template was covered with a rectangular polymer chamber with one opening, to limit silane access to the surface of the template. The cavity surrounding the template was 30 mm in width, 30 mm in length, and varied in height from 1 mm to 4 mm. The cavity encased the microfeatures of the template, creating a secondary diffusion chamber within the desiccator.

4.2.3. Sacrificial liquid deposition and PDMS molding for liquid lithography

All sacrificial liquids were prepared in-house in aqueous solutions. The following polyol solutions were prepared in 50 mL volumes with deionized (DI) water: tetraethylene glycol (40% by weight, Sigma Aldrich, 110175); xylitol (40%, Sigma Aldrich, X3375); glycerol (40%, Sigma Aldrich, G9012); ribose (40%, Sigma Aldrich, R7500); dipropylene glycol (50%, Sigma Aldrich, D215554); sorbitol (30%, Sigma Aldrich, 240850); trimethyolethane (15%, Fisher Scientific, T047925G).

Template features were covered with these aqueous polyol solutions until all features were fully submerged. The template/solution were then placed under vacuum 5 times for 30 s each to remove excess gas from inside the microwells and ensure full liquid penetration into the microwells. The template was tilted to 45° and discontinuously dewetted with the remaining sacrificial liquid to remove excess solution from the surface, and then placed in a 70°C oven for 20 min to solidify the sacrificial liquid left within the features. PDMS pre-polymer (SYLGARD 184 Silicone Elastomer Base) and PDMS curing agent (SYLGARD 184 Elastomer Curing Agent) were combined in a 5:1 ratio for a total of 10 mL and stirred vigorously. This PDMS solution was then coated onto the microfeatures of the template, degassed for 2 min, and cured at 95°C for 1 h. After baking, the PDMS was readily removed from the template and placed with micropillar stamps facing upward on a standard glass slide.

4.2.4. DIC and ESEM imaging of generated micropillar stamps

For micropillar stamps with convex curvature, differential interference contrast (DIC) microscopy was sufficient to measure pillar curvature. Thin slices of the array of pillars were collected with a razor blade and placed flat, with pillars lying horizontally, on a glass slide. These pillars were imaged at 10x and 20x magnification on a Nikon Eclipse TE2000-U DIC

microscope. High resolution images of the pillars (both concave and convex) were collected using environmental scanning electron microscopy (ESEM). ESEM images were collected on a FEI Quanta 200 Field Emission Gun, following sputtercoating with 4 nm of platinum.

4.2.5. Confocal microscopy imaging of concave-tipped micropillar stamps

Micropillar stamps with concave tip curvature were incubated in 0.2% rhodamine B in 1X PBS for 16 h. These stamps were then dried and rinsed with 70% ethanol in DI water. The pillars were then imaged via confocal microscopy on an Olympus IX83 Research Inverted Microscope, generating Z-stack images.

4.2.6. Intestinal epithelial cell culture

Cells used in this study originated from biopsies of human colonic epitheliums, acquired from colonoscopies at the University of North Carolina's Hospital Meadowmont Endoscopy Center with consent of the patient (under the approved University of North Carolina Institutional Review Board #14-2013). Crypts were isolated and the cells culture as described previously and then frozen for later use [21]. All experiments in this study were conducted using cells between passage 5 and 10 (P5 and P10). Cells demonstrated a normal karyotype through P11 [21]. Just prior to use, cells were expanded on collagen scaffold as described previously [21]. The media compositions used in this study were described previously [21] and are termed expansion media [EM], stem media [SM], and differentiation media [DM]. The composition of these medias can be found in Wang et al [21]. Briefly, EM is used to grow cells after initial seeding. SM is used to promote the expansion of stem and proliferative cells, while DM is used to differentiate cells into colonocytes, goblet cells and other differentiated colonic epithelial cells. These two media types (SM and DM) can be used in concert to create gradients of differentiation on a prepared scaffold, as will be described in Section 4.2.7.

4.2.7. Formation of *in vitro* colonic crypts

In vitro crypts were formed as previously described [21]. For this application, crypt-shaped microwells were molded into a collagen scaffold using pillar molds constructed using liquid lithography and possessing concave, flat or convex curved bottoms at each microwell or crypt. Briefly customized 12-well Transwell inserts were formed by replacing their polycarbonate porous membrane with a PTFE membrane ((BGCM00010; Millipore, Burlington, MA). A diffusion window in the membrane was formed by placing a 3 mm hole in a nonpermeable olefin plastic film (4-mL thick, TOPAS 6013; TOPAS Advanced Polymers, Florence, KY) attached to the bottom of the PTFE membrane.

A solution of Type I rat-tail collagen (5 mg/mL), 1-ethyl-3-(-3-dimethylaminopropyl) carbodiimide hydrochloride (EDC, 600 mmol/L) and N-hydroxysuccinimide (NHS, 150 mmol/L) were loaded into the upper reservoir of each Transwell insert and then molded by pressing the PDMS micropillar stamps into the collagen as it cross-linked. The micropillar stamp was removed from the shaped collagen which was washed as described previously [21]. The collagen microwell array (*in vitro* crypt scaffold) was then coated with 10 µg/mL Type I human collagen at 37°C for 16 h and then rinsed 2x with sterile 1X PBS. As described previously [21] cells were cultured on the upper surface of the shaped collagen scaffold until the cells formed a monolayer across the surface and lining the microwells. When 80% cell confluency was reached, a chemical gradient was formed along the crypt long axis by SM (2 mL) into the basal reservoir and DM (1 mL) into the luminal reservoir. These media were changed daily for 5-7 days and then the cells assayed as described below.

4.2.8. Staining and fluorescence measurements

Prior to cell fixation, cells were incubated with 5-ethynyl-2´-deoxyuridine (EdU) at 10 µmol/L in 1X PBS for 24 h at 37°C. Cells were then fixed using 4% paraformaldehyde (PFA) in deionized water by incubation for 20 min at 25°C. The cells were rinsed 2 times with 1X PBS. After fixing, cells were permeabilized using 0.5% Triton X-100 in 1X PBS for 20 min at 25°C. DNA was labelled by incubation with 2 µg/mL Hoechst 33342 in 1X PBS for 15 min at 25°C. Incorporated EdU incorporation was labelled using the Alexa Fluor 647 EdU Click-IT stain (C10430, Thermo Fisher Scientific). F-actin was stained using the ActinGreen 488 ReadyProbes kit (R37110, Thermo Fisher Scientific), a phallotoxin stain that specifically binds F-actin. G-actin, the non-polymerized globular form of actin, was stained using deoxyribonuclease I, conjugated with Alexa Fluor 594 (10 µg/mL in 1X PBS; D12372, Thermo Fisher Scientific). Fixed cells were stained for F-actin and G-actin by incubation with the dyes at 30 min at 25°C. After staining, the cells were imaged using confocal microscopy (Olympus IX83 Research Inverted Microscope). Z slices every 2.5 µm along the crypt long axis was collected. The average fluorescence intensity for each fluorescent stain at each image slice was quantified using ImageJ plugin Time Series Analyzer V2 [25]. For Z-section analysis, the image slices from each crypt were organized into 25 µm bins at the bottom, middle, and top of each crypt. The average fluorescence intensity (in relative fluorescence units, or RFU) of these bins was measured, and then compared across 20 crypts for each type of crypt to account for crypt-to-crypt variability. These images were collected at the same laser intensity and voltage to enable comparison.

4.2.9. Statistics

The primary statistical analysis used in this study was a two-tailed t-test P-value analysis, with confidence levels of 99% ($p < .01$) used to indicate a statistically significant difference in

population average. All collected data was assessed for the presence of a normal distribution prior to comparison.

4.3. Results and discussion

4.3.1. Overview of array fabrication and application

Liquid lithography using a polyol loaded into a chemically modified microwell array was used to fabricate a PDMS stamp with an array of micropillars with tips of varying curvature (Fig. 1). The micropillar stamps were then used to form collagen scaffolds consisting of an array of microwells with bases of varying curvature. Finally, *in vitro* crypt arrays were formed by culture of a monolayer of primary, human colonic epithelial cells across the array surface and the impact of crypt base curvature on cell physiology was investigated.

4.3.2. Selection of the molding liquids to form a micropillar stamp with tip surfaces of varying convex curvatures

Initial stages of liquid lithography rely upon a suitable mold and liquid selection in order to establish a surface tension difference that shapes the liquid into the desired curvature. In this case, polyols were chosen as the molding liquids due to their abundance, low cost, and spectrum of suitable surface energies (ranging from 35.0 dynes/cm to nearly 120.0 dynes/cm). Polyol surface energy is primarily tied to the number of hydroxyl groups bonded along the hydrocarbon backbone of each polyol monomer (Table 1). As the number of hydroxyl groups increases, a polyol monomer exhibits higher surface energies, preferring to self-bond rather than spreading across a surface [26]. This property has the potential to yield a range of curvatures based on the selected polyol molding liquid. In order to establish a direct link between pillar curvature and the surface energy of a molding liquid, polyols with varying hydroxyl number (2-6) were chosen to assess their impact on curvature during liquid lithography. The choices were as follows:

dipropylene glycol, tetraethylene glycol, trimethyolethane, glycerol, D-ribose, xylitol, and sorbitol. It was hypothesized that below the SU-8 surface energy, the molding liquid would display wetting behavior, and resultant pillars would have a convex shape, and above this threshold, a molding liquid would display non-wetting behavior, and resultant pillars would have a concave shape.

Three molding liquids with low surface energies were initially chosen with a goal to produce convex-tipped micropillar stamps. The curvature of the micropillar stamps formed from the low-energy polyols was measured by microscopy (Fig 2a). Use of TMOE yielded significantly flatter surfaces than use of TEG and DPG. TEG and DPG yielded similar curvatures due to their equivalent number of hydroxyl groups. Initially, TMOE was predicted to yield concave-tipped pillars as its surface energy is reported to be greater than that of SU-8 [15]. However, in practice, convex-tipped pillars were observed when using TMOE as a molding liquid. It is likely that SU-8 surfaces possess varying surface energies depending on the fabrication steps and that the SU-8 used had a greater surface energy than that typically reported in the literature. In some experiments, the height of the generated micropillars (124±33 μm) varied. This was likely due to the de-wetting strategy used, resulting in a varying amount of residual liquid per well. We anticipate that an automated pipetting system for liquid deposition would eliminate this variability.

4.3.3. Chemical modification of a microwell mold to form a micropillar stamp with tip surfaces of varying convex curvatures

Without chemical modification, most photolithographic substrates like SU-8 have relatively low surface energies compared to most solutions used in liquid lithography [30]. However, it is possible to modify the surface energy of the SU-8 substrate to affect the initial

interfacial interaction between the molding liquid and the template. Deposition of a hydrophobic organosilane (octyltrichlorosilane) was used to lower the surface tension of an SU-8 mold, decreasing its wettability and enabling a wider range of molding liquids/polyols to display non-wetting behavior [35]. Octyltrichlorosilane in varying volumes was deposited within a chamber and vapor-phase deposition onto an array of SU-8 microwells performed. As the silane volume was increased, the curvature of pillars generated from TEG, DPG, or TMOE decreased (Fig 2b-g). When imaged by microscopy the decrease in curvature was readily apparent (Fig. 2b-e). When imaged by SEM, the pillars possessed high-quality, smooth surfaces (Fig 2g). Based on the results of this experimental workflow, it was determined that vaporous silane deposition could be employed to alter micropillar tip curvature in a predictable manner.

4.3.4. Selection of the molding liquids and silane-modified wells to form a micropillar stamp with top surfaces of varying concave curvatures

Micropillar stamps in which the top surface is concave could be used as a stamp to form an array of microwells in which the bottoms were convex, forming a "bubble" pushing into the interior cylinder of the microwell. Such microwells would be of significant value in understand cell-cell proximity effects such as between nurse and stem cells or in guiding cell differentiation/migration [36]. Molding liquid polyols with 3 or more hydroxyl groups (and surface energies greater than roughly 55-60 dynes/cm) were expected to poorly wet the SU-8 microwell templates and hence form a sphere of liquid at the bottom of the SU-8 microwell molds (Table 1). Liquid lithography would then produce PDMS micropillar stamps in which the top surface of each pillar was concave. A lithographic microwell template was placed in a vacuum chamber and exposed to varying volumes of octyltrichlorosilane. PDMS micropillar stamps were formed using polyols with 3-5 hydroxyls. The formed micropillars demonstrated

concave upper surfaces when sectioned and imaged by transmitted light, when stained with rhodamine B and imaged by confocal microscopy, or imaged by SEM (Fig 3a,b,d). All 3 sacrificial liquids displayed an inverse relationship between micropillar surface curvature and the volume of silane used (Fig 3c). The difference in micropillar curvature was statistically different for the pillars fabricated using 0 and 200 µL of silane. These data demonstrated that polyol sacrificial liquids of a sufficiently high surface energy generated concave-tipped micropillars and increasing silane volume led to greater absolute surface curvatures. Additionally, as the number of hydroxyl groups in the polyol sacrificial liquid increased the absolute curvature increased. While the above data demonstrated the ability to form microwells with both concave and convex surfaces, each surface curvature required a separate fabrication step. The ability to produce a single array of microwells in which the microwells varied in the curvature of their base would speed the ability to assess the role of surface curvature in future experiments.

4.3.5. Establishing a gradient of convex curvature across an array of micropillar stamps

One of the promises of lab-on-a-chip platforms is the ability to screen rapidly through many different assay variables. To achieve a gradient of surface energy along the SU-8 microwell array, a diffusion chamber (30 mm wide, 30 mm long, 1 - 4 mm high) was constructed to house the mold during the silane reaction (Fig 4a). When the chamber was mated with the microwell array mold, the mold was accessible to the external atmosphere or vapor phase silane through a single open side. Thus, the mold end closest to the opening was expected to experience a higher concentration of the vapor-phase silane relative to the edge of the mold farthest from the open end. The gradient in the silane concentration was modulated by altering the secondary chamber height, diffusion time, and silane volume within the chamber. A micropillar stamp was then formed from this mold using a polyol sacrificial liquid (TEG, DPG, or TMOE). The stamp

was sliced into 1 mm-thick sections that were 4, 8, 12 and 16 mm from the array end and the slices examined by microscopy. As the slices increased in distance from the open end of the chamber, the curvature of the micropillar tops decreased (Fig. 4b-h). For example, when TEG was used as the sacrificial liquid, the top of the micropillars were significantly different in curvature between 4 and 16 mm at 12.6±4.1 degrees and 37.4±3.7 degrees, respectively (Fig 4b-e). Overall, these results suggested that greater silane deposition occurred at the edge of the mold closest to the chamber opening relative to that at the back end and that a gradient of surface energy was created enabling a gradient in micropillar surface curvature across the array.

To understand how the height of the chamber impacted deposition of the silane, diffusion chambers with a height of 1, 2, or 4 mm were used for silane deposition. TEG, DPG, or TMOE were then added to the microwells on the array and PDMS micropillar stamps formed. When a 1 mm height was used, the micropillar stamps displayed a greater tip curvature relative to that formed with a 2 mm-high chamber (Fig 4f-h), suggesting that silane did not penetrate as deeply into the diffusion chamber during the diffusion time. When a 4 mm-high chamber was used, the micropillar stamps using TEG, DPG, and TMOE displayed lower magnitudes of tip curvature relative to the stamps formed from a 2 mm chamber (Fig 4f-h), suggesting that silane penetrated deeply into these very tall diffusion chamber. Thus, the 2 mm height chamber yielded the greatest range of curvatures for the micropillar surfaces across the array. This data demonstrated that a gradient of device surface properties was formed *via* simple, vapor-based silane diffusion, and the ensuing surface energy gradient enables formation of micro-objects of distinct curvature.

4.3.6. Establishing a gradient of concave curvature across an array of micropillar stamps

Biological architectures feature both concave and convex surfaces; for example, branching within the bronchiole of the lungs leads to concave curvature and cell isolation at the

start of different branches [38], and asymmetric budding of crypts can be observed during crypt formation, also yielding concave curvature [39]. Therefore, it is important to be able to replicate concave curvature (in addition to convex) in a lab-on-a-chip setting with varying degrees of magnitude. To create structures of concave curvature, diffusion chambers of heights 1, 2, or 4 mm were placed over a microwell array which was then silanized with octyltrichlorosilane. After which time, glycerol, ribose, or xylitol was loaded into the wells and a PDMS micropillar stamp then formed. For 4 mm chamber heights, there was no statistically significant change in pillar tip curvature across the length of the array for any of the tested polyol sacrificial liquids (Fig 5). This was likely due to silane saturation throughout the chamber over the 16 h diffusion window. However, both 1 mm and 2 mm chamber heights led to a statistically significant difference in tip curvature when moving from the opening to the closed end of the secondary chamber for the tested sacrificial liquids (Fig. 5). Overall, the observed gradients in curvature support our initial hypotheses, as increasing the chamber height of the secondary chamber provoked an inverse relationship in the sharpness of the observed surface tension (and tip-curvature) gradient.

4.3.7. Analyzing biomedical pillar curvature effects on *in vitro* colonic stem cell activity

To understand the impact of curvature on the colon crypt stem cell niche, primary human colon epithelial cells were cultured within collagen microwells formed with varying curvature at their base: -30, 0 or 30 degrees of curvature. The collagen microwells were formed using PDMS of varying curvature fabricated using liquid lithography with different polyols. As described previously, when primary colonic epithelial cells are cultured to confluence on the shaped collagen followed by application of a chemical gradient, polarized *in vitro* crypts form with a distinct stem cell and differentiated cell compartment [21]. *In vitro* crypts with altered stem compartment curvatures, created from concave, flat, and convex micropillar stamps, were stained

for DNA (Hoechst 33342) and S-phase cells (EdU incorporation), fixed and imaged by confocal microscopy (Fig 6a-c). As expected, proliferative cell density at the top and through the middle of the crypts was similar for convex, flat and concave-bottomed crypts, as there should be no curvature differences at these points along the microwell or *in vitro* crypts (Fig 6d-e). In contrast, a significant increase in cell proliferation was observed at the base of the concave-bottomed crypts relative to that at the base of the flat or convex-bottomed crypts.

In order to further quantify the difference in EdU intensity between crypt styles and different areas along the crypt, additional staining image analysis was performed (Fig 6e). Briefly, for each crypt, Z-stack image slices were collected every 2 μm along the crypt. In order to look at EdU intensity for the different sections of the crypt (luminal, middle, and basal), "bins" of Z-stack slices were created and stacked together in ~25 μm increments. The top 25 μm was labeled as the luminal section, a grouping of 25 μm around the middle of the crypt was labeled the middle section, and the bottom 25 μm was labeled as the basal section. 25 μm was chosen in order to fully capture the curved surfaces in the stem compartment of each crypt. There was no statistically significant difference (with 99% confidence) in average EdU intensity between any of the crypt styles in the luminal or middle compartments of the crypt.

In the basal compartment, however, all 3 styles of crypt (made from concave, flat, and convex pillars) were statistically significantly different from each other with 99% confidence. Crypts made from concave pillars displayed an average EdU intensity of 6.1e5±2.7e5 RFU, crypts made from flat pillars displayed a basal EdU intensity of 1.4e6±2.1e5 RFU, and crypts made from concave pillars displayed the highest basal EdU intensity at 2.3e6±3.7e5 RFU. This data supports the hypothesis that changing the microcurvature of the stem cell compartment of a crypt can alter proliferative cell activity, and that using pillars of concave curvature caused a

noticeable increase in proliferative cell activity. Because of these results, researchers in this study were interested in other potential effects on cell behavior that altering the stem cell compartment curvature could cause. It was decided to focus on cell activity revolving around cell-cytoskeleton interactions, and the involved proteins, as altering microcurvature could feasibly cause downstream effects on mechanotransduction at the bottom of *in vitro* crypts.

4.3.8. Establishing connections between pillar curvature effects and cytoskeletal adjustments for colonic epithelial cells

The downstream behavior effects of changing the physical microenvironment of the crypt stem cell compartment likely originate with changes in how the cells interact with the extracellular matrix (ECM). Cytoskeletal proteins, such as actin, tubulin, and laminin, are likely secreted in different amounts as a response to the different mechanostimuli a cell experiences on structures of different curvature. While likely far more pronounced on scaffolds with pronounced, curved nanofeatures (due to closer dimensions in magnitude to mechanosensors on the cell/ECM), researchers in this study hypothesized that concave, flat, and convex *in vitro* crypts would generate different cytoskeletal protein responses in colonic epithelial cells. Colonic epithelial cells were cultured and grown into *in vitro* crypts exactly as described in the previous section. The difference for this section came in the immunofluorescence stage of experimentation, and is outlined in Section 4.2.7. F-actin and G-actin were chosen as targets of interest because of the important role they play in cell-cell interactions on the microscale. It was thought that, by altering the microstructure of the stem cell compartment within the *in vitro* crypts, mechanotransduction within these crypts would be altered as well, and cytoskeletal stains are a viable way of measuring those changes downstream (Figs 7 and 8). The bottom 25 μm of a set of *in vitro* microwell crypts were created from each type of micropillar stamp and stained for

Hoechst 33342 (blue), F-actin (yellow), and G-actin (red), as well as a composite image for each type (Fig 7). These 25 μm stacks were created via confocal Z-slice imaging, and the bottom 25 μm were chosen in order to cover the full curvature of the stem cell compartment. Qualitatively, it can be observed that general nuclear count and F-actin presence are similar regardless of the type of pillar used to create the crypt. However, when stained for G-actin, there is a distinct difference based on pillar type. Specifically, G-actin seems to be more heavily expressed in crypts created by concave pillars.

Quantitative analysis of these crypts after cytoskeletal staining was also performed (Fig. 8), showing Hoechst, F-actin, and G-actin stains (Fig 8a-c, respectively). Each graph is separated into three compartments, each 25 μm long and containing Z-stack fluorescence intensity images for each stain. Crypts created using each style of pillar without any seeded cells were also stained and used as a control group; staining results for flat-bottomed crypts without cells were included to show a baseline level of fluorescence (Fig 8). Firstly, it was important to establish similar that the intensity of Hoechst fluorescence was similar between each type of crypt in the luminal and middle sections of each crypt, as stem compartment curvature should not have a major effect on cell number in those parts of the crypt. This was found to be true in this study, as there was no statistically significant difference in Hoechst intensity (and therefore, cell number) between the different crypt curvatures at any location along the crypts. For F-actin, there was no difference in fluorescence intensity in the luminal or middle sections of the crypt, as expected. In the basal stem cell compartment, crypts created from convex and flat pillars had no statistical difference. However, both had statistically significantly higher F-actin presence than crypts created from concave pillars. This gives evidence that there are cytoskeletal differences caused by the concave pillars that were not observed for the other pillar curvatures; it is feasible that cells are less able

to connect to each over via cell-cell interactions because of the physical strain caused by the upward-curving stem compartment in these crypts. The major difference in cytoskeletal activity, however, can be found in G-actin activity in the stem compartments of the crypts (Fig 8c). While convex and flat pillars generate similar levels of G-actin activity, concave pillars generate an extremely significant increase in G-actin fluorescence in the stem compartment. One hypothesis for this substantial increase in G-actin activity could be that cells in the crypts created by concave pillars are receiving mechanostimuli to increase production of actin, to create more cell-cell interactions, but the microcurvature within the crypt prevents full polymerization of G-actin into F-actin. This could lead to overexpression of G-actin, which would fit with the data collected in this experiment. While there could be other explanations, these experiments give significant evidence that microcurvature within the stem cell compartment of a colon crypt can have major downstream effects on cell behavior.

4.4. Conclusions and acknowledgments

In summary, this group of experiments give evidence that adjusting the physical microenvironment within *in vitro* crypts of colonic epithelial cells can have major effects on subsequent cell behavior. It is possible to control the curvature at the tips of biomedical micropillars by use of liquid lithography as a synthesis method. Specifically, by using A) different polyol molding liquids to exploit surface tension interactions within lithographic microwells, and B) using vaporous deposition of silane to mute these surface tension effects in a controlled manner. It was also demonstrated that it’s possible to create a gradient of micropillar tip curvatures on the same lithographic template by using an applied gradient of vaporous silane deposition. These methods combined allowed for PDMS stamps to be created for use with type I

collagen bioscaffolds, and these bioscaffolds could then be used to culture intestinal epithelial cells.

By using these modified PDMS stamps, it was observed that an altered curvature from the micropillar tips would have substantial effects on cell behavior within the basal stem cell compartment of the generated *in vitro* crypts. When pillars of convex curvature were used, it was found that proliferative activity in the base of the crypts was elevated relative to the other tip curvatures; this is possibly due to the cells being more tightly grouped at the base of the crypt. Similarly, it was found tip curvature had effects on cytoskeletal activity in affected areas of the crypt, with concave pillars leading to a significant elevation in G-actin presence compared to the other types of pillars. This work gives a new approach for more closely mimicking *in vivo* cell behavior in lab-on-a-chip/bioscaffold *in vitro* work, just by altering the physical environment on which cells are cultured. For any tissue type that relies upon cytoskeletal structure and mechanotransduction for behavioral cues, these findings could give a new avenue of study for reducing the gap between *in vivo* and *in vitro* cell behavior.

The author thanks Nicole Smiddy and Matthew Disalvo for assistance and training in photolithographic techniques, and thanks Scott Magness for providing human colonic epithelial tissue. The author also thanks the Chapel Hill Analytical and Nanofabrication Laboratory for assistance in microscopy. Finally, the author thanks NSF GRFP Grant # 2016212411 and NIH DK109559 for funding.

4.5. Figures

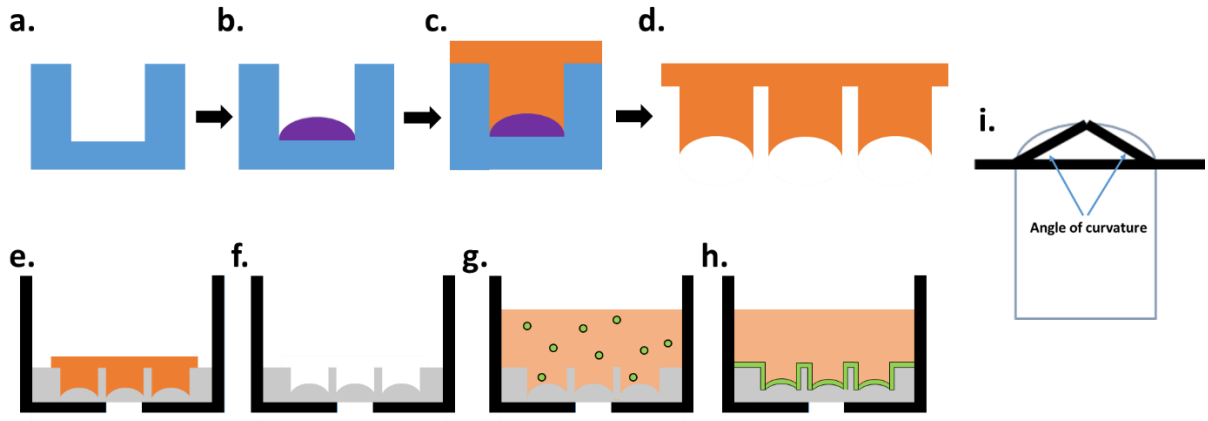

Figure 4.1. Schematic of liquid lithography and *in vitro* crypt synthesis with biomedical micropillar stamps. Schematic of general experimental workflow in this project. a) Cylindrical microwell masters are created from SU-8 (blue) via photolithography. b) Sacrificial aqueous polyol solutions (purple) are deposited within the microwell masters and solidified. c) PDMS (orange) is added onto the surface of the microwell master with polyol. d) The cured PDMS stamp is removed from the SU-8 microwell master. This example shows concave micropillars. e) The PDMS pillar stamp is pressed into a liquid solution of type I rat-tail collagen (grey) within a Transwell cassette (black), which is then gelled and cross-linked. f) The PDMS stamp is carefully removed from the molded collagen leaving an array of crypt microwells in the collagen scaffold. This example shows microwells with a convex bottom. g) A media solution (light orange) containing colonic epithelial cells (green) is cultured on the scaffold. h) The colonic cells grow to confluence. i) The tips of generated pillars were measured by establishing a parallel plane with the flat "bottom" of the pillar. After this, researchers measured two angles from that plane, coming from the left- and rightmost parts of the pillar, to the actual maximum tip of the pillar. These two values were averaged, and any pillar displaying a difference of 5 or more degrees between the angle was not used for measurement.

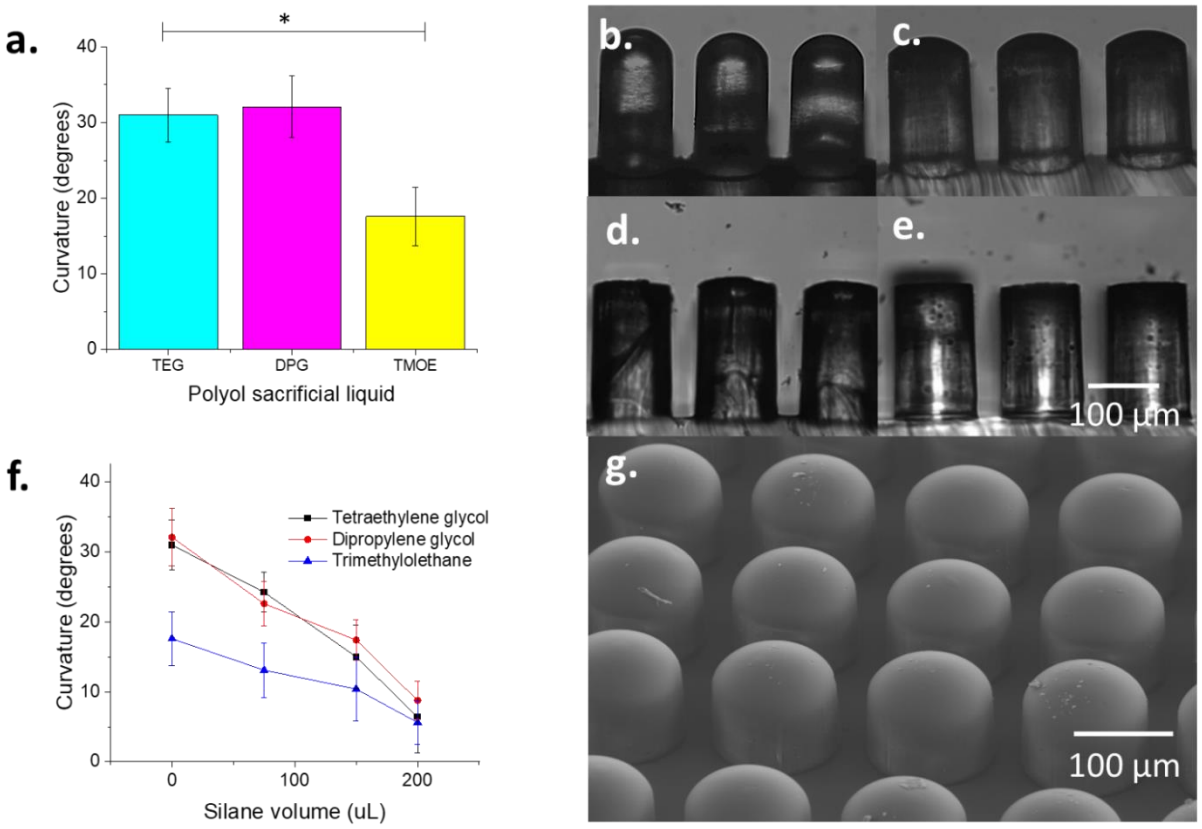

Figure 2. Creation of convex-tipped micropillar stamps. a) Micropillar stamp curvature in the absence of silanization (* = $p < 0.001$). b-e) Microscopy images of micropillar stamps created using varying volumes of octyltrichlorosilane, with 0 (b), 75 (c), 150 (d), and 200 (e) µL. f) The dependence of micropillar stamp curvature on the volume of silane employed for each of 3 polyols. g) SEM of convex micropillar stamps.

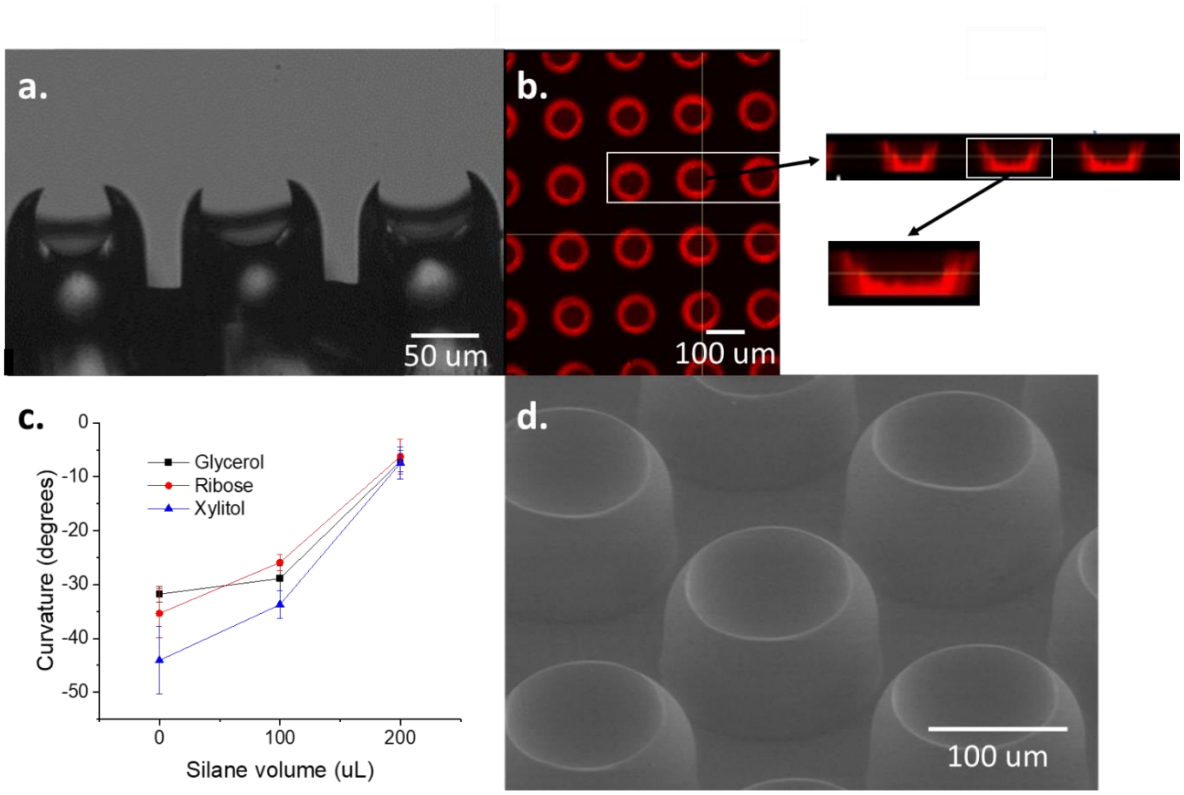

Figure 3. Creation of concave-tipped micropillar stamps. a) Microscopy image through a section of an array of concave-tipped pillars, created using sorbitol as a polyol sacrificial liquid. b) Fluorescence confocal image (XY plane) through an array of concave micropillar stamps stained with rhodamine B. Expanded insets are Z-stack images of three and one micropillar(s). c) Dependence of micropillar stamp curvature on silane volume. d) SEM image of concave micropillar stamps.

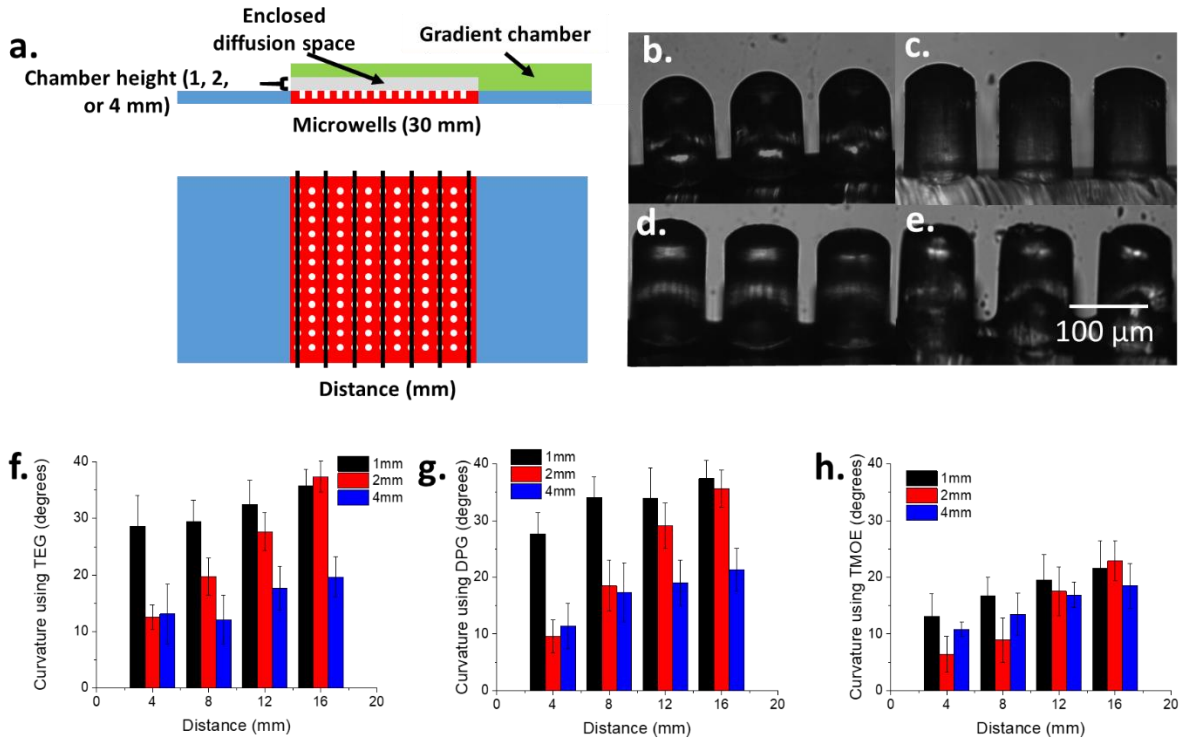

Figure 4.4. Creation and measurement of a gradient of convex micropillar tip curvature. a) An illustration of the secondary diffusion chamber used to create gradient diffusion of silane. The isolation chamber was placed so that only one end of the square array of wells was open to silane diffusion, with the other 3 sides closed off by a thick plastic isolation chamber. Height of this chamber could be altered by 3D printing additional isolation chambers. b-e) DIC images of pillars generated on one template using a 2 mm height secondary chamber within a silane diffusion chamber, moving from 4 mm away from the back end of the chamber (away from the opening) for (b), 8 mm away for (c), 12 mm away for (d), and 16 mm away (near the chamber opening) for (e). Silane deposition increased from b-e, resulting in a decrease in tip curvature. f-h) The quantitative relationship between convex-tipped pillar curvature and distance from the back end of the chamber, with 4 mm being near the closed end of the chamber and 16 mm being near the opening of the chamber.

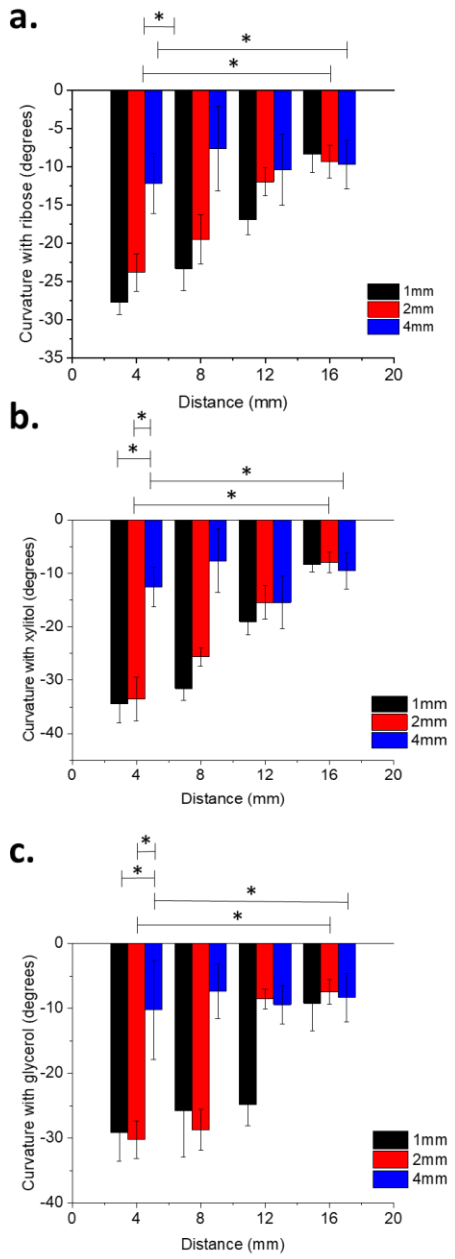

Figure 4.5. Creation and measurement of a gradient of concave micropillar tip curvature.

a-c) The quantitative relationship between concave-tipped pillar curvature and distance from the back end of the chamber, with 4 mm being near the closed end of the chamber and 16 mm being near the opening of the chamber. Negative values of degrees were used in this figure to illustrate

the difference between concave and convex curvature, with negative angles corresponding to concave curvature on the pillar tip. * denotes statistical significance at 99% confidence.

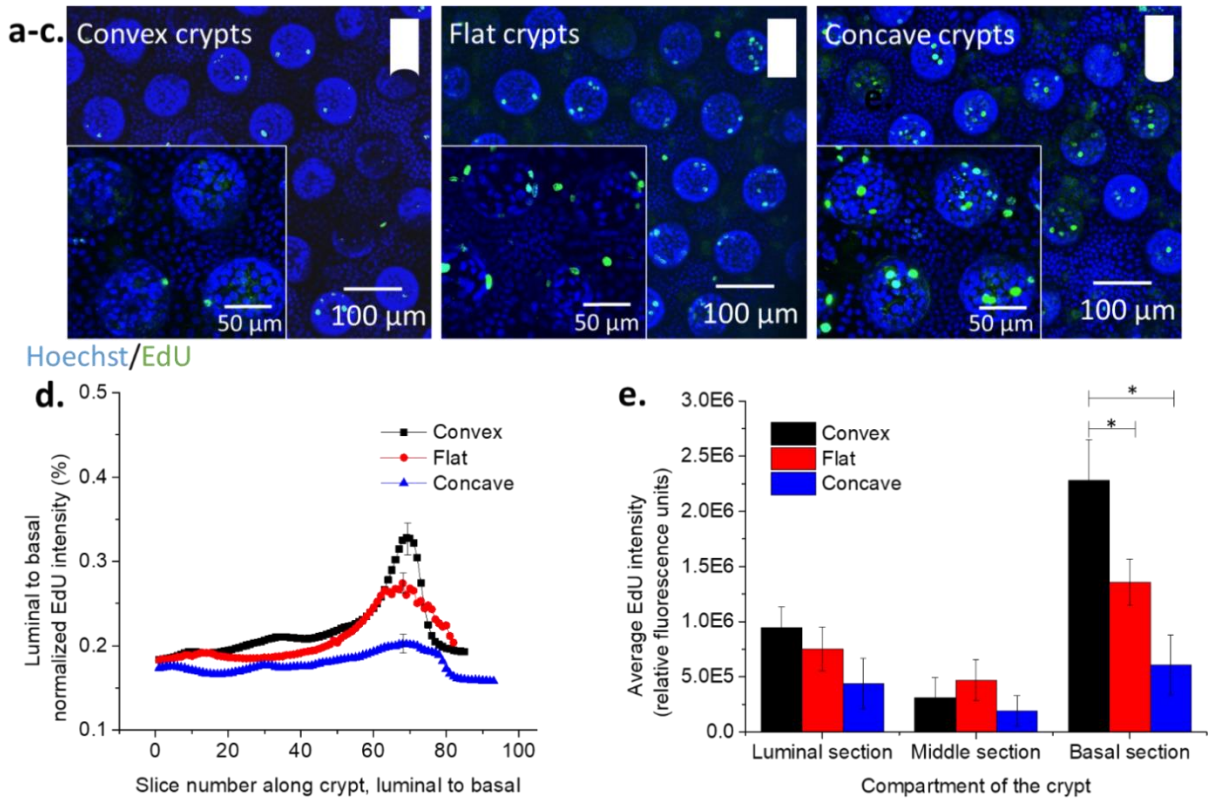

Figure 4.6. Measuring the effects of microcurvature in the *in vitro* crypt stem cell niche on proliferative activity. a-c) Confocal Z-stack images of in vitro crypts created with different PDMS stamp curvatures. Hoechst is shown in blue, EdU staining is shown in green. These images were all taken at identical laser intensity and voltage to allow for comparison. The entirety of each crypt is stacked and shown in these images. d) Using ImageJ, each Z-slice image (occurring approximately every 2.5 µm) for 25 crypts per pillar type was measured for Hoechst and EdU intensity, giving a map of fluorescence along the entirety of the crypt. The EdU intensity then normalized to Hoechst intensity, to account for cell number variability. Standard deviations are shown for the peak intensity value of each crypt type. e) Each crypt was divided into 25 µm bins at the lumen, middle, and base of the crypt, and the slices within these bins were

Z-stacked and measured for EdU intensity. * denotes statistical significance with 99% confidence.

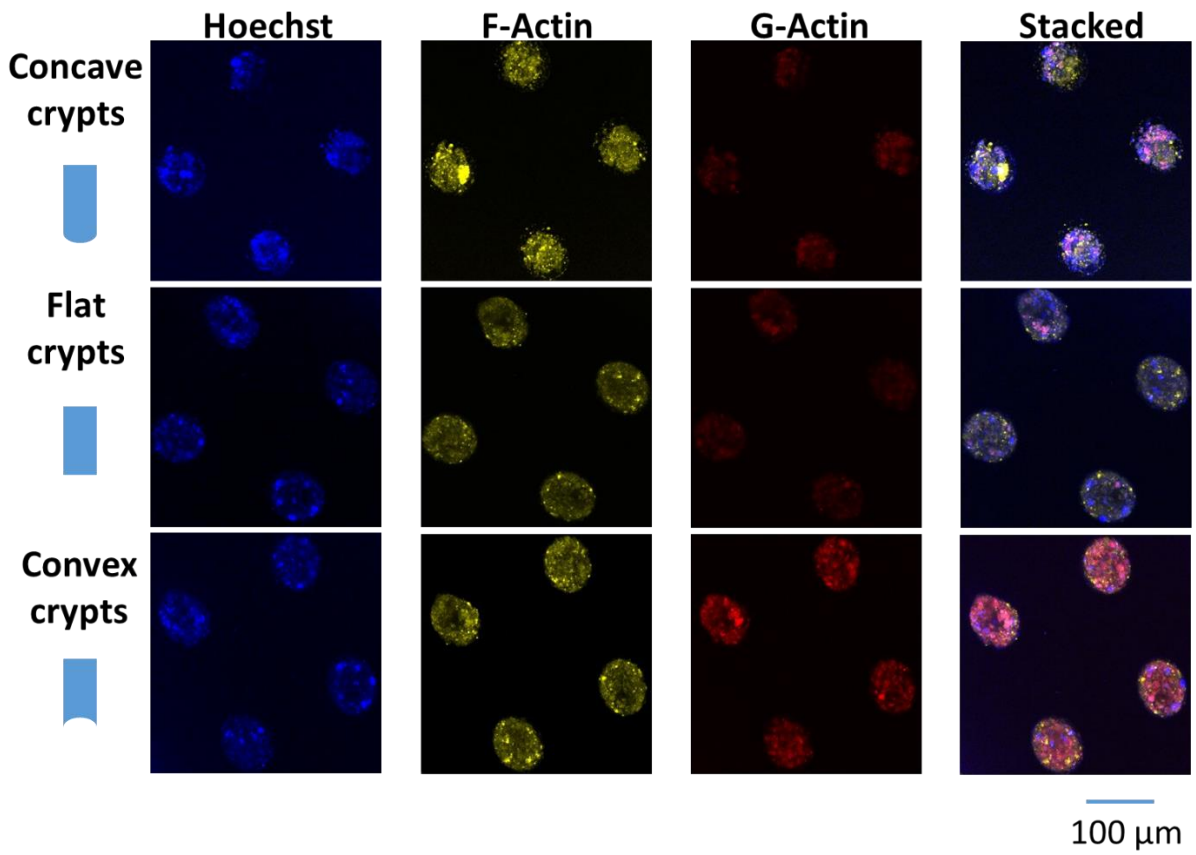

Figure 4.7. Measuring the effects of microcurvature in the *in vitro* crypt stem cell niche on cytoskeletal activity. Cytoskeletal image staining for each type of PDMS stamp. All crypts were imaged at the same laser intensity and voltage to allow for comparison. The bottom 25 µm of each crypt was included in these Z-stack images, incorporating the entirety of curvature at the bottom of each crypt. Hoechst is in blue, F-actin is in yellow, and G-actin is in red. The final stacked images include all three stains.

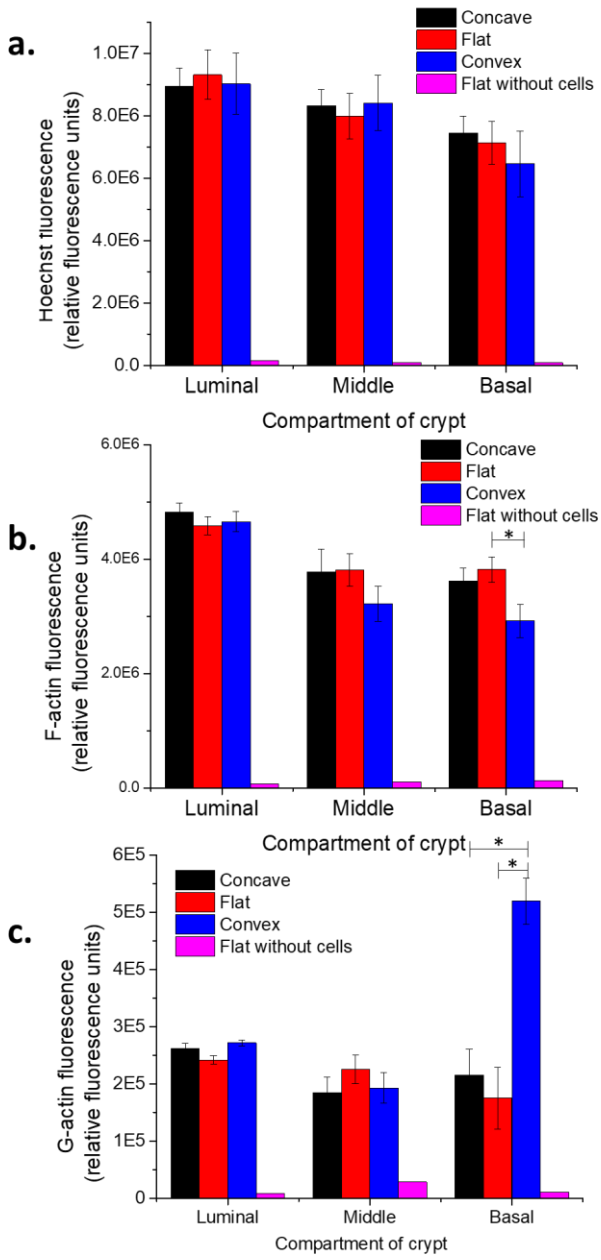

Figure 4.8. Quantifying cytoskeletal activity differences based on microcurvature in the *in vitro* crypt stem cell niche. a-c) After separation into 25 µm bins at the lumen, middle, and base sections of 25 crypts, the intensity of Hoechst (a), F-actin (b), and G-actin (c) was measured. These were all measured via confocal microscopy at the same laser intensity and voltage. *

denotes statistical significance with 99% confidence. All measurements for all crypt types were statistically significant from crypts with no cells seeded.

Section 4.6. Tables

Material	Surface energy (dynes/cm)	Number of hydroxyl groups	Used in study?	Reference
Dipropylene glycol (DPG)	33.9	2	+	[28]
Tetraethylene glycol (TEG)	44.0	2	+	[27]
Trimethylolethane (TMOE)	50.6	3	+	[37]
Glycerol	64.0	3	+	[29]
Threitol	77.2	4		[37]
Ribose	81.4	4	+	[37]
Xylitol	89.7	5	+	[37]
Glucose	92.0	5		[29]
Sorbitol	99.8	6	+	[29]
Sucrose	113.0	8		[29]
PDMS	20.8	N/A	+	[15]
Unmodified SU-8	45.2	N/A	+	[15]
Octyltrichlorosilane-treated SU-8	22.9	N/A	+	[15]

Table 4.1. Surface energy of materials in liquid lithography.

REFERENCES

1. Tran, K. T. M.; Nguyen, T. D. Lithography-Based Methods to Manufacture Biomaterials at Small Scales. *Journal of Science: Advanced Materials and Devices* **2017**, *2* (1), 1–14. https://doi.org/10.1016/j.jsamd.2016.12.001.

2. Zhang, H.; Yan, Q.; Xu, Q.; Xiao, C.; Liang, X. A Sacrificial Layer Strategy for Photolithography on Highly Hydrophobic Surface and Its Application for Electrowetting Devices. *Sci Rep* **2017**, *7* (1), 3983. https://doi.org/10.1038/s41598-017-04342-z.

3. Wu, E.-S.; Strickler, J. H.; Harrell, W. R.; Webb, W. W. Two-Photon Lithography for Microelectronic Application. In *Optical/Laser Microlithography V*; International Society for Optics and Photonics, 1992; Vol. 1674, pp 776–782. https://doi.org/10.1117/12.130367.

4. Seo, J.-H.; Park, J. H.; Kim, S.-I.; Park, B. J.; Ma, Z.; Choi, J.; Ju, B.-K. Nanopatterning by Laser Interference Lithography: Applications to Optical Devices. *J Nanosci Nanotechnol* **2014**, *14* (2), 1521–1532. https://doi.org/10.1166/jnn.2014.9199.

5. Loomis, J.; Ratnayake, D.; McKenna, C.; Walsh, K. M. Grayscale Lithography—Automated Mask Generation for Complex Three-Dimensional Topography. *JM3* **2016**, *15* (1), 013511. https://doi.org/10.1117/1.JMM.15.1.013511.

6. Faustino, V.; Catarino, S. O.; Lima, R.; Minas, G. Biomedical Microfluidic Devices by Using Low-Cost Fabrication Techniques: A Review. *Journal of Biomechanics* **2016**, *49* (11), 2280–2292. https://doi.org/10.1016/j.jbiomech.2015.11.031.

7. Kang, H.-W.; Lee, S. J.; Ko, I. K.; Kengla, C.; Yoo, J. J.; Atala, A. A 3D Bioprinting System to Produce Human-Scale Tissue Constructs with Structural Integrity. *Nature Biotechnology* **2016**, *34* (3), 312–319. https://doi.org/10.1038/nbt.3413.

8. Rose, J. C.; De Laporte, L. Hierarchical Design of Tissue Regenerative Constructs. *Advanced Healthcare Materials* **2019**, 1701067. https://doi.org/10.1002/adhm.201701067@10.1002/(ISSN)2192-2659.Regenerative-Medicine.

9. Lee, G.; Lee, J.; Oh, H.; Lee, S. Reproducible Construction of Surface Tension-Mediated Honeycomb Concave Microwell Arrays for Engineering of 3D Microtissues with Minimal Cell Loss. *PLoS ONE* **2016**, *11* (8), e0161026. https://doi.org/10.1371/journal.pone.0161026.

10. Suh, K.-Y.; Park, M. C.; Kim, P. Capillary Force Lithography: A Versatile Tool for Structured Biomaterials Interface Towards Cell and Tissue Engineering. *Advanced Functional Materials* **2009**, *19* (17), 2699–2712. https://doi.org/10.1002/adfm.200900771.

11. Zhang, Y.; Lo, C.-W.; Taylor, J. A.; Yang, S. Replica Molding of High-Aspect-Ratio Polymeric Nanopillar Arrays with High Fidelity. *Langmuir* **2006**, *22* (20), 8595–8601. https://doi.org/10.1021/la061372+.

12. Giang, U.-B. T.; King, M. R.; DeLouise, L. A. Microfabrication of Bubbular Cavities in PDMS for Cell Sorting and Microcell Culture Applications. *Journal of Bionic Engineering* **2008**, *5* (4), 308–316. https://doi.org/10.1016/S1672-6529(08)60175-4.

13. Liu, C.; Liu, J.; Gao, D.; Ding, M.; Lin, J.-M. Fabrication of Microwell Arrays Based on Two-Dimensional Ordered Polystyrene Microspheres for High-Throughput Single-Cell Analysis. *Anal. Chem.* **2010**, *82* (22), 9418–9424. https://doi.org/10.1021/ac102094r.

14. Kim, S.-H.; Lee, G. H.; Park, J. Y. Microwell Fabrication Methods and Applications for Cellular Studies. *Biomed. Eng. Lett.* **2013**, *3* (3), 131–137. https://doi.org/10.1007/s13534-013-0105-z.

15. Balowski, J. J.; Wang, Y.; Allbritton, N. L. Fabrication of 3D Microstructures from Interactions of Immiscible Liquids with a Structured Surface. *Advanced Materials* **2013**, *25* (30), 4107–4112. https://doi.org/10.1002/adma.201301658.

16. Humphries, A.; Wright, N. A. Colonic Crypt Organization and Tumorigenesis. *Nature Reviews Cancer* **2008**, *8* (6), 415–424. https://doi.org/10.1038/nrc2392.

17. Mercer, R. R.; Russell, M. L.; Crapo, J. D. Alveolar Septal Structure in Different Species. *Journal of Applied Physiology* **1994**, *77* (3), 1060–1066. https://doi.org/10.1152/jappl.1994.77.3.1060.

18. Sun, B.; Lam, R. H. W. Influence of Micro-Scale Substrate Curvature on Subcellular Behaviors of Vascular Cells. In *2016 IEEE 16th International Conference on Nanotechnology (IEEE-NANO)*; 2016; pp 339–342. https://doi.org/10.1109/NANO.2016.7751337.

19. Dupont, S.; Morsut, L.; Aragona, M.; Enzo, E.; Giulitti, S.; Cordenonsi, M.; Zanconato, F.; Le Digabel, J.; Forcato, M.; Bicciato, S.; et al. Role of YAP/TAZ in Mechanotransduction. *Nature* **2011**, *474* (7350), 179–183. https://doi.org/10.1038/nature10137.

20. Li, Q.; Kumar, A.; Makhija, E.; Shivashankar, G. V. The Regulation of Dynamic Mechanical Coupling between Actin Cytoskeleton and Nucleus by Matrix Geometry. *Biomaterials* **2014**, *35* (3), 961–969. https://doi.org/10.1016/j.biomaterials.2013.10.037.

21. Wang, Y.; Kim, R.; Gunasekara, D. B.; Reed, M. I.; DiSalvo, M.; Nguyen, D. L.; Bultman, S. J.; Sims, C. E.; Magness, S. T.; Allbritton, N. L. Formation of Human Colonic Crypt Array by Application of Chemical Gradients Across a Shaped Epithelial Monolayer. *Cellular and Molecular Gastroenterology and Hepatology* **2018**, *5* (2), 113–130. https://doi.org/10.1016/j.jcmgh.2017.10.007.

22. Beane, O. S.; Darling, E. M. Isolation, Characterization, and Differentiation of Stem Cells for Cartilage Regeneration. *Ann Biomed Eng* **2012**, *40* (10), 2079–2097. https://doi.org/10.1007/s10439-012-0639-8.

23. Wang, Y.; DiSalvo, M.; Gunasekara, D. B.; Dutton, J.; Proctor, A.; Lebhar, M. S.; Williamson, I. A.; Speer, J.; Howard, R. L.; Smiddy, N. M.; et al. Self-Renewing Monolayer of Primary Colonic or Rectal Epithelial Cells. *Cell Mol Gastroenterol Hepatol* **2017**, *4* (1), 165-182.e7. https://doi.org/10.1016/j.jcmgh.2017.02.011.

24. Pai, J.-H.; Wang, Y.; Salazar, G. T.; Sims, C. E.; Bachman, M.; Li, G. P.; Allbritton, N. L. A Photoresist with Low Fluorescence for Bioanalytical Applications. *Anal Chem* **2007**, *79* (22), 8774–8780. https://doi.org/10.1021/ac071528q.

25. Rasband, W.S., ImageJ, U. S. National Institutes of Health, Bethesda, Maryland, USA, https://imagej.nih.gov/ij/, 1997-2018.

26. Wang, H.; Dai, D.; Wu, X. Fabrication of Superhydrophobic Surfaces on Aluminum. *Applied Surface Science* **2008**, *254* (17), 5599–5601. https://doi.org/10.1016/j.apsusc.2008.03.004.

27. Dow Chemical, "Tetraethylene Glycol." 112-60-7 datasheet, Feb. 2007.

28. Monument Chemical, "Dipropylene Glycol (DPG)." 25265-71-8 datasheet, Jan. 2018.

29. Romero, C. M.; Paéz, M. S. Surface Tension of Aqueous Solutions of Alcohol and Polyols at 298.15 K. *Physics and Chemistry of Liquids* **2006**, *44* (1), 61–65. https://doi.org/10.1080/01421590500315360.

30. Parvathy Rao, A.; Venkateswara Rao, A. Modifying the Surface Energy and Hydrophobicity of the Low-Density Silica Aerogels through the Use of Combinations of Surface-Modification Agents. *J Mater Sci* **2010**, *45* (1), 51–63. https://doi.org/10.1007/s10853-009-3888-7.

31. Lacroix, L.-M.; Lejeune, M.; Ceriotti, L.; Kormunda, M.; Meziani, T.; Colpo, P.; Rossi, F. Tuneable Rough Surfaces: A New Approach for Elaboration of Superhydrophobic Films. *Surface Science* **2005**, *592* (1), 182–188. https://doi.org/10.1016/j.susc.2005.07.006.

32. Good, R. J. Contact Angle, Wetting, and Adhesion: A Critical Review. *Journal of Adhesion Science and Technology* **1992**, *6* (12), 1269–1302. https://doi.org/10.1163/156856192X00629.

33. Foley, B. M.; Hernández, S. C.; Duda, J. C.; Robinson, J. T.; Walton, S. G.; Hopkins, P. E. Modifying Surface Energy of Graphene via Plasma-Based Chemical Functionalization to Tune Thermal and Electrical Transport at Metal Interfaces. *Nano Lett.* **2015**, *15* (8), 4876–4882. https://doi.org/10.1021/acs.nanolett.5b00381.

34. Arkles, Barry. Hydrophobicity, Hydrophilicity and Silane Surface Modification. *Gelest, Inc.*, Morrisville, PA, USA. **2011.**

35. Ferreira, L. A.; Breydo, L.; Reichardt, C.; Uversky, V. N.; Zaslavsky, B. Y. Effects of Osmolytes on Solvent Features of Water in Aqueous Solutions. *Journal of Biomolecular*

36. *Structure and Dynamics* **2017**, *35* (5), 1055–1068. https://doi.org/10.1080/07391102.2016.1170633.

37. Théry, M. Micropatterning as a Tool to Decipher Cell Morphogenesis and Functions. *J Cell Sci* **2010**, *123* (24), 4201–4213. https://doi.org/10.1242/jcs.075150.

38. ACD/Structure Elucidator, version 2018.1, *Advanced Chemistry Development, Inc.*, Toronto, ON, Canada, www.acdlabs.com, 2019.

39. Kim, M.; Choi, J.-C.; Jung, H.-R.; Katz, J. S.; Kim, M.-G.; Doh, J. Addressable Micropatterning of Multiple Proteins and Cells by Microscope Projection Photolithography Based on a Protein Friendly Photoresist. *Langmuir* **2010**, *26* (14), 12112–12118. https://doi.org/10.1021/la1014253.

40. Tan, C. W.; Hirokawa, Y.; Gardiner, B. S.; Smith, D. W.; Burgess, A. W. Colon Cryptogenesis: Asymmetric Budding. *PLoS One* **2013**, *8* (10). https://doi.org/10.1371/journal.pone.0078519.

CHAPTER 5: CONCLUSIONS

The goal of this dissertation was to demonstrate the downstream effects of altered biomaterial properties on intestinal epithelial cell culture, allowing for potential applications of these cultures for lab-on-a-chip biotechnologies. This goal was accomplished in a two-fold manner, both with altered scaffold properties and their effects on *in vitro* cell behavior and with altered rheological properties for *in vitro* secretions (in this case, mucus).

It was demonstrated that using an air-liquid interface (ALI) with an intestinal cell monolayer allowed for the formation of a measurable attached mucus layer, a difficult proposition with typical submerged cell culture. When comparing the rheological properties of this mucus layer with native mucus, harvested from *ex vivo* surgical resections of colonic tissue, it was found that *in vitro* mucus was similar but slightly weaker. Biochemically and via immunohistochemistry, it was found that *ex vivo* mucus formed larger complexes with more overall mucins, nucleated around cells that were also detached from the native epithelial mucosa. Because of these findings, it was thought that *in vitro* culture produced a looser, more diffuse mucus layer in line with the native outer mucus layer, whereas native mucus provided elements of both the inner and outer mucus layer. Long-term, attempting to form a similar ALI culture with *in vitro* crypts instead of a monolayer could prove fruitful for closing the gap between *in vitro* and native intestinal mucus.

Moving towards cell culture scaffolding, it was shown that a) a controllable gradient of surface properties could be constructed using vapor-phase silanization, b) this gradient could be used in conjunction with liquid lithography to create biomedical micropillar stamps with

controlled microtip curvature, and c) these micropillar stamps could be used to form *in vitro* crypts with measurable effects on cell behavior. The gradient of silane deposition was accomplished using a primary diffusion chamber to hold vaporized silane, and a single-opening secondary diffusion chamber attached to the top of a surface to create a source-sink model of silane diffusion onto the surface. Longer diffusion times correlated to more silane deposition within the secondary diffusion chamber, allowing for quantifiable gradient formation. When silanization was coupled with liquid lithography, it was found that PDMS pillar stamps could be created with either convex- or concave-tipped pillars based on the sacrificial polyol used. It was also found that, by using the secondary diffusion chamber, a gradient of microtip curvatures could be achieved. When these pillars of different curvature were used as stamps for *in vitro* intestinal crypt culture, it was found that curvature of the stem cell niche played a role in downstream cell behavior. Specifically, it was found that convex-tipped pillars (creating concave crypts) generated a significantly higher amount of EdU in the stem cell niche, indicating strong proliferative activity than other crypt curvatures. It was also found that cytoskeletal activity was affected, with concave-tipped pillars (creating convex crypts) generating significantly higher amounts of G-actin compared to other crypt curvatures.

The experimental data gathered for this dissertation could increase the microstructural relevance of a lab-on-a-chip intestinal crypt model for use in tissue engineering, regenerative medicine, and drug screening. Overall, the effects of the physical microenvironment on *in vitro* cell behavior and secretion were demonstrated. These results, when coupled with the effects of altering the chemical microenvironment as well as co-culturing these models with other intestinal cell types, could significantly improve the effectiveness of this culture method in mimicking *in vivo* intestinal behavior.